

American University in Cairo

## AUC Knowledge Fountain

---

Theses and Dissertations

Student Research


---

Winter 1-31-2023

### In-Field Solar Panel Assessment and Fault Diagnosis

Muhammad Elgamal  
maelgamal@aucegypt.edu

Follow this and additional works at: <https://fount.aucegypt.edu/etds>

 Part of the [Electronic Devices and Semiconductor Manufacturing Commons](#), [Other Electrical and Computer Engineering Commons](#), and the [Power and Energy Commons](#)

---

#### Recommended Citation

##### APA Citation

Elgamal, M. (2023). *In-Field Solar Panel Assessment and Fault Diagnosis* [Master's Thesis, the American University in Cairo]. AUC Knowledge Fountain.

<https://fount.aucegypt.edu/etds/2038>

##### MLA Citation

Elgamal, Muhammad. *In-Field Solar Panel Assessment and Fault Diagnosis*. 2023. American University in Cairo, Master's Thesis. *AUC Knowledge Fountain*.

<https://fount.aucegypt.edu/etds/2038>

This Master's Thesis is brought to you for free and open access by the Student Research at AUC Knowledge Fountain. It has been accepted for inclusion in Theses and Dissertations by an authorized administrator of AUC Knowledge Fountain. For more information, please contact [thesisadmin@aucegypt.edu](mailto:thesisadmin@aucegypt.edu).



The American  
University in Cairo  
الجامعة الأمريكية بالقاهرة

Graduate Studies

*In-Field Solar Panel Assessment and Fault Diagnosis*

A THESIS SUBMITTED BY

Muhammad Elgamal

TO THE

*Department of Electronics and Communications  
Engineering*

Dec. 27, 2022

*in partial fulfillment of the requirements for the degree of  
Master of Science, MSc in Electronics and Communications  
Engineering*

# Declaration of Authorship

I, Muhammad Elgamal declare that this thesis titled, "In-Field Solar Panel Assessment and Fault Diagnosis Using Machine Learning" and the work presented in it are my own. I confirm that:

- This work was done wholly or mainly while in candidature for a research degree at this University.
- Where any part of this thesis has previously been submitted for a degree or any other qualification at this University or any other institution, this has been clearly stated.
- Where I have consulted the published work of others, this is always clearly attributed.
- Where I have quoted from the work of others, the source is always given. With the exception of such quotations, this thesis is entirely my own work.
- I have acknowledged all main sources of help.
- Where the thesis is based on work done by myself jointly with others, I have made clear exactly what was done by others and what I have contributed myself.

Signed:



---

Date:

Dec. 29, 2022

---

# Abstract

Photovoltaic energy is a green energy that suit from small houses to high-power stations spanning large areas. In such large areas, monitoring individual panels can be a tedious task, especially if it was required to identify operational faults of these panels. Photovoltaic 4.0 technology depend on collecting data from each station and feeding them to a central processing system that is capable of analyzing operation data and hopefully locate when a fault happens. Additionally, analysis of collected data may take several approaches of which we are interested in a model-based-difference approach. So, we have a theoretical model of the station at a hand and at the other hand we have actual measurement and based on the discrepancy between the model and the measurement we judge the occurrence of a fault. In such method, it is crucial to the model to be accurate as much as possible and for measuring device to be accurate as well to have a clear judgement. In this work, we build an analysis module at the center of a photovoltaic 4.0 station implemented in the American University in Cairo. The model is comprehensive in nature and is capable of modelling from individual cell level to the whole panel level as well as dealing with measurement issues to have a good judgement at the end. The used model is based on single-diode model of a solar panel and is capable of modelling solar panels in different environmental conditions and is validated against datasheet and actual measurement.

# Acknowledgements

Special Thanks to Ammar Elsedawy, Omar Morsy and Dalia Ahmed at Center of Nanoelectronics and Devices, CND, for providing required data from installed photovoltaic energy site within the American University in Cairo. Also, special Thanks to Ahmed Handossa from Energy Power Systems for information about installed site and commercial information about the subject.

This thesis included research done on a plant that is installed by a grant from IT Industry Development Agency, ITIDA for project CFP160 titled: " Photovoltaic4.0 Research and Development of O&M Technologies for PV plants management". The project started at Jan. 2020 and finished at Sep. 2022 it was implemented by Energy Power Systems company with Center of Nanoelectronics and Devices, CND at AUC as an academic research partner.

# Contents

<b>Declaration of Authorship</b> .....	<b>1</b>
<b>Abstract</b> .....	<b>2</b>
<b>Acknowledgements</b> .....	<b>3</b>
<b>List of Figures</b> .....	<b>8</b>
<b>List of Tables</b> .....	<b>10</b>
<b>List of Equations</b> .....	<b>11</b>
<b>List of Abbreviations</b> .....	<b>13</b>
<b>List of Symbols</b> .....	<b>14</b>
<b>Introduction</b> .....	<b>15</b>
1.1 Economy of Photovoltaic Energy .....	16
1.2 Maintenance Issues.....	18
1.2.1 Monitoring systems available in the market and under development .....	19
1.2.1.1 Schneider Electric’s Exostruxure platform .....	19
1.2.1.2 ABB Ability platform.....	20
1.2.1.3 TRUST PV.....	20
1.3 Research Aim and Scope.....	22
<b>Solar Cell Basics</b> .....	<b>23</b>
2.1 Contemporary Solar Cell Technologies.....	23
2.1.1 First-generation solar cells.....	23
2.1.1.1 Monocrystalline silicon solar cell.....	23
2.2.1.2 Multi-crystalline silicon solar cells.....	25
2.1.2 Second-generation solar cells .....	26
2.2.2.1 Thin-film solar cells.....	26
2.1.3 Third- generation solar cells.....	27
2.1.4 Comparison of solar cell technologies at the state of the art .....	27
2.1.4.1 First Generation.....	27
2.1.4.2 Second generation .....	27
2.1.4.3 Third generation.....	28
2.2 Solar Cell Physics .....	29

2.2.1	P-N Junction Revisited .....	30
2.2.2	Solar cell as a p-n junction .....	32
2.2.3	Derivation of Single-Diode Model.....	35
2.2.4	Industrial Parameters .....	36
2.2.5	Normal Industrial Parameters .....	37
2.3	Summary .....	41
<b>Fault Classification and Diagnosis.....</b>		<b>42</b>
3.1	Comparative evaluation of fault detection approaches.....	42
3.2	Hotspot and shading faults .....	46
3.2.1	Ma's method for hotspot detection based on IV curves.....	46
3.2.2	Niazi's method for hotspot detection by infrared imaging .....	50
3.3	Modelling solar panel with arbitrary irradiance distribution and partial shading.....	52
3.4	Summary .....	54
<b>Modelling Panel in Field.....</b>		<b>56</b>
4.1	Modelling Environmental Conditions .....	56
4.1.1	Estimating cell temperature.....	56
4.1.2	Estimating total irradiance incident on a solar panel .....	57
4.1.2.1	Positioning the panel and the sun.....	58
4.1.2.2	Irradiance Models.....	60
4.2	SDM Explained.....	62
4.2.1	Why SDM and its limitations? .....	62
4.2.2	Modelling from cell up to array .....	64
4.2.2.1	Cell string with different irradiance levels .....	65
4.2.2.1	Finding the IV characteristics of a panel .....	66
4.3	SDM parameter extraction.....	69
4.3.1	Family 1 approaches.....	69
4.3.1.1	Saloux's method .....	71
4.3.1.2	Cannizzaro's method.....	71
4.3.2	Family 2 approaches.....	73
4.3.2.1	Stornelli's method .....	73
4.3.2.2	Laudani's method with our modifications .....	74
4.3.3	Comparison between different Family 2 approaches .....	77
4.4	Translating circuit parameters at different environmental conditions .....	79
4.4.1	Valerio's model.....	80
4.4.2	Short-circuit current model .....	81
4.4.3	Open-circuit voltage model.....	81
4.4.4	Series and parallel resistance model .....	81
4.4.5	Ideality model.....	82
4.4.6	Photocurrent and diode reverse saturation current model.....	82
4.4.7	Efficiency model.....	82

4.4.8	Verifying parameter translation from datasheet measurements .....	82
4.5	Summary .....	84
<b>Installed Site and Analysis Module .....</b>		<b>86</b>
5.1	Site Description .....	86
5.1.1	Location .....	86
5.1.2	System architecture.....	87
5.1.3	Panel specifications.....	89
5.1.4	Characterizers.....	90
5.1.5	Power conversion.....	91
5.1.6	Weather station .....	92
5.1.7	Communication with station.....	93
5.2	Analysis Module .....	94
5.3	Summary .....	95
<b>Analysis Procedures and Results.....</b>		<b>96</b>
6.1	Description of Dataset .....	96
6.2	Limitations of characterizers .....	98
6.2.1	Characterizer measurements irregularities .....	98
6.2.1.1	Small number of points .....	98
6.2.1.2	Current saturation near short-circuit or open-circuit regions.....	99
6.2.1.3	Missing points at low voltage.....	100
6.2.1.4	Noisiness and varying sampling rate .....	100
6.2.2	Measures for characterizers quality .....	101
6.3	Parameter extraction.....	107
6.3.1	Parameter Extraction on given dataset .....	107
6.4	Parameter translation & weather models .....	109
-6.4.1	Verifying weather models from datasets .....	109
6.4.2	Distribution of Environmental conditions .....	111
6.5	Doing data analysis.....	112
6.5.1	Analysis in time.....	112
6.5.2	Analysis in space.....	115
6.5.3	Comparing standard IV curves.....	115
6.6	Summary .....	117
<b>Conclusions.....</b>		<b>118</b>
<b>References .....</b>		<b>119</b>
<b>Appendix.....</b>		<b>126</b>
Full Description of Analysis Module .....		126
1	Dependencies, APIs, and code templates.....	126
1.1	Mathematical and scientific computing packages.....	126



1.2	Weather APIs .....	126
1.3	Additional packages .....	128
2	Functions .....	128
2.1	Reading a single characterization .....	128
2.2	Reading and saving variables .....	129
2.3	Parsing and analyzing reports .....	129
2.4	Running Optimization .....	130
3	Used classes .....	131
3.1	<code>iv_measurement</code> class .....	131
3.2	<code>cell</code> class .....	135
3.3	<code>cell_string</code> class .....	135
3.4	<code>panel</code> class .....	135

## List of Figures

Figure 1 Yearly direct normal irradiance in $kWh/m^2$ .....	15
Figure 2 Annual peak load of Egypt in MW .....	16
Figure 4, energy production share of each technology.....	17
Figure 3 Attractiveness of each technology compared to order in energy share.....	17
Figure 5 Different capabilities of Electric Schneider ExoStruxure .....	21
Figure 6 Monocrystalline panel with cells separated.....	24
Figure 7 Structure of different monocrystalline silicon cells (a) <b>PERL</b> cell, (b) <b>HIT</b> , (c) <b>BC-BJ</b> , (d) <b>IBC</b> and (e) buried contact structure.....	25
Figure 8 Mosaic shaped multi-crystalline solar cells .....	25
Figure 9 (a) Metal-Wrap-Through cell, <b>MWT</b> , (b) Emitter Wrap-Through, <b>EWT</b> , Solar Cell.....	26
Figure 10 Cost efficiency of different solar cell generations .....	28
Figure 11 Development of solar cell efficiencies evolution through time for different technologies.....	29
Figure 12 (a) p-n junction at equilibrium and (b) doping profile of step p-n junction.....	30
Figure 13 Energy-band diagram for a p-n junction.....	31
Figure 14 Three different radiative processes in semiconductors, here $f$ denotes the probability density function of particle at energy level either it is a photon or an electron.....	33
Figure 15 Energy band diagram of simple p-n junction solar cell with different loss mechanisms numbered from 1 to 7 .....	34
Figure 16 Single Diode Model of Solar Cell.....	35
Figure 17 IV characteristics of a solar cell when illuminated (solid black), dark (dashed black) as well as the power generated (green). .....	36
Figure 18 Quantum efficiency of Monocrystalline silicon solar cell based on normalized current at different wavelengths.....	38
Figure 19 Shockley-Queisser Limit for efficiency assuming blackbody radiation with aforementioned criteria and with AM1.5 spectrum at several fractions of radiative recombination namely, 1, 10 – 3 and 10 – 6.....	39
Figure 20 Shockley-Queisser limit for short-circuit current density and for the open-circuit voltage ratio $eVOC/Eg$ .....	39
Figure 21 Efficiency of different solar technologies for minicells, standard cell size and for a whole panel (module).....	41
Figure 22 All possible faults encountered in a photovoltaic array .....	43
Figure 23 time domain reflectometry using function generator and an oscilloscope to check a panel string.....	44
Figure 24 A brief description of RDM, OSA, MBDM and MLT .....	45
Figure 25 IV characteristics of (a) leaky panel with a hotspot cell or (b) nonleaky panel with a hotspot cell .....	47
Figure 26 Distance features extracted from a stepped IV characteristics.....	48
Figure 27 Looking for faults in other domain other than the IV characteristics .....	49
Figure 28 Installed station for the collection of thermal imaging.....	50
Figure 29 Summary of algorithm used to train on infrared images of solar panels and how to	

extract faulty panels like those showing hotspot or cracks here .....	52
Figure 30 Code snippet for simulating a panel with specific SDM parameter set.....	53
Figure 31 Resulting IV characteristics for shaded panel.....	53
Figure 32 Histogram of a noisy shaded panel reading.....	54
Figure 33 Procedure to estimate approximate irradiance levels from IV characteristics.....	54
Figure 34 Solar spectra after modelling sun as a black body or after measuring actual spectra in space and on earth.....	58
Figure 35 Location of the sun described by altitude, zenith and azimuth angles, and panel is described by tilt and azimuth angles .....	59
Figure 36 Different types of irradiance incident on a solar panel .....	59
Figure 37 DDM and TDM for a solar cell.....	63
Figure 38 Internal connection of a photovoltaic panel as a series connection of cell strings and cells are positioned in physical panel.....	64
Figure 39 Code snippet for defining a cell string .....	65
Figure 40 IV characteristics for a cell string of three irradiance distributions.....	66
Figure 41 Active current path when (a) all panels are shaded, (b) when only one panel produces current and the two other panels are bypassed, (c) when only one panel is bypassed for being shaded and (d) when all panels are active.....	67
Figure 42 The IV characteristics of three different panels in Figure 33, and their resultant IV when connected together .....	68
Figure 43 Fitting of both algorithms at low and high irradiance .....	78
Figure 44 Error for both algorithms at different irradiance levels .....	79
Figure 45 Curves translated from STC curve compared to the datasheet value (in dots).....	83
Figure 46 Error in translated IV curves when parameters are extracted initially by Laudani's algorithm .....	84
Figure 47 Actual installed station V.S. satellite view from Google Maps.....	86
Figure 48 Panel numbering.....	87
Figure 49 On-grid topology of the station .....	88
Figure 50 System Architecture .....	88
Figure 51 Actual panel used with a schematic showing its dimensions .....	89
Figure 52 IV characteristics of used panel at different irradiance levels.....	90
Figure 53 Characterizers used in this research developed by CND .....	90
Figure 54 ABB inverter of model TRIO-27.6-TL-OUTD .....	91
Figure 55 Installed weather station.....	92
Figure 56 Data-logger for the weather station- main ports.....	93
Figure 57 Communication box used at the station.....	93
Figure 58 Architecture of analysis module.....	94
Figure 59 Daily number of readings in dataset 1.....	96
Figure 60 Daily number of readings in dataset 2.....	97
Figure 61 Readings by each of the active characterizers .....	98
Figure 62 Small number of points before sunset .....	99
Figure 63 Presence of current saturation in some reading.....	99
Figure 64 Problems in readings from dataset 1. Panel 1 has slight increase of current at short-circuit region and panel 2 has sudden decrease in short-circuit current before the maximum power point.....	100
Figure 65 Noisy measurement from dataset 2 .....	100
Figure 66 Original reading being conditioned.....	101
Figure 67 Probability of having a $V_{min}$ with a specific value of both datasets.....	102
Figure 68 Probability of having a specific $V_{step}$ for both datasets .....	102

Figure 69 Probability of having a specific point count .....	103
Figure 70 Probability of having a specific fill factor in both datasets .....	103
Figure 71 Change of minimum voltage against hour of the day (dataset 2) .....	105
Figure 72 Change of minimum voltage per hour of the day (dataset 1) .....	106
Figure 73 Average number of points per reading against hour in dataset 2 .....	106
Figure 74 Histogram of NRMSE based on Laudani's parameter extraction for both datasets ...	108
Figure 75 Probability of NRMSE lesser than a specific value .....	108
Figure 76 Probability of having ratio of parameter to its expected value lower than a given $x$ , for both datasets .....	110
Figure 77 Probability distribution of cell temperature and irradiance in both datasets .....	111
Figure 78 Time analysis of panel 8.....	113
Figure 79 Time analysis for panel 35.....	114
Figure 80 Comparison of standard curve generated by our model and an actual measurement (reading1 above and reading 2 below).....	116
Figure 81 Flowchart for irradiance estimation.....	128
Figure 82 Sample station report. Yellow is panel ID, red is timestamp and green is sequence of IV points. ....	129
Figure 83 Finding panel irradiance from cell irradiance .....	136

## List of Tables

Table 2 Egyptian companies for PV panels .....	18
Table 1 Savings for each renewable energy technology, RET.....	18
Table 3 Example solar cell circuit parameters.....	35
Table 4 Industrial parameters of cell with circuit parameters in Table 3.....	37
Table 5 Industrial Parameters for solar cells of different technologies ideally (based on Shockley-Queisser limit) or from best-manufactured cells. Here we assume $c = 1$ and $J_{SC} = ISC/A$ . EQE is external quantum efficiency as shown in Figure 14 .....	40
Table 6 maximal industrial parameters for a solar panel that has $c$ cells and $A$ total area.....	40
Table 7 Merits and demerits of the different approaches of fault detection.....	44
Table 8 The characteristics of $dN_{max}$ values for different voltage regions.....	49
Table 9 System performance in terms of sensitivity, specificity and precision.....	51
Table 10 Thermal correction factors and temperature change of a solar panel in different fixtures .....	57
Table 11 Albedo values for different location types.....	61
Table 12 Coefficients for Perez-Ineichen model.....	62
Table 13 Comparison between SDM and DDM in different aspects .....	63
Table 14 Comparison between strings of different photocurrents.....	66
Table 15 Performance of seventeen different methods for parameter extraction on the NREL dataset.....	71
Table 16 Extracted parameters using both methods .....	79
Table 17 Irradiance incident on station per year, best panel tilt angle and maximum power production per year .....	87
Table 18 Specifications of panel type Suntech STP275-20/Wfw .....	89
Table 19 Specifications of TRIO-27.6-TL-OUTD by ABB.....	92
Table 20 Number of active characterizers throughout time.....	97
Table 21 Quality metrics for all characterizers in dataset 1.....	104

Table 22 Quality metrics for all characterizers in dataset 2.....	104
Table 23 Percentage of dataset curves where measured parameters are less than or equal to the expectation .....	111
Table 24 Decoherence measure between panel 8 and panel 35 .....	115
Table 25 Two readings used for standard curve comparison.....	115

## List of Equations

(1).....	30
(2).....	31
(3).....	31
(4).....	31
(5).....	32
(6).....	32
(7).....	32
(8).....	32
(9).....	34
(10).....	35
(11).....	35
(12).....	37
(13).....	56
(14).....	56
(15).....	57
(16).....	58
(17).....	59
(18).....	59
(19).....	59
(20).....	60
(21).....	60
(22).....	60
(23).....	60
(24).....	61
(25).....	61
(26).....	61
(27).....	61
(28).....	61
(29).....	62
(30).....	62
(31).....	65
(32).....	67
(33).....	67
(34).....	68
(35).....	68
(36).....	68
(37).....	69
(38).....	69
(39).....	69
(40).....	70

(41)	70
(42)	70
(43)	70
(44)	70
(45)	71
(46)	71
(47)	71
(48)	72
(49)	72
(50)	72
(51)	72
(52)	72
(53)	72
(54)	72
(55)	72
(56)	73
(57)	73
(58)	73
(59)	73
(60)	74
(61)	74
(62)	75
(63)	75
(64)	75
(65)	75
(66)	75
(67)	76
(68)	76
(69)	76
(70)	76
(71)	76
(72)	76
(73)	80
(74)	80
(75)	80
(76)	81
(77)	81
(78)	81
(79)	81
(80)	81
(81)	81
(82)	82
(83)	82
(84)	82
(85)	82
(86)	135

# List of Abbreviations

<b>PERL</b>	passivated emitter rear localized
<b>HIT</b>	heterojunction with intrinsic thin layer
<b>TCO</b>	transparent conductive oxide
<b>BC-BJ</b>	back contact -back junction
<b>ARC</b>	anti-reflective coating
<b>IBC</b>	interdigitated back contact
<b>LID</b>	light-induced-degradation
<b>MWT</b>	metal-wrap-through
<b>EWT</b>	emitter-wrap-through
<b>IV characteristics</b>	current-voltage characteristics
<b>SDM</b>	Single-Diode Model
<b>MPPT</b>	Maximum Power Point Tracker
<b>DDM</b>	Double-Diode Model
<b>TDM</b>	Triple-Diode Model
<b>LAN</b>	Local Area Network
<b>GUI</b>	Graphical User Interface
<b>SPICE</b>	Simulation Program with Intended Circuit Emphasis (a programming language used for the description and simulation of electronic circuits)
<b>API</b>	Application Programming Interface
<b>MBDM</b>	Model-Based Difference Method
<b>SPAM</b>	Sandia Photovoltaic Array Modelling
<b>CSP</b>	Concentrated Solar Power
<b>PV</b>	Photovoltaic
<b>SWH</b>	Solar Water Heater

# List of Symbols

$e$	Elementary electron charge $1.60217663 \times 10^{-19} C$
$\epsilon_s$	Dielectric permittivity of silicon
$N_d, N_a$	Donor and acceptor concentration
$x_n, x_p$	Extent of space charge region in the n or p region
$E_c, E_v$	Edge of the conduction or valence band
$E_{Fi}$	Intrinsic Fermi level
$E_F$	Fermi level
$\Phi_{Fp}, \Phi_{Fn}$	Absolute potential difference between intrinsic Fermi level and Fermi level in p or n region
$V_{bi}$	Built-in voltage in a p-n junction
$V_a$	Applied Voltage
$E_{Fn}, E_{Fp}$	Fermi level in p or n region
$\mu_p, \mu_n$	Mobility of holes and electrons
$\delta p_n, \delta n_p$	Excess minority holes and electrons
$J, J_s$	Current density, reverse saturation current density
$D_n, D_p$	Diffusion coefficient for electrons and holes
$L_n, L_p$	Diffusion length for electrons and holes
$k$	Boltzmann constant $1.380649 \times 10^{-23} m^2kg s^{-2}K^{-2}$
$T$	Absolute temperature in Kelvin
$n$	p-n junction ideality factor
$N_c, N_v$	Intrinsic density of states in conduction and valence bands
$E_g$	Energy gap
$I_{ph}$	Photocurrent
$R_s, R_p$	Series and parallel resistances in the SDM
$I_D$	Diode current
$I_{SC}, V_{OC}$	Short-circuit current, open-circuit voltage
$P_{MP}, V_{MP}, I_{MP}$	Maximum power, voltage and current at maximum power



# Chapter 1

## Introduction

Photovoltaic energy has been used extensively as a power source standalone for houses or for general distribution networks [1]. The actual need for solar energy stems from the rapid growth of population and the continuous depletion of fossil fuels[2].

Egypt specifically has great potential for solar energy as it belongs to the solar belt and in 1991 solar atlas of Egypt, it was shown that Egypt enjoys 3900-3200 hours of yearly sunshine with direct normal energy of  $3200 \text{ kWh/m}^2$  [3]. The maximum attainable solar energy in Egypt is 73.6 Petawatt hour (PWh) [3]. The distribution of solar energy is uneven and Egypt is one of the luckiest countries (see Figure 1 adopted from [3])

Around 90% of the electrical energy produced in Egypt are from fossil fuels, mainly from power stations relying on gas. The demand for energy is limited by the current power capacity and it can have power shortage if the country gas resources are depleted which affects country's economy and social welfare[4]. The annual growth of the peak electrical load of the country is 6% (see Figure 2 as adopted from [4], [5]). Until now, maximum installed power exceeds maximum load slightly of which 52% are gas stations. It is expected that over the next twenty years the energy demand will increase by 15-25% yearly. In 2017, the total installed energy capacity of solar energy is 145.2MW, and it was planned to reach 2.13 GW in 2020[6]

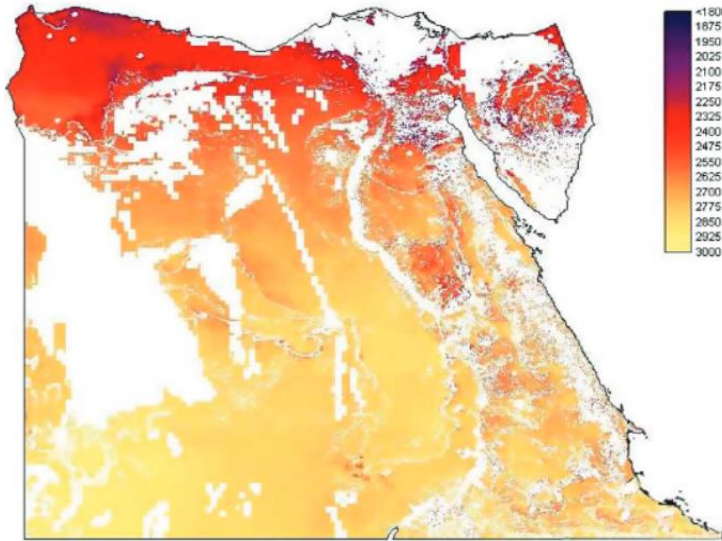


Figure 1 Yearly direct normal irradiance in  $\text{kWh/m}^2$

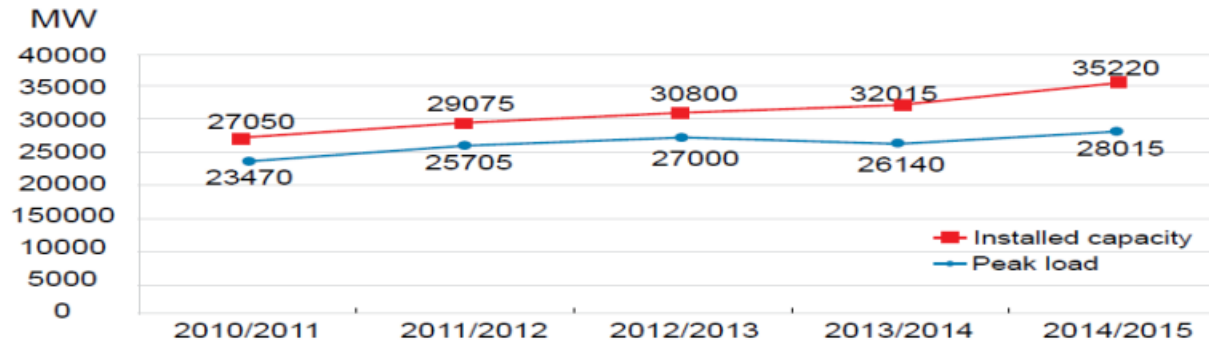


Figure 2 Annual peak load of Egypt in MW

## 1.1 Economy of Photovoltaic Energy

The Egyptian government is planning to privatize electricity industry with possibilities of foreign investments which opens the door for several companies to compete in providing renewable energy solutions especially solar panels [4].

Several solar energy technologies exist like: Concentrated-Solar-Power (CSP), Solar Water Heater, (SWH) and Photovoltaic (PV). Each one of these technologies has a market share within the Egyptian Energy Production Economy. CSPs depend on a mirror/lens system that concentrates sun rays and produces heat into a steam that used afterward for a conventional energy production plant. SWH uses sun rays directly for the purpose of water heating without concentrators for both energy production and water desalination and finally PV which depend on generating current through photovoltaic effect.

In [7], the energy production share for all technologies is shown in Figure 4, where PV technology has the lowest energy share in all years. Also, there are three different scenarios for future energy production (beginning from 2010 to 2022 by the Energy Research Center at Cairo University) that would benefit the Egyptian economy saving costs and environment, named high, medium, and low scenarios. In Table 1, PV energy at best scenario (high) can save 1 million ton of oil-equivalent and 3 million tons of  $CO_2$ . Additionally, it can save fossil fuel that can be exported of 258 million dollars (based on the used rate of gas per watt production). Furthermore, it can save energy subsidy with 62 million dollars. Even in the best economic scenario, the PV technology has the lowest share of savings. However, it opens the door for small companies to flourish although its share in power production comes after the wind technology, CSP, and hydropower as renewable sources of energy. Additionally, PV technology comes after CSP in research and development expenses and before SWH, which means reasonable opportunity and higher attractiveness for research and development as shown in Figure 3 (adopted from [7])

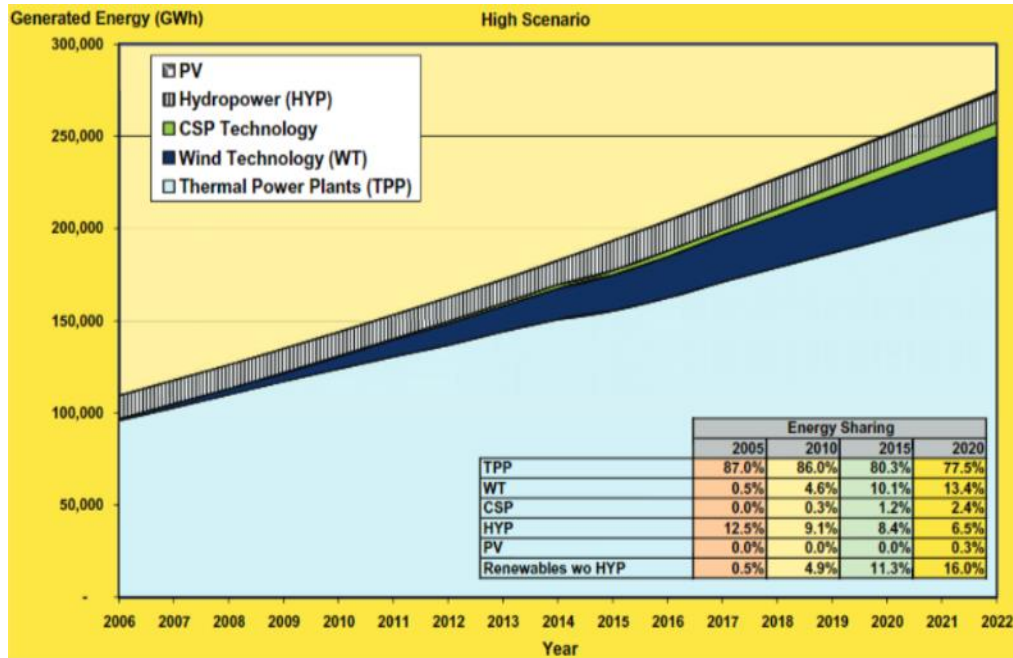


Figure 4, energy production share of each technology

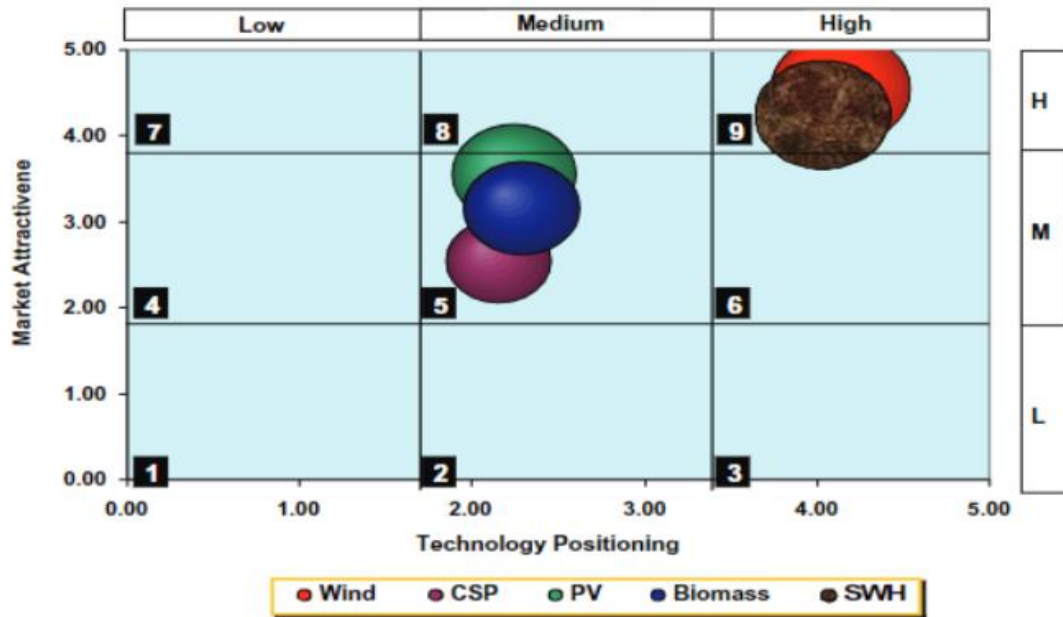


Figure 3 Attractiveness of each technology compared to order in energy share

Several companies are involved in solar energy production in Egypt [8]. Most solar cells are imported from Europe, the USA, Japan and China. However, some companies like the Arab Organization for Industrialization has two manufacturing lines to produce **PV** modules with capacity of 1MWP per year beside the only private company doing this called BIC for electronics, environment and energy. These companies has 25% of the manufactured materials and the cells

themselves are imported; the only local parts are junction boxes, frames, glass and electrical connections. A list of biggest companies in the Egyptian market by 2011 are listed in Table 2 (adopted from [8]). Some other companies and startups include: KaramSolar, InfinitySolar and Empower Energy Systems, EES.

Table 1 Savings for each renewable energy technology, RET

Technology of power generation	Anticipated savings		Anticipated cost savings (million US\$)		Anticipated avoided subsidy (million US\$)		Generated energy via RET (million kWh)
	TOE (million)	CO <sub>2</sub> (million tons)	Opportunity cost for export	Certified emission reduction	Business as usual	Fuel prices liberation to close the gap	
<i>High scenario</i>							
Wind	67	179	17,299	1789	13,311	5292	293,608
CSP	10	27	2656	275	2043	751	45,070
PV	1	3	258	27	199	62	4380
Total	78	209	20,213	2090	15,553	6105	343,059
<i>Medium scenario</i>							
Wind	46	122	11,830	1223	9103	3648	200,776
CSP	7	17	1680	174	1293	485	28,514
PV	0.6	1.5	142	15	109	34	2,409
Total	53	141	13,652	1412	10,505	4167	231,699
<i>Low scenario</i>							
Wind	22	59	5728	592	4408	1840	97,222
CSP	4	10	975	101	751	283	16,556
PV	–	–	–	–	–	–	–
Total	26	69	6704	693	5158	2123	113,778

Table 2 Egyptian companies for PV panels

PV systems supply	
Company name	Type of work
Arabian Solar Energy & Technology Co. (ASET)	Sales of PV systems and installation energy saving lamps
MEET	Sales of PV systems and installation
BIC for Electronics Environment & Energy	PV modules assembly and sales of PV systems
Arab African Company	Sales of PV systems
IMF Company	Sales of PV systems
EGAT	Sales of PV systems
Elctrometry	Sales of PV systems
Egyptian Company for Development of Engineering Works (EEWD)	Sales of PV systems
Gamma Group Company	Sales of PV systems

## 1.2 Maintenance Issues

Large stations like Benban solar park [9] with total power production capacity of 1.8 GW have thousands of solar panels that coproduce electric energy that would be delivered to end users. The problem with installed stations is that when a panel drops, the power production of panel string is reduced significantly. The cost of fault detection and shut down of the entire station plus the maintenance cost is extremely high. Several companies provide monitoring

systems for installed stations that suit electrical energy operators.

## **1.2.1 Monitoring systems available in the market and under development**

### **1.2.1.1 Schneider Electric's Exostruxure platform**

The Exostruxure platform[10] is Schneider electric's digital backbone connecting operational technology (OT) solutions with the latest in IT technology to unlock value in operations and leverage the true potential of the Internet of Things.

Schneider electric's Exostruxure includes several software that suit almost any application, most interesting to the context in hand is the Power Monitoring Expert (PME), which is employed in the context of exclusive monitoring and the Power Supervisory Control and Data Acquisition (Power SCADA) used in monitoring and control of devices simultaneously, they also offer a building management software (BMS) named Exostruxure building Operation (EBO). With respect to monitoring, Schneider electric offer the Power Monitoring Expert (PME) software, which allows the user to monitor his entire power system with quite illustrative visualizations. The PME consists of three layers, (1) the physical layer, (2) edge control software, and (3) the applications and analytics layer also known as the advisory layer. The physical layer is the layer of sensors and physical devices that measure the process data and send information over a communication network.

The edge control software consists of several visualization and analytics features such as dashboard, homepage, reports, alarms, trends, diagrams and data comparison features, and it has a refresh rate of five seconds. In addition, it has several levels of access for users and it employs a local database for data storage. Storage of data is designed to be on a SQL local server, and communication with the software can take place over TCP/IP, Modbus TCP or Modbus RTU protocols, also data collection can take place from the plant gateway or directly from the device. However, it requires a license. The software consists of license standard modules and Add-on modules.

On the contrary advisory layer, which uses collected data to make predictions is an Azure based cloud platform that analyzes the data collected and produces advisory report, for example it can recommend a new equipment to the operator to solve a certain problem and as it recommends it displays the new equipment data and price and it can predict information about the plant under investigation. The advisory layer requires annual subscription fees and storage of information takes place on the Azure cloud platform.

Here we demonstrate two advisory add-on examples, first is the asset advisor add-on, which is used to evaluate live data from connected assets and used to apply analytics to identify potential threats. Second is the electrical health advisor, which is used to predict a problem and suggest a solution, which saves a lot of engineering time.

Figure 5 shows the different capabilities that Schneider ExoStruxure can do:

- (a) It has a dashboard including all metrics of installed station, like total power production, weather conditions, power quality metrics.
- (b) Mapping of solar station performance to the physical placement of the panels.
- (c) Analysis of the power delivered to several types of loads connected to the station.
- (d) Network electrical architecture including inverters, panels and sensors.

### 1.2.1.2 ABB Ability platform

ABB Ability [11] is ABB's IoT platform for digitalization of the industry, it offers its users the ability to predict faults, the ability to monitor all plant variables, the ability to optimize plant performance, the ability to optimize maintenance time and increase uptime, it also offers powerful analysis and prediction tools to assess the health of the devices within the plant.

### 1.2.1.3 TRUST PV

TRUST PV [12] is a four-year project with total cost of €13 million, including €9 million funded from the European Union. The project aims at increasing the friendly integration of reliable PV plants considering different market segments through the demonstration of increased performance and reliability of PV components and PV systems in large portfolios of distributed and utility scale PV.

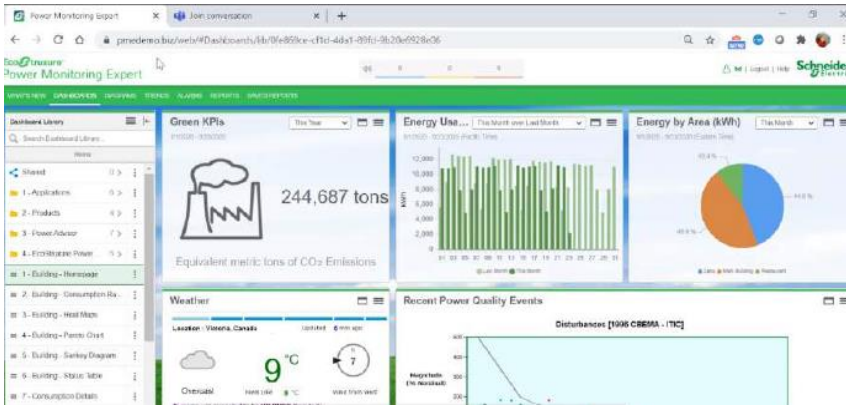
The project aims its activities at the improvement of PV module operations and maintenance friendly design, inverter enabled operation and maintenance solutions, extended testing, accurate energy yield modelling and data driven mitigation measures. The data gathered will flow into Artificial Intelligence (AI) enhanced decision support systems.

TRUST PV is driven by the needs of the PV project stakeholders, such as the end users, system integrators and operation and maintenance operators. Yield assessment models will be developed to become more accurate by full utilization of the digitalization of the PV sector through the integration of 3D design and Building Information Modelling (BIM) to eliminate the gap between performance and failure detection through monitoring and field inspection. The project will deploy tailored strategies for the residential sector and the utility sector with the final aim of improving the hosting capacity and increase stability.

TRUST PV includes research partners from several countries such as Italy, Belgium, Cyprus, Germany, Greece, Lithuania, France, Netherlands, UK. The PVMD group of TU Delft will mainly be responsible for the following research:

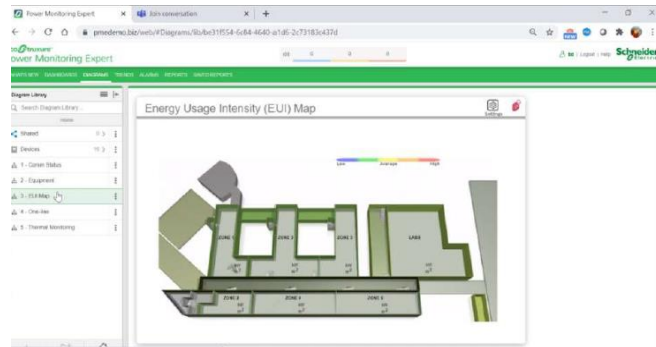
1. Integrated yield and reliability modelling framework based on 4 levels of details approach of the PVMD group
2. Short and mid-term advanced PV system energy forecasting and fault detection by digital twinning using artificial intelligence techniques.
3. Improving the reliability of floating PV systems and validating their operational behavior with
4. respect to ground-mount PV systems.





(a) Dashboard view of the PME showing total energy Production

(b) Mapping the production data over the physical stations



(c) Analysis of different loads connected to the station with power

(d) The network architecture from solar panels, inverters, etc.

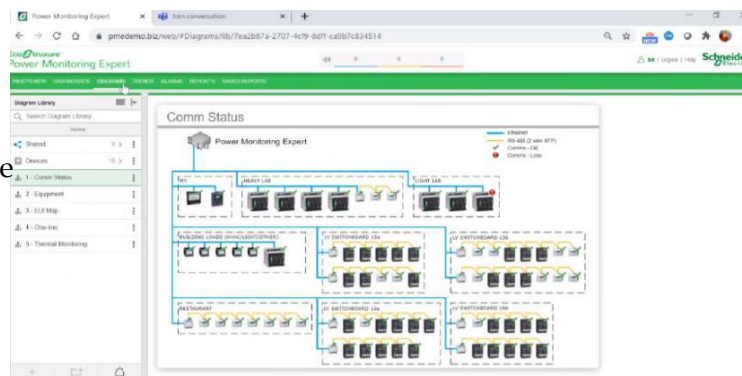


Figure 5 Different capabilities of Electric Schneider ExoStruxure

## 1.3 Research Aim and Scope

This research is done on an installed photovoltaic station by Empower Energy and Systems with a cooperation with Center of Nanoelectronics and Devices to develop an IoT system for monitoring photovoltaic stations. The physical layer (including panels and sensors) of the IoT system beside the communication layer underwent several stages of development. The target of this research is to lay a solid foundation of data analysis module that can detect operational faults of solar panels. The analysis module must be able to assure that data received from sensors make sense and be able to detect several faults and can use it later for decision making. This data insight is highly valuable in analysis of solar panel measurement data.

This thesis will be organized as follows:

- The second chapter will give an overview of available solar cell technologies and the basic physics behind the operation of solar cells and their equivalent circuit model. Furthermore, normal ranges of parameters found in datasheets will be demonstrated.
- The third chapter will overview several panel faults as reviewed from the literature; we will focus on faults that can be diagnosed from current-voltage characteristics of solar panel.
- The fourth chapter will lay a foundation for a solar cell modelling approach that we will use extensively in doing our analysis. Before modelling the solar panel, we model the environmental conditions surrounding it then we see how variation of environment affects solar panel performance.
- The fifth chapter will discuss the specifics of the installed site and a detailed description of the developed analysis module and its capabilities.
- The sixth chapter will analyze actual datasets produced in several stages of developing the installed station. The limitations of photovoltaic characterizers will affect how we can deal with given datasets. The powerfulness of developed mathematical models will help understand behavior of solar panels under various environmental conditions. Besides, several methods will be proposed and investigated for data analysis.
- Finally, a conclusion will be given about the whole work summarizing all points.



# Chapter 2

## Solar Cell Basics

The photovoltaic effect is the key concept behind solar cells and to understand this effect we need to detail the structure of a typical solar cell. In 2008, 38% of produced solar cells were made of monocrystalline silicon and 48% were from polycrystalline silicon [13] and newer solar cell technologies have same operation principles of the types. As we focus on both monocrystalline and polycrystalline solar cells, we begin to detail their structure.

## 2.1 Contemporary Solar Cell Technologies

From an industrial point of view, several technologies exist in the market of solar cells, depending mainly on the physical structure of the solar cell itself. We talk here about different technologies available in the market.

Three different generations of solar cell technologies exist in the market [14]. The first contains solar cells that are relatively expensive with good efficiency, the second has lower efficiency and lower cost per watt and as for the third generation, it includes solar technologies not commercialized yet with greater efficiency and lower cost [15].

### 2.1.1 First-generation solar cells

Crystalline silicon solar cells are over 80% of photovoltaics in the market [15]. They are single-junction solar cells where the bulk material crystalline silicon wafer between 160 and 240 micrometers thick.

#### 2.1.1.1 Monocrystalline silicon solar cell

Monocrystalline silicon solar cells are the industry standard for so many reasons. Firstly, the longevity of the cell is outstanding as there are still some solar panels operating since 1970's, some can last as long as 50 years with a loss of only 0.5% in efficiency per year [14]. In addition, most performance warranties go for at least 25 years. Also, they are environmentally cleaner than other panels that hold toxic materials like cadmium.

Industrially, the fabrication process is very time consuming, and many cells are so fragile and can be easily damaged. Monocrystalline panels have separated cells interconnected externally (as shown in Figure 6) on the contrary to polycrystalline panels for

instance.



Figure 6 Monocrystalline panel with cells separated

Several structures exist in fabrication of monocrystalline solar cells as shown in Figure 7 (as adopted from [13]) The most common type is the passivated emitter rear localized, **PERL**, structure [16]. In such structure, silicon solar cell is sliced from a column ingot produced by Czochralski process [13]. In such process silica containing impure silicon is purified to have highly crystalline silicon. The sliced wafer is p-type doped with boron. Donor ions, phosphorus in this case, bombard the wafer to provide a thin n-type layer at the top of the cell. Afterward, the surface is passivated with a thin layer of silicon dioxide and then being etched before metal fingers are deposited to collect current from the solar cell. The top surface of solar cell has pyramidal grooves to trap incident light upon the solar cell. On the back side, rear contacts are deposited after localized doping of acceptor ions. **PERL** is the most common structure to be used in laboratories and in industry [13].

Second structure is heterojunction with intrinsic thin layer, **HIT**[17]. The **HIT** cell is a n-type crystalline silicon wafer sandwiched between two intrinsic layers of amorphous silicon sandwiched again between p or n-type amorphous silicon layers and instead of passivated surface a transparent conductive oxide, **TCO**, is utilized to form contact between grid fingers and solar cell itself.

Third structure back contact -back junction cell, **BC-BJ**, a p-n junction is formed at the rear of the solar cell exactly above deposited contacts. The bulk of the solar cell is n-type silicon wafer. However passivated surface is covered by an anti-reflective coating, **ARC** to absorb sun irradiance to the maximum.

Fourth structure is a variation of third structure but when the back contact is not a rectangular grid rather than an interdigitated grid lines and it is called interdigitated back contact, **IBC**, cell.

Last but not least, buried contact cell is similar to **PERL** structure but with surface contacts are buried inside to grid line shadowing. It is shown in Figure 7 that all these cell structure has

an internal p-n junction formed either with single crystal as in Figure 7, (a, c, d, e) or as a hetero p-n junction as in Figure 7, (b). Furthermore, metal contacts either formed on surface directly or after the addition of TCO provide a source of current resistance in the solar cell. Actually, the use of TCO in HIT cells is mainly to reduce the sheet resistance of the amorphous silicon.

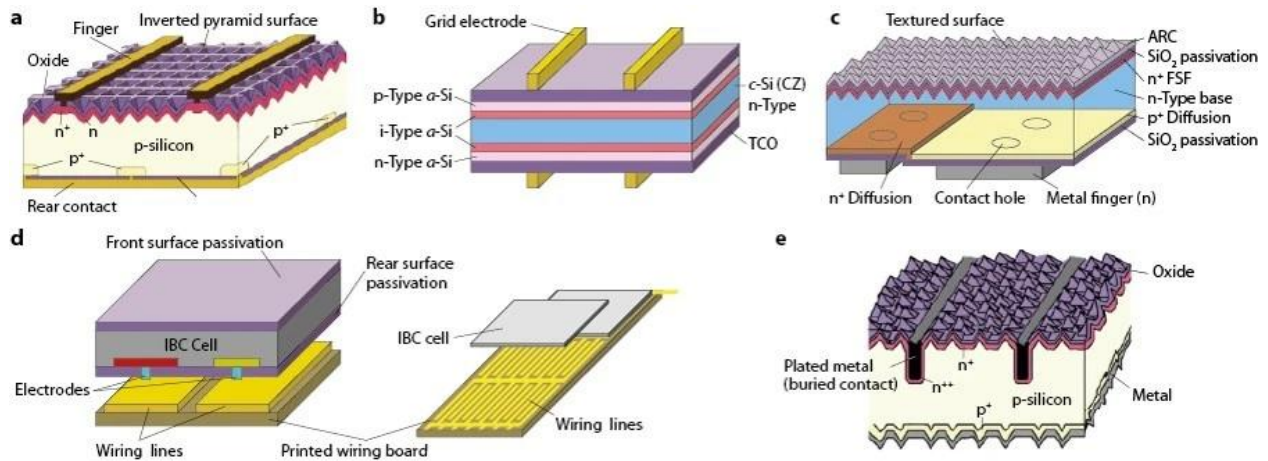


Figure 7 Structure of different monocrystalline silicon cells (a) PERL cell, (b) HIT, (c) BC-BJ, (d) IBC and (e) buried contact structure

To enhance the absorption of solar cells manufacturers, try to maximize area subject to sunlight by depositing narrower grid lines like in HIT cells, or use textured surfaces with back electrodes as in BC-BJ cells. However, the production of such cells is costly compared to PERL cells, so it remains the dominant structure for monocrystalline solar cell. Some manufacturers use n-type wafers to build the cell as it is less sensitive to light-induced-degradation, LID [17] which occurs when boron dopants recombine with oxygen at the air due to carrier photogeneration.

### 2.1.1.2 Multi-crystalline silicon solar cells

Multi-crystalline silicon solar cells are the most common solar cells because they are cheaper than monocrystalline cells and they are middle choice in terms of power (which is 70% of monocrystalline cells) and cost. They are durable almost as monocrystalline cells and they have mosaic color due to differently-oriented crystals they are made of as shown in Figure 8.



Figure 8 Mosaic shaped multi-crystalline solar cells

Most structures adopted for monocrystalline cells are used for polycrystalline ones but with poorer power production. The amount of power produced per unit area is related to the carrier lifetime relative to cell thickness. For polycrystalline cells, cell thickness is reduced to minimize cost and to keep the relative carrier lifetime as high as possible. Several structural modifications are common to mitigate carrier lifetime losses.

Kyocera [17] introduced the metal-wrap-through, **MWT**, structure for polycrystalline silicon cells which is depicted in Figure 9 (a) (as adopted from [13]). In such structure, beneath each negative bus bar there is a hole leading to the back surface. The presence of such wrap-throughs increases the lifetime of electrons around the n-doped region which in turn enhances current production.

Other companies as well like ECN, Advent Solar introduced the design of emitter-wrap-through, **EWT**, structure as shown in Figure 9 (b). The advantage of **EWT** is that it eliminates most of bus bars at the top and instead n-regions are connected to laser-drilled metal holes. Such design increases power production by exposing larger area and by increasing carrier lifetimes as well.

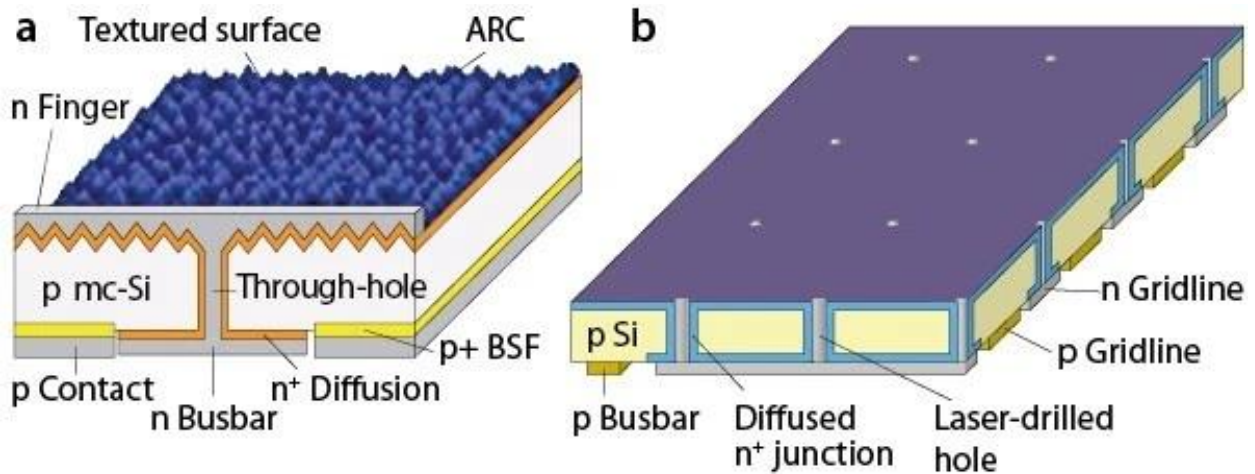


Figure 9 (a) Metal-Wrap-Through cell, **MWT**, (b) Emitter Wrap-Through, **EWT**, Solar Cell

## 2.1.2 Second-generation solar cells

### 2.1.2.1 Thin-film solar cells

This technology reduces the amount of active material in a cell creating compared to silicon ones[18]. Most designs sandwich active material between two panes of glass. Such cells can be formed of a hetero-junction like cadmium telluride, CdTe and copper-indium-gallium selenide, CIGS, or a p-i-n junction just like amorphous silicon. The efficiency for these modules is not the best but they are cheaper than first-generation counterparts.

CdTe cells account for 5% of cells produced worldwide, however it is a highly toxic material which adds industrial hazards to using it. A possible replacement for CdTe cells is CIGS as it is non-toxic and gives best conversion efficiency among all commercial thin-film technology. Another interesting feature in CIGS is its strong thermal stability compared to other thin-film cells.

The most developed thin-film technology is amorphous silicon, and it has existed in the market for over than 20 years. The uniformity of amorphous silicon thin films compared to other materials make the cells more reliable. Another technology is based on Gallium-Arsenide, GaAs where solar cells are mainly single-crystalline thin films that has can be used either in single/multiple-junction solar cells. Interestingly, they are relatively insensitive to heat.

### 2.1.3 Third- generation solar cells

Multijunction solar cells offer high reliability, a high power-to-mass ratio, excellent radiation hardness, small temperature variation, and the possibility to operate at high voltage and low current. Simply, they are multiple thin films cascaded and grown on top of one another. Each layer has a different band gap energy to allow it to absorb electromagnetic radiation over a different portion of the spectrum. Multi-junction cells were originally developed for special applications such as satellites and space exploration. Other technologies for solar cells include organic solar cells (e.g., dye-sensitized solar cells) and quantum dot cells [19].

### 2.1.4 Comparison of solar cell technologies at the state of the art

In [20], authors compared different generations of solar cells.

#### 2.1.4.1 First Generation

Included monocrystalline and polycrystalline silicon solar cells, beside GaAs monocrystalline cells. 90 % (as of 2022) of the market are first generation cells.

Advantages:

- Longest warranty, commercial warranty is 25-year long,
- Monocrystalline perform well under low irradiance,
- Polycrystalline are fabricated through melt-and-pour process which is easier than monocrystalline ones.
- Polycrystalline are cost effective and has 12% average efficiency
- 

Limitations:

- Comparatively expensive,
- Massive silicon losses at fabrication process of monocrystalline silicon as silicon wafers are cut,
- High temperature affects polycrystalline cells compared to monocrystalline ones,
- Silicon purity is limited in polycrystalline cells so efficiencies in 13-16% range,

#### 2.1.4.2 Second generation

Made mainly of amorphous (a-Si) and microcrystalline ( $\mu C$  -Si) silicon thin films, beside Cadmium telluride, CdTe, Cadmium sulfide, CdS and Copper indium gallium selenide, CIGS.

Advantages:

- Some cells are physically flexible, so they are widely applicable to different type of building.

- Relatively easier to produce.

Disadvantages:

- Shorter lifespan compared to first generation cells
- Some cells has poisonous materials which implies safety issues.

### 2.1.4.3 Third generation

It includes cells done from organic materials, perovskite cells, die sensitized solar cels, DSSC's, Quantum-dot cells and multijunction cells.

Organic photovoltaics need donors and acceptors with high extinction coefficients and good stability compared to silicon counterparts. Besides, their measured lifespan is shorted than expected by manufacturers.

Perovskite materials are based on minerals like calcium titanium dioxide  $CdTiO_2$ . Perovskite solar cells are prepared with solution-based methodologies after being processed with tin or a halide. First version of using intermediate perovskite layers showed little efficiency as 4% but currently the maximum recorded efficiency is 29%.

DSSC's have very long lifespan than crystalline silicon devices. They can reach maximum of 12% efficiency with Ru(11) dye.

Quantum-dot solar cells provide greater control over the bandgap of included materials, hence a great control over its electrical properties. Dots can have surface defects or electron traps. Silicon doping of such cells shifts up their efficiency from 11.3% to 17%.

From a commercial point of view, (based on Figure 10 which is adopted from [20]), first generation solar cells has cost per power rate lesser than  $\$1/W$  and spans large variation of cost per  $m^2$  and approximately, efficiency below 20%. However, second generation solar cells have lower cost per are below  $100\$/m^2$  as well as cost per power between  $\$0.5/W$  and  $\$1/W$  and approximately the same range of efficiencies is achieved compared to first generation cells. For the third generation cells, cost per area is wider compared to second generation but also larger efficiency and lower cost per power between  $\$0.5/W$  to  $\$0.1/W$ .

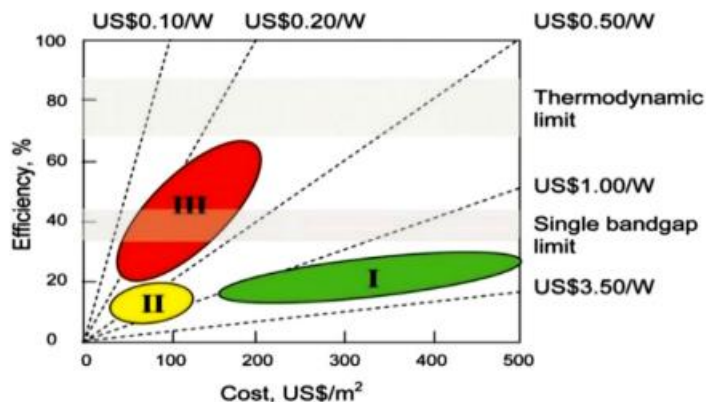


Figure 10 Cost efficiency of different solar cell generations

According to National Renewable Energy Laboratory (see Figure 11 adopted from [20]), a comparison was made between different solar cell technologies (as tested in research laboratories) in terms of achieved efficiency. From higher to lower, multijunction or single junction GaAs were first, then crystalline silicon cells, then thin firm technologies, and finally, emerging technologies,



like DSSC, Perovskite, and quantum dots came at the end. Multijunction solar cell with ray concentrator developed by NREL in 6J143x project achieved the record of 47.1% efficiency.

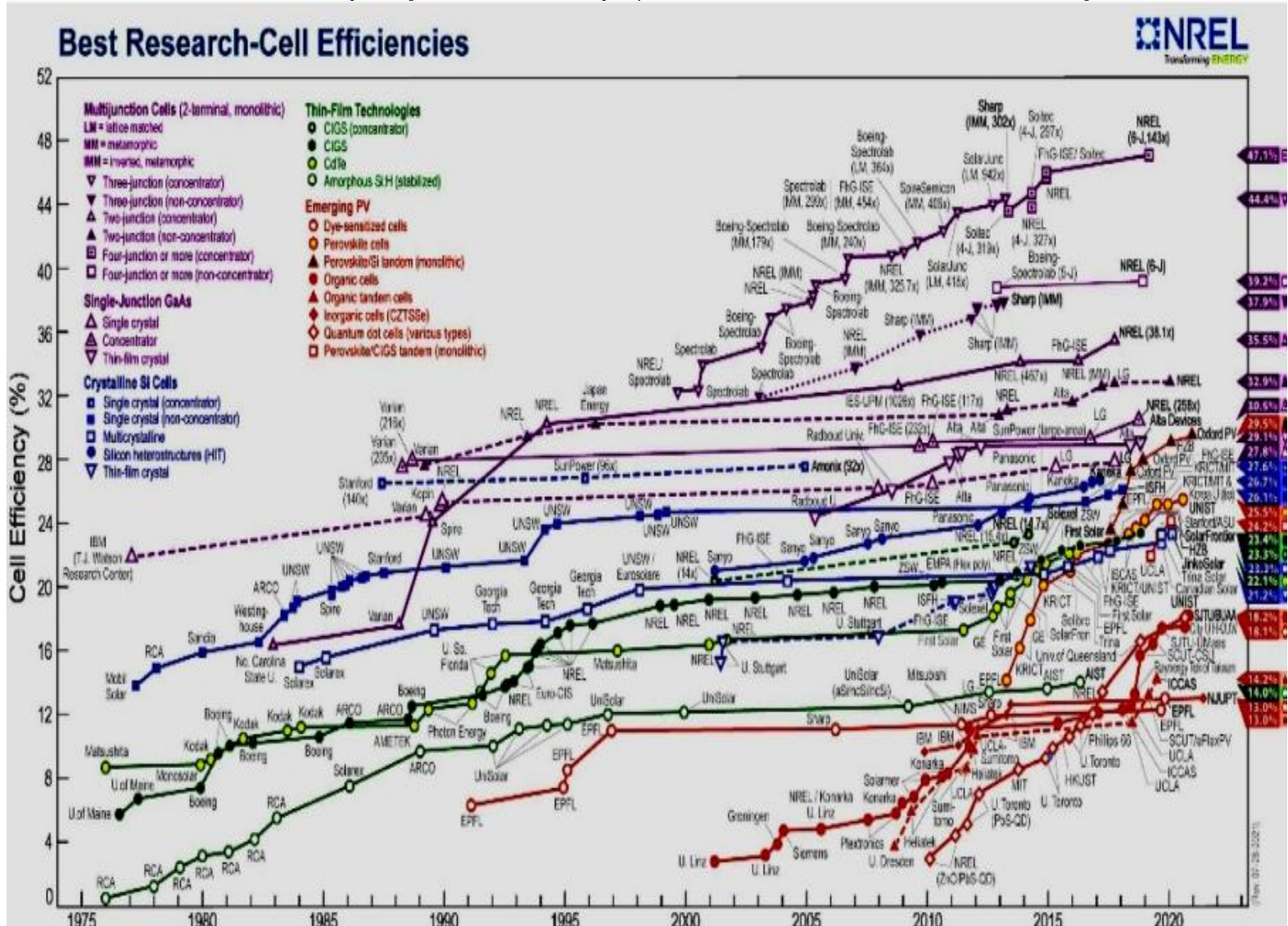


Figure 11 Development of solar cell efficiencies evolution through time for different technologies

## 2.2 Solar Cell Physics

The photovoltaic effect is the key concept behind solar cell operation. As shown from previous section in (Figure 7 and Figure 9)- solar cells are structurally a p-n junction with some modifications. So, we will show the theory of operation of p-n junction and how we can use them to model solar cells properly.

## 2.2.1 P-N Junction Revisited

A p-n junction is a stack of oppositely doped semiconductor regions- one doped with acceptors, p-region, and another one doped with donors, n-region. When we concatenate both regions together, we have a metallurgical junction called the p-n junction. For sake of simplicity, we presume that doping profile is an abrupt step at the junction itself as shown in Figure 12 (b)

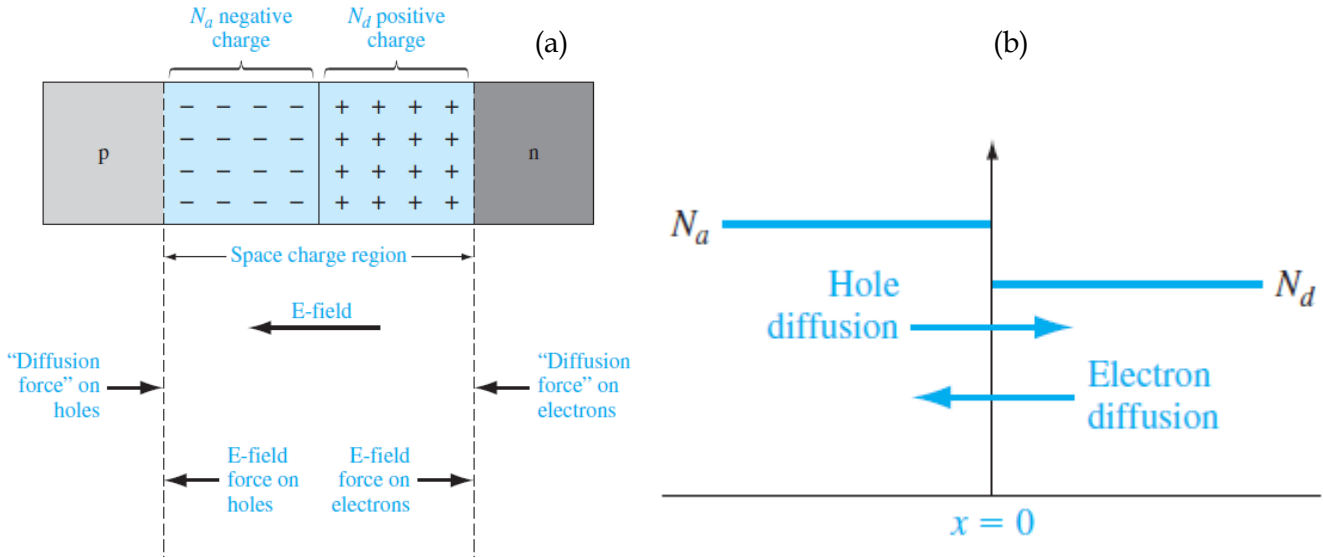


Figure 12 (a) p-n junction at equilibrium and (b) doping profile of step p-n junction. (as adopted from [21]).

Several assumptions are made to find the current-voltage, IV, characteristics of a regular p-n junction and they are as follows:

- The junction width (space charge region in Figure 12 (a)) is very narrow relative to the width of n or p regions [22] and negligible carrier recombination can occur at the junction.
- The dominant carrier transport mechanism is diffusion and electric field is confined to space-charge region even in nonequilibrium conditions [22]
- N and P regions are not heavily doped for such that carriers follow Boltzmann statistics instead of Fermi statistics [21], [22]
- All doping atoms are ionized and provide carriers [21]

At equilibrium, abundant electrons at the n-region move toward to the p-region, and likewise, abundant holes in p-region move toward the n-region, leaving out a place where no free carriers exist but only immobile ions. Consequently, an electric field is induced between both regions (as demonstrated in Figure 12) that opposes the motion of more carriers between both regions. The intensity of electric field can be found by solving Poisson's equation and it will be the maximum at the junction itself [21]. Afterward the built-in potential between both n and p regions can be expressed depending on doping concentrations as follows

$$V_{bi} = \frac{e}{2\epsilon_s} (N_d x_n^2 + N_a x_p^2) \quad (1)$$



As a result, the energy-band diagram of the p-n junction is bended at the junction itself and the Fermi level is continuous everywhere as shown in Figure 13 (as adopted from [21])

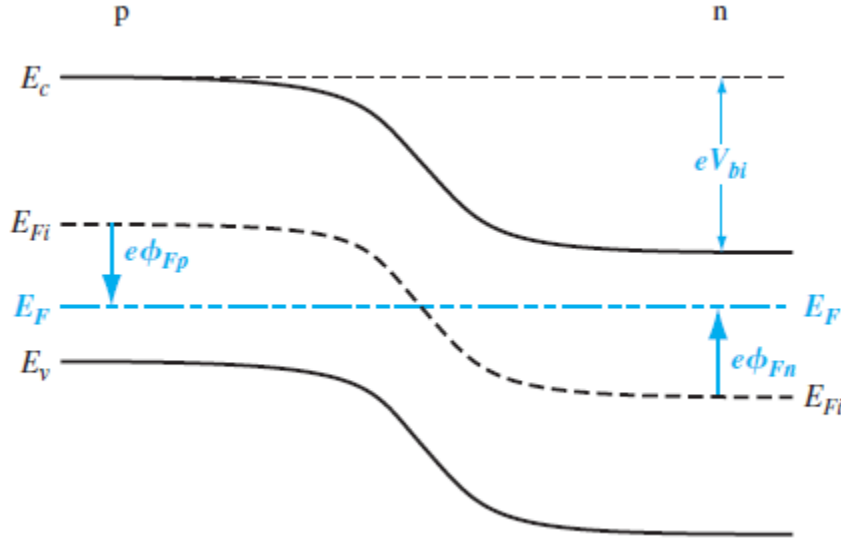


Figure 13 Energy-band diagram for a p-n junction

When an external potential  $V_a$  is applied to the p-n junction the potential barrier between p and n regions is reduced by becoming  $V_{bi} - V_a$  and the Fermi level is broken into two different Fermi levels for each region  $E_{Fp}$  and  $E_{Fn}$  namely. The reduction of potential barrier facilitates the diffusion of carriers between n and p regions where excess minority carriers diffuse from either p or n region to the other region. The diffusion of both carriers is called ambipolar transport and it is governed by (2) in the n region

$$D_p \frac{\partial^2(\delta p_n)}{\partial x^2} - \mu_p E \frac{\partial(\delta p_n)}{\partial x} + g' - \frac{\delta p_n}{\tau_{p0}} = \frac{\partial(\delta p_n)}{\partial t} \quad (2)$$

As we assume that that the electric field is confined within the space charge region and with a dominant diffusion transport, we neglect the electric field term; also the time derivative is neglected for a steady-state solution and we have  $g' = 0$  so for n region (2) is reduced to (3) and like wise for excess minority carriers in p region we have (4)

$$\frac{d^2(\delta p_n)}{dx^2} - \frac{\delta p_n}{L_p^2} = 0 \quad (x > x_n) \quad (3)$$

$$\frac{d^2(\delta n_p)}{dx^2} - \frac{\delta n_p}{L_n^2} = 0 \quad (x < x_p) \quad (4)$$

Solution of (3) and (4) with proper boundary conditions based on Boltzmann carrier statistics can

find excess carrier concentrations. Hence the diffusion current at space-charge region boundary can be found as in (5). Finally, the famous diode equation[21] can be found as (6). It is noteworthy that the current  $J_s$  called reverse or saturation current is the current passed through the junction when the p-n junction is reverse biased.

$$\begin{aligned}
 J_p(x_n) &= -eD_p \left. \frac{dp_n}{dx} \right|_{x=x_n} \approx -eD_p \left. \frac{d(\delta p_n)}{dx} \right|_{x=x_n} \\
 J_n(-x_p) &= eD_n \left. \frac{dn_p}{dx} \right|_{x=-x_p} \approx eD_n \left. \frac{d(\delta n_p)}{dx} \right|_{x=-x_p} \\
 J &= J_p(x_n) + J_n(-x_p)
 \end{aligned} \tag{5}$$

$$\begin{aligned}
 J &= J_s \left( \exp \left[ \frac{eV_a}{kT} \right] - 1 \right) \\
 \text{where } J_s &= \left[ \frac{eD_p p_{n0}}{L_p} + \frac{eD_n n_{p0}}{L_n} \right]
 \end{aligned} \tag{6}$$

In real p-n junctions, the diffusion mechanism is not always the dominant mechanism in carrier transport so in terms of current instead of current density one can say that

$$I = I_s \left[ \exp \left( \frac{eV_a}{n k T} \right) - 1 \right] \tag{7}$$

In (7), the term  $n$  is called the ideality factor and it equals 1 for large forward-bias voltage where the diffusion mechanism dominates, and it equals 2 when the recombination dominates the performance of a p-n junction so in general  $1 \leq n \leq 2$ . The choice of proper  $n$  must fit the IV the measured IV characteristics of a fabricated p-n junction [21].

### 2.2.2 Solar cell as a p-n junction

Beginning with the solar cell at equilibrium conditions as a p-n junction whose energy band diagram is shown in Figure 13. Carriers do not move from valence band to conduction band at thermal equilibrium except with four different mechanisms[23]: thermal generation, radiative generation, carrier-carrier generation, and impurity-and-surface generation.

In thermal generation, thermal energy given to electrons in valence band is given to promote them to move within the conduction band leaving equal number of holes behind and when energy drops electrons relax into lower states in a thermal recombination process. In an intrinsic doped semiconductor, the number of intrinsic carriers is related to temperature and the intrinsic density of states  $N_v, N_c$  in both bands so

$$n_i^2 = N_c N_v \exp \left( - \frac{E_g}{kT} \right) \tag{8}$$

In radiative processes, photons incident with energy equal to or greater than the bandgap of the semiconductor interacts with electrons in the semiconductor itself in various manners. First, photons can excite electrons to move from valence band to conduction band leaving a hole behind which is called “simulated absorption”. Second, photons can excite electrons in conduction band to relax into lower states giving a photon in “simulated emission”. Last, electrons in conduction band can relax into lower states and emit photons in “spontaneous emission”. Figure 14 (adopted from[23]) demonstrates the three different radiative processes. In case of solar cell, we are interested in simulated absorption to produce photocurrent[23].

In carrier-carrier generation, high energy electrons can promote electrons from lower states into upper states by scattering. However, this process is low probable except in highly doped semiconductors. The reverse process is called Auger recombination. This generation/recombination process is responsible for the performance of solar cells when electron energy is sufficiently high [23].

For impurity and surface generation/recombination it is noted that in real-world solar cells, semiconductor crystal lattice cannot be repeated infinitely without any defects or discontinuities. Additionally, semiconductor crystal has various impurities at the surface between different materials. Both crystal defects and impurities induce minor energy levels in the forbidden gap which act as carrier traps so either thermal lattice vibrations or photon interactions contribute to the movement of carriers into these traps. In generally thermal vibrations are the dominant carrier generation and recombination mechanism there so the whole process is nonradiative. When no photon is incident, carriers settle at these traps until a thermal vibration releases them or a carrier of another polarity recombines at these traps. The number of electrons at conduction band and density of traps determine rate of recombination. Such recombination termed “Shockley-Read-Hall Recombination” impedes carrier transport and drops cell efficiency considerably [23].

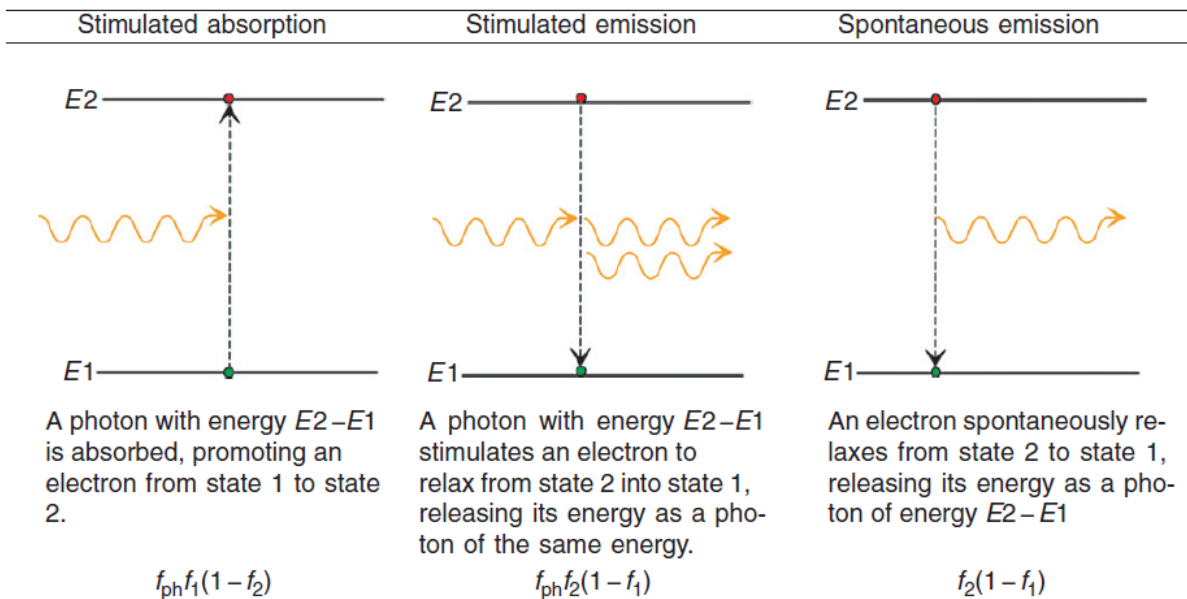


Figure 14 Three different radiative processes in semiconductors, here  $f$  denotes the probability density function of particle at energy level either it is a photon or an electron

The energy band diagram of a simple p-n junction solar cell is shown in Figure 15 (adopted from [24]) and several regions of interest exist. First, from  $-d \leq x \leq 0$  which is the top p-type region where photons fall. Second, from  $0 \leq x \leq W$  which is p-n junction barrier region. Last, the bottom n-type layer from  $W \leq x \leq W + L$ .

Photogenerated carriers can recombine at bulk regions using mainly Shockley-Read-Hall recombination/Auger recombination as shown in Figure 15 mechanisms 1 (at p-region), 4(at junction region) and 5 (at n-region). Similarly, greater recombination occurs at the ohmic contact formed at p-type region (mechanisms 2 and 3), and at the n-type region (mechanisms 6 and 7). Both mechanisms 3 and 6 occur in the forbidden gap while mechanisms 2 and 7 occur in the metal side of the ohmic contact.

The current produced at any specific voltage is given by integrating the number of available carriers overall the p-n junction and subtracting the carrier loss due to bulk and surface recombination as shown in (9). The term  $G_{ph}(\lambda, x)$  is the photogenerated carriers of specific wavelength and at a specific depth  $x$  (if photogeneration decreases as we go deeper in the solar cell). Besides,  $R, J_{ST}$  and  $J_{SB}$  resemble the losses at bulk, top p-type region and bottom n-type region respectively.

$$J = e \int_{-d}^{L+W} \int_{\lambda} G_{ph}(\lambda, x) d\lambda dx - e \int_{-d}^{L+W} R(x) dx - J_{ST}(-d) - J_{SB}(L + W) \quad (9)$$

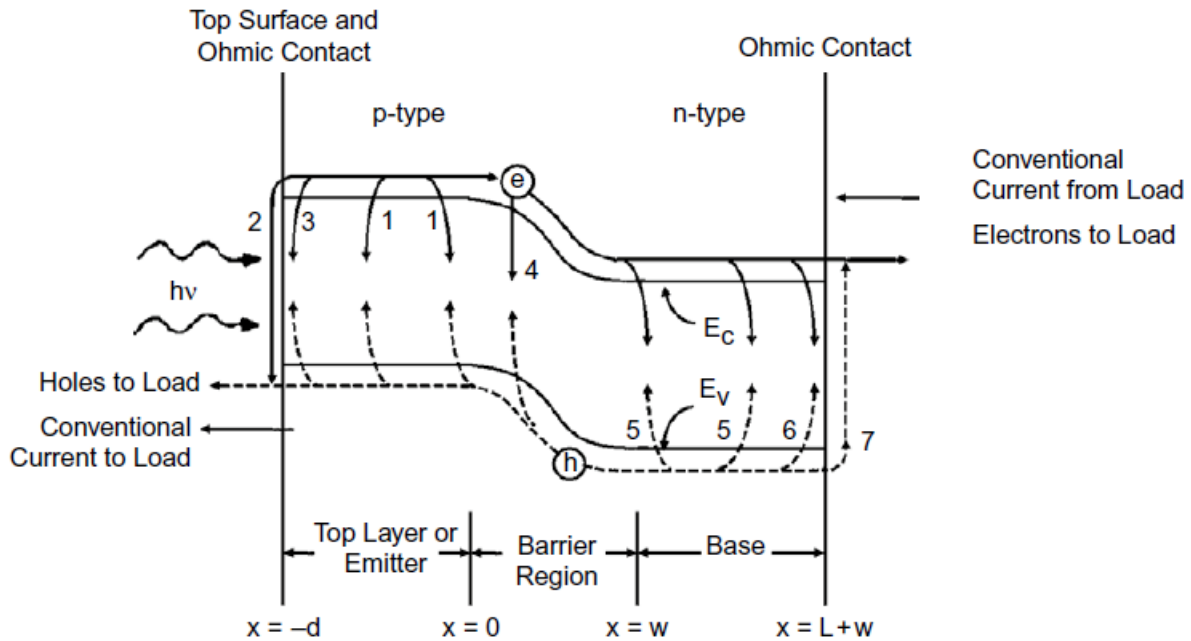


Figure 15 Energy band diagram of simple p-n junction solar cell with different loss mechanisms numbered from 1 to 7

Equation (9) shows the direct dependence of current on the incident irradiance spectrum and on the efficiency of the solar cell in utilizing such spectrum.

### 2.2.3 Derivation of Single-Diode Model

Based on the underlying physics of solar cells, we can derive the solar cell single-diode model, **SDM** which includes an irradiance-dependent current source, diode (p-n junction) and a series which is the total resistance along the current flow path including contacts and resistivity across the silicon itself and a parallel resistance accounting for the leakage current in the p-n junction [25]. A depiction of the single diode model is shown in Figure 16.

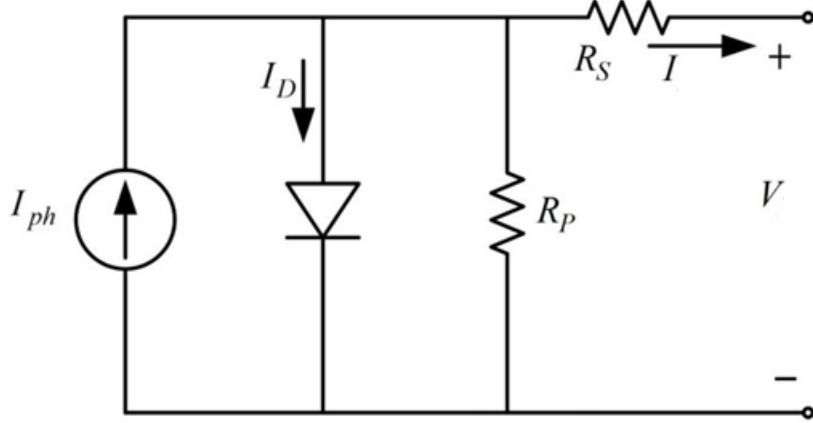


Figure 16 Single Diode Model of Solar Cell

In the **SDM**,  $I_{ph}$  is the photocurrent from the incident irradiance,  $I_D$  is the diode current,  $R_p$  and  $R_s$  are the parallel and series resistances respectively. Consequently, one can find the IV characteristics of the solar cell from Kirchhoff's laws as follows.

$$I_{ph} = I_D + I + \frac{V + IR_s}{R_p} \quad (10)$$

and based on (7), one can extend the  $I_D$  term and reorganize (10) to be as follows.

$$I = I_{ph} - I_0 \left[ \exp \left[ \frac{e(V + IR_s)}{nkT} \right] - 1 \right] - \frac{V + IR_s}{R_p} \quad (11)$$

where  $I_0$  is the reverse saturation current of the p-n junction and it is called dark current at short-circuit point as when the photocurrent is zero (no irradiance is incident on the solar cell) and with infinite parallel resistance and zero series resistance (i.e., no significant loss mechanisms) the value of current at zero voltage (a.k.a. when the solar cell is short-circuited) is  $-I_{dark}$ . The following IV characteristics as shown in Figure 17 are obtained when the values of parameters in the **SDM** (circuit parameters) are as in Table 3 using MATLAB script found in [26].

Table 3 Example solar cell circuit parameters

Parameter	Value
$R_s$	10 mΩ
$R_p$	1MΩ
$n$	1.1
$I_{ph}$	9 A

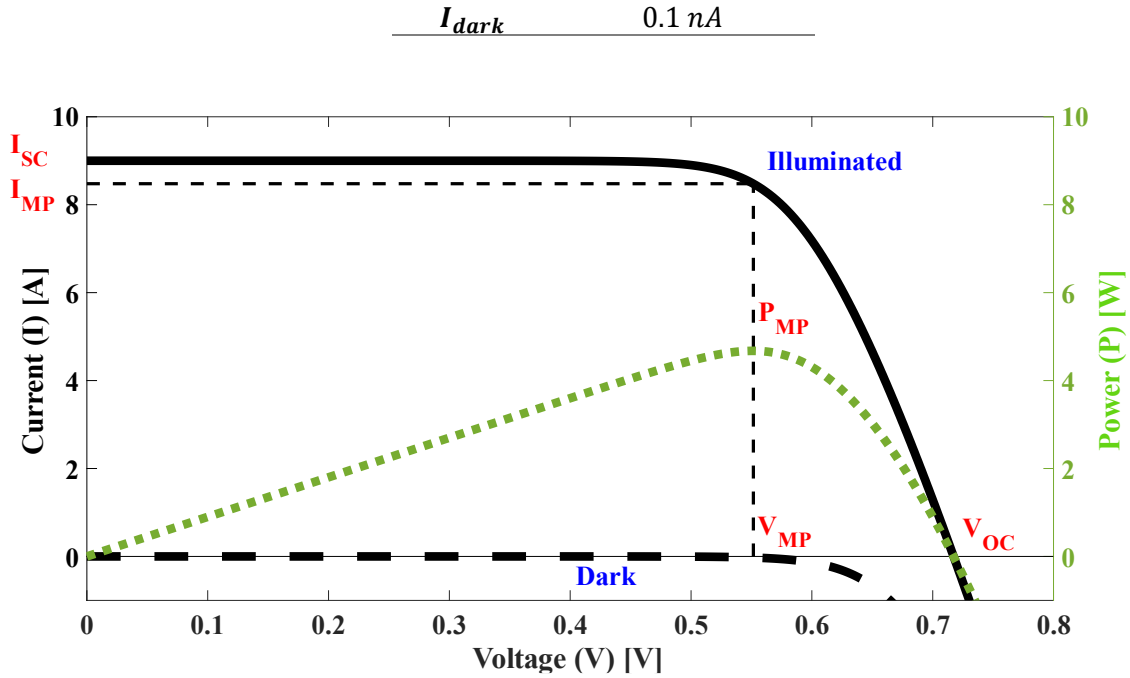


Figure 17 IV characteristics of a solar cell when illuminated (solid black), dark (dashed black) as well as the power generated (green).

In Figure 17, it is shown that when no photocurrent exists (i.e., no irradiance at all) the panel has the dark current value as an output current at various voltages, however, at higher voltages, the solar cell acts as a load (the output current changes sign) which is interesting enough that solar cells, then, do not act as power-generators anymore. In contrast, when the solar cell is illuminated, output current passes then it decreases smoothly at higher voltages.

#### 2.2.4. Industrial Parameters

Several parameters of interest arise naturally from the IV characteristics and are found in datasheets of commercial solar panels that we call industrial parameters. First, the short-circuit current, which occurs when both terminals of the solar cell are connected without any load in between we note it as  $I_{SC}$ . The second parameter is open-circuit voltage,  $V_{OC}$  which is the maximum voltage after which the solar cell begins to act as a load not as a generator. The third parameter is the maximum power the solar cell can generate  $P_{MP}$  and the remaining parameters are  $V_{MP}$  and  $I_{MP}$  which are the voltage and current at which the solar cell generates maximum power. The former two parameters can find the load resistance that can draw the maximum power of the cell  $R_L = V_{MP}/I_{MP}$  which is important to design maximum power point trackers **MPPTs** that ensure maximum utilization of solar cell power using proper DC/DC converters[27]. In addition, an interesting factor can be added to assess the performance of a solar cell compared to an ideal power generator is called the fill factor,  $FF$ . In ideal generator, the source delivers the same current  $I_{SC}$  for all voltages up to the open-circuit voltage[24],  $V_{OC}$  so to measure this rectangularity we define  $0 \leq FF \leq 1$ . Additionally, cell conversion efficiency,  $\eta$ , measures how much of incident solar irradiance is delivered as power. All these parameters are shown in (12), here  $Irr_{max}$  is the maximum irradiance incident on solar cell in  $W/m^2$  and  $A$  is cell area.

For cell with circuit parameters shown in Table 3, the corresponding industrial parameters

are shown in Table 4.

$$\left\{ \begin{array}{l} I_{SC} = I | V = 0 \\ V_{OC} = V | I = 0 \\ P_{MP} = P | \frac{dP}{dV} = 0 \\ V_{MP} = V | P = P_{MP} \\ I_{MP} = I | P = P_{MP} \\ FF = \frac{V_{MP} I_{MP}}{V_{OC} I_{SC}} \\ \eta = \frac{P_{MP}/A}{Irr_{max}} \end{array} \right. \quad (12)$$

Table 4 Industrial parameters of cell with circuit parameters in Table 3

Parameter	Value
$I_{SC}$	9 A
$V_{OC}$	0.7167 V
$P_{MP}$	4.6758 W
$V_{MP}$	0.5516 V
$I_{MP}$	8.4776 A
$FF$	0.7249

The efficiency of solar cell depends on the optical properties of the cell material and as a radiative process it is bounded by the energy gap of the semiconductor. The quantum efficiency of solar cell is measured when both terminals of the cell are shorted, and the transmitted current is measured after impinging photons with specific wavelength on the solar cell. The graph is then normalized to the maximum current value as shown in Figure 18 (adopted from [28] for monocrystalline type of solar cell). It is shown that each cell has a bandwidth of irradiance that limit photogeneration in (9).

### 2.2.5 Normal Industrial Parameters

The comparison of different solar cells usually occurs at standard test conditions, **STC**, which are normally  $Irr_{max} = 1000 W/m^2$ ,  $T = 298.15 K$  and AM1.5 spectrum as shown in Figure 34 and they are found in datasheets of most commercial solar cells.

The solar cell efficiency is a very important metric of solar cells. For a single-junction solar cell, Shockley and Queisser provided a theoretical limit for the efficiency known as Shockley-Queisser limit [29]. The following assumptions are true for such theoretical limit:

1. The cell temperature 300 K and the sun temperature is 6000 K and the incident irradiance is a blackbody irradiance obtained from (15) and shown in Figure 34.
2. The probability that a photon with energy larger than the energy gap enters the cell is 1

and the probability that it generates an electron-hole pair is 1.

3. All produced current is from photogeneration and no other generative process, fraction of radiative recombination to all recombination is  $f_c = 1$ .
4. Cell geometric factor: (depends on cell dimensions and distance from the sun) is  $2.18 \times 10^{-5}$ .
5. Phenomena like up-conversion[30], down-conversion and multijunction cell design[31] are not considered in our calculations. Which is widely acceptable for most of current solar cell technologies[32].

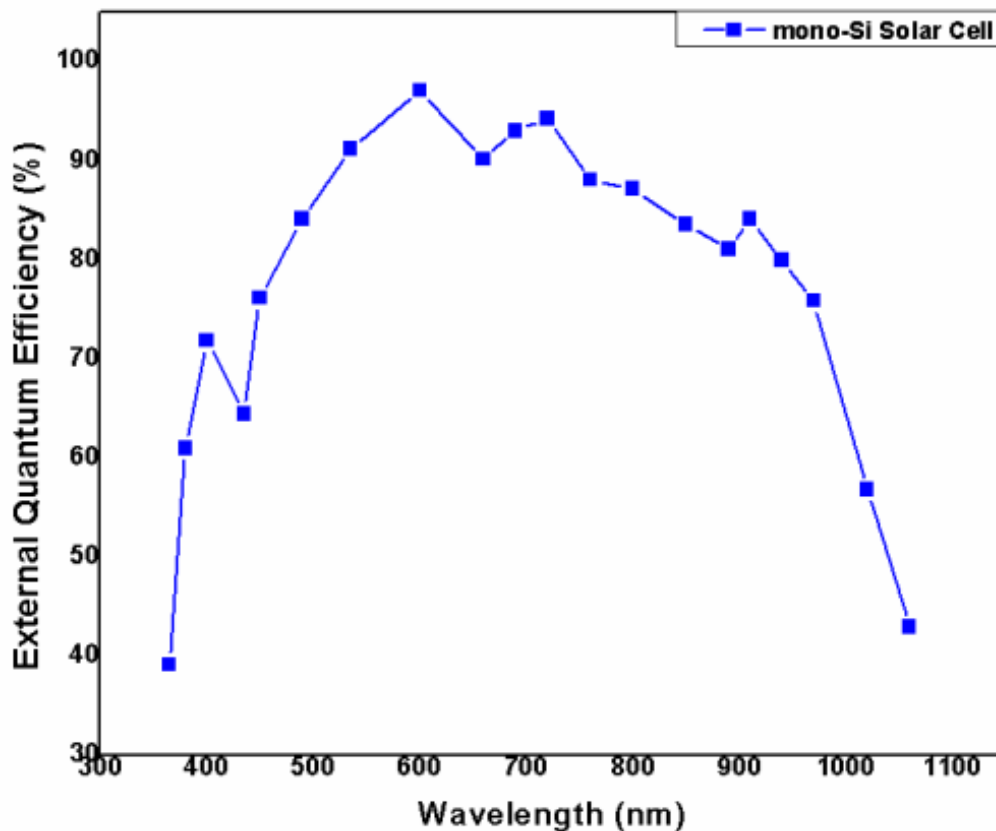


Figure 18 Quantum efficiency of Monocrystalline silicon solar cell based on normalized current at different wavelengths.

For practical purposes, the Shockley-Queisser approach was applied at common STC, where AM1.5 spectrum is used instead of blackbody approximation and at cell temperature of  $298.15\text{ K}$  and with assumption of ideal reflector at the cell rear (the condition no. 2 for Shockley-Queisser criteria). The maximum theoretical efficiency for AM1.5 radiation is plotted in Figure 19 against energy band gap (as adopted from [33]). It is noted that the maximum attainable efficiency is 33.36% instead of 30% for blackbody spectrum at the energy gap of  $1.36\text{ eV}$  instead



of 1.1 eV for blackbody spectrum. Of course, lower fractions of radiative recombination will deteriorate maximum attainable efficiencies.

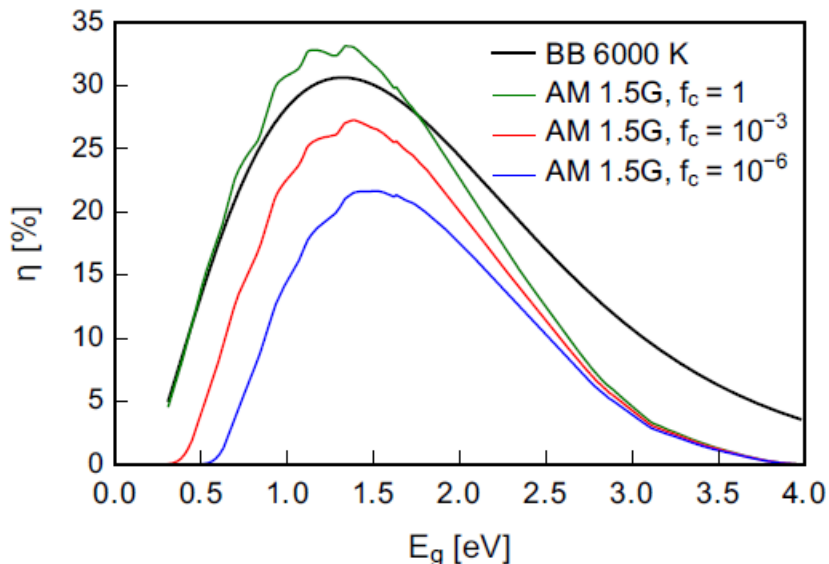


Figure 19 Shockley-Queisser Limit for efficiency assuming blackbody radiation with aforementioned criteria and with AM1.5 spectrum at several fractions of radiative recombination namely, 1,  $10^{-3}$  and  $10^{-6}$ .

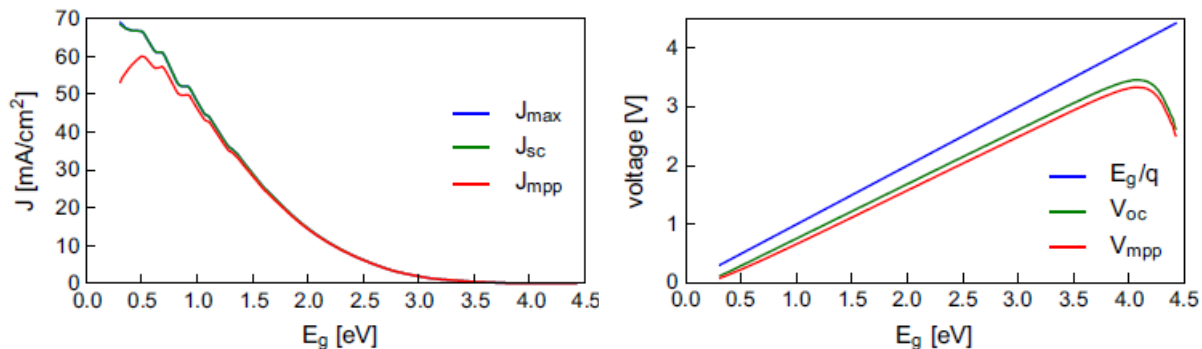


Figure 20 Shockley-Queisser limit for short-circuit current density and for the open-circuit voltage ratio  $eV_{oc}/E_g$

The limits of other industrial parameters are defined by the physics of the cell itself. For example, the maximum attainable open-circuit voltage is  $E_g/e$  [24]. The upper bound of  $I_{SC}/A$  and  $V_{OC}$  for a single cell as a function of bandgap are shown in Figure 20 (as adopted from [33]). For instance, for a single-crystalline silicon solar cells whose energy bandgap is 1.10 eV [32] we have the following upper-bounds on parameters as shown in Table 6. Besides, limits on industrial parameters in different technologies can be found in [33] compared to the best-manufactured solar cells [32]. For commercial solar panels (modules), the maximum conversion efficiencies are as shown in Figure 21 up to 2019, while most recent data (2021) that contain under-development uncommercialized cells- is found at [34]. However, it is noticeable that most commercial solar panels have efficiencies from 15% to slightly above 20% for the top crystalline-silicon solar

panels.

Table 5 Industrial Parameters for solar cells of different technologies ideally (based on Shockley-Queisser limit) or from best-manufactured cells. Here we assume  $c = 1$  and  $J_{SC} = I_{SC}/A$ . EQE is external quantum efficiency as shown in [32]**Error!**

Cell type	$E_g^{PV}$ (eV) <sup>a</sup> $((\frac{d}{dE}EQE)_{Max}$ (eV))	$V_{OC}$ (V)	$V_{MP}$ (V)	Cell type	$E_g^{PV}$ (eV)	$J_{SC}^{SQ}$ (mA cm <sup>-2</sup> )	$J_{SC}$ (mA cm <sup>-2</sup> )	$J_{MP}$ (mA cm <sup>-2</sup> )
<b>Single-crystalline materials</b>				<b>Single-crystalline materials</b>				
c-Si	1.10 (1.07)	0.74	0.66	c-Si	1.10	44.2	42.6	40.3
GaAs	1.42 (1.41)	1.13	1.02	GaAs	1.42	32.0	29.8	28.5
InP	1.38 (1.34)	0.94	0.82	InP	1.38	33.7	31.1	29.6
GaInP <sup>d</sup>	1.88 (1.84)	1.49	1.36	GaInP <sup>b</sup>	1.88	17.4	16.3	15.8
<b>Polycrystalline materials</b>				<b>Polycrystalline materials</b>				
mc-Si	1.11 (1.09)	0.67	0.57	mc-Si	1.11	44.1	41.1	39.1
CdTe <sub>1-x</sub> Se <sub>x</sub>	1.42 (1.42)	0.88	0.74	CdTe <sub>1-x</sub> Se <sub>x</sub>	1.42	32.0	30.2	28.3
CIGS	1.12 (1.12)	0.74	0.63	CIGS	1.12	43.8	38.8	36.4
CZTSS	1.13 (1.14)	0.53	0.39	CZTSS	1.13	43.4	33.6	29.1
CZTS	1.48 (1.46)	0.71	0.54	CZTS	1.48	29.6	21.8	18.7
ABX <sub>3</sub>	1.55 (1.55)	1.12	0.90	ABX <sub>3</sub>	1.55	27.3	24.9	22.2
<b>Other materials</b>				<b>Other materials</b>				
a-Si	1.77 (1.71)	0.90	0.73	a-Si	1.77	20.4	16.4	13.9
OPV (Toshiba)	1.62 (1.63)	0.78	0.64	OPV (Toshiba)	1.62	24.8	19.3	17.3
QD <sup>d</sup>	1.77 (1.78)	1.16	0.95	QD <sup>b</sup>	1.77	20.3	15.2	14

Table 6 maximal industrial parameters for a solar panel that has  $c$  cells and  $A$  total area

Parameter	$V_{OC}/c$ [V]	$cI_{SC}/A$ [mA/cm <sup>2</sup> ]	$V_{MP}/c$ [V]	$cI_{MP}/A$ [mA/cm <sup>2</sup> ]	$FF$	$\eta$
<b>Single-Crystalline Silicon</b>	0.87	44.1	0.76	43	0.85	0.3268

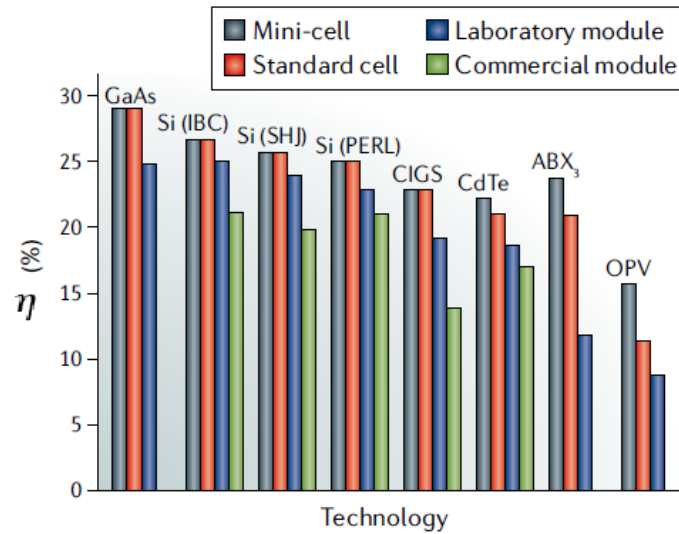


Figure 21 Efficiency of different solar technologies for minicells, standard cell size and for a whole panel (module)

## 2.3 Summary

To really understand the modelling of solar panels, one must overview the current technologies in solar panels which are classified into three different generations. The first generation provides monocrystalline and multi-crystalline silicon solar cells which have the greatest market shares until now. In the second-generation solar cells, we mentioned the thin film solar cells which are gaining commercial recognition right now and finally, the third generation includes multiple technologies that are still under research or were not commercialized greatly.

As we knew, the internal physical structure of a solar cell, we revisited the physics of PN junction, and how physically it is possible to model solar cell with help of the single-diode model (which is the model we will depend on in our analysis). Afterward, we introduced the different types of parameters that can be used to describe a solar cell (either parameters that are directly measurable that we call an industrial parameter) or parameters that we do not find directly and we call them circuit parameters. At the end, we investigate the physical limits of industrial parameters given a specific technology (A notion will help in identifying photovoltaic readings that make sense or not).

# Chapter 3

## Fault Classification and Diagnosis

In this part, a review will be given for several faults that can happen to solar power stations beginning from cell, panel (module of several cells), string (serially connected panels) and up to whole station. The focus of our work is to detect several electrical faults that usually happen to in-field solar panels. We depended on work from recent literature to gather information. The work at this part is divided chronologically into two phases. In phase 1, we investigated hotspot faults, their causes and detection methods and their economic plausibility. Besides, the effects of similar faults were investigated as well like shading effects on performance. All these investigations were based on proper understanding of solar panels electrical and physical models. In phase 2, our investigation pool widened to include other several faults (like line-to-line faults for instance) and to review how this data is analyzed afterward to differentially diagnose several faults. At the end we will limit our scope to faults that can be diagnosed with measuring the current-voltage characteristics only.

### 3.1 Comparative evaluation of fault detection approaches

This paper [35] reviews several faults that may occur in a PV array (several panel strings) interfaced to a load. It begins by listing all possible faults that may occur and classifies recent fault detection methodologies in literature. The paper provides a comparison between several works in the literature based on fault detection variables, possible indicated faults, procedural complexity of implementation and need for several sensors/ economic viability of these techniques. Additionally, the efficiency of whole classes of approaches is compared to provide insight in most efficient approaches.

The main faults reviewed by authors include LGF, LLF, AF, OC, SF, HS, BDF, DGF and GFC (line-to ground fault, line-to-line fault, arc fault, open-circuit fault, shading fault, bypass diode fault, degradation fault and general fault condition respectively).

All of these faults and other faults that may occur outside of the PV array are summarized in Figure 22. New faults like LLF, LGF occur due to misconnection between different panels whether in same string or in different one, or a misconnection between line and ground. Also, some faults are due to arcing and separation of some panels from the power network like OC and AF. There is less distinction between HS and SF in this review: in sense that whether hotspot is temporary or permanent. SF includes partial-shading conditions which is the uneven distribution

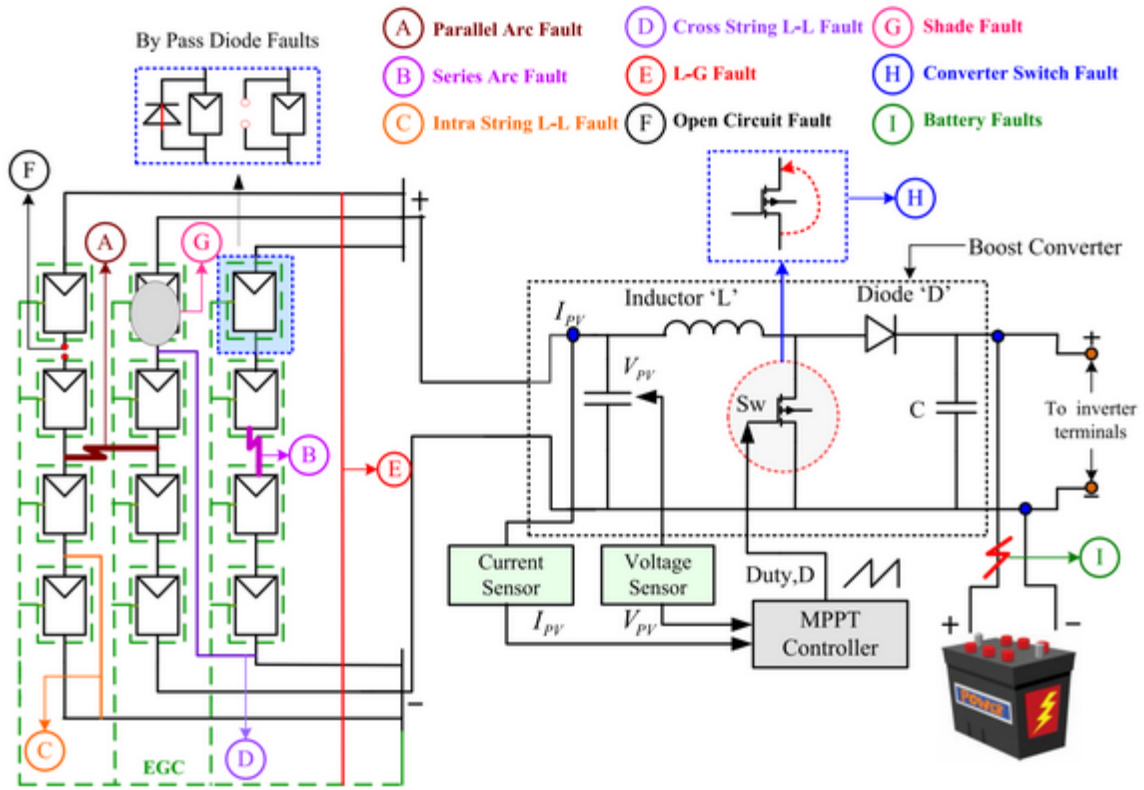


Figure 22 All possible faults encountered in a photovoltaic array

of shades over the PV array. It may occur due to building/tree shadows, passage of clouds and bird droppings or dust accumulation.

Authors classify different detection approaches to four classes:

- MBDM (model-based difference measurement)
- RDM (real-time difference measurement)
- OSA (output signal analysis)
- MLT (machine-learning techniques)

Figure 24 (adopted from [35]) summarizes the difference between these classes and their outline. In MBDM there is a parallel model of the system that computes decisive parameters and compares it to in-field parameter estimations and based on which a decision is taken. Another approach that depends only on in-field measurements tracks the history of estimated parameters and based on preset thresholds, fault is detected. In MLT, there is a dependence on either real data and/or model to decide on faults. The merits of all methods are compared in Table 7 (adopted from [35]).

Table 7 Merits and demerits of the different approaches of fault detection

sl. no.	Approach	Advantages	Disadvantages
1	Model based difference measurement	<ul style="list-style-type: none"> <li>• Use of real time PV modeling reduces environmental impact</li> <li>• Accurate fault detection</li> </ul>	<ul style="list-style-type: none"> <li>• Dependency to parameter estimation technique used to define the PV model</li> <li>• Numerous additional component requirement</li> <li>• Procedurally complex</li> <li>• Large detection time</li> </ul>
2	Real time difference measurement	<ul style="list-style-type: none"> <li>• Only require threshold limits from PV model for fault detection</li> <li>• Less component requirement</li> <li>• Easy implementation</li> <li>• Improved detection time</li> </ul>	<ul style="list-style-type: none"> <li>• Accuracy depends on the quality of threshold limits set</li> <li>• Noise in synthetic data may affect fault detection</li> </ul>
3	Output signal analysis	<ul style="list-style-type: none"> <li>• Accurate in detection</li> <li>• Minimal sensor requirement</li> <li>• Commercially effective and product oriented</li> </ul>	<ul style="list-style-type: none"> <li>• Presence of noise in sampling signals affects the detection capability</li> <li>• Additional software/hardware platform for feature extraction</li> </ul>
4	Machine learning techniques	<ul style="list-style-type: none"> <li>• Setting threshold limits not required</li> <li>• Rapid fault detection</li> <li>• Classification of faults possible</li> </ul>	<ul style="list-style-type: none"> <li>• Large amount of training data required</li> <li>• Faults cannot be detected universally</li> <li>• Quality of model predicted training data depends upon the accuracy of PV model</li> </ul>

One of the examples on OSA is [36] where authors try to send an electric rectangular pulse of low power injected in a panel string where the reflected back signal is used to diagnose disconnected solar panels. This technique is called time-domain reflectometry and is illustrated in Figure 23 (adopted from [36]).

One of the examples on MLT is [37] which is a simulation study for detecting LLF, HS and OC in solar panels. Authors use LSTM (long short-term memory) networks to classify errors generated from simulation. According to them, LSTM was superior as a deep learning technique as it uses samples in VI-plane without manually extracting decisive features. Compared to SVM (support vector machine), ANN (artificial neural networks) the results are quite impressive. However, faults regenerated by modelling are ideal, non-noisy. Although authors claim comparing such classifiers on noisy data but fault detection percentages are excessively high.

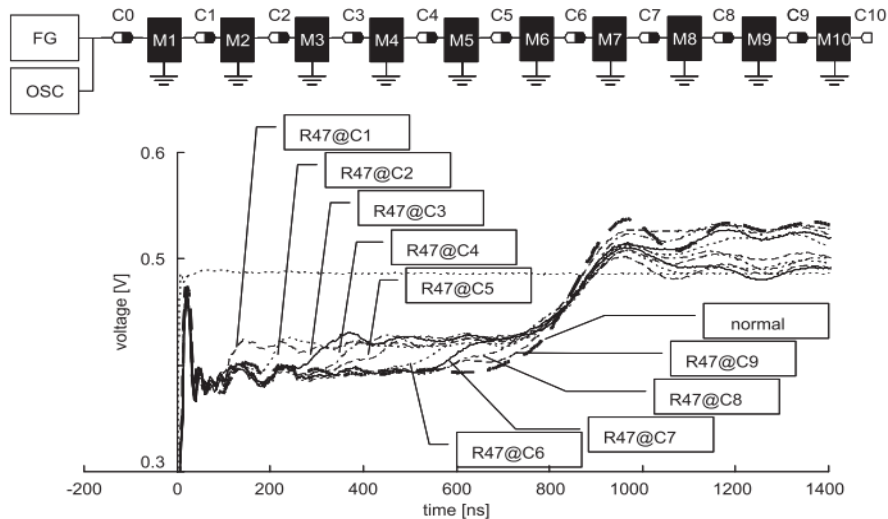


Figure 23 time domain reflectometry using function generator and an oscilloscope to check a panel string

Such work has a great potential for fault-detection of faults that result in changing IV characteristics.

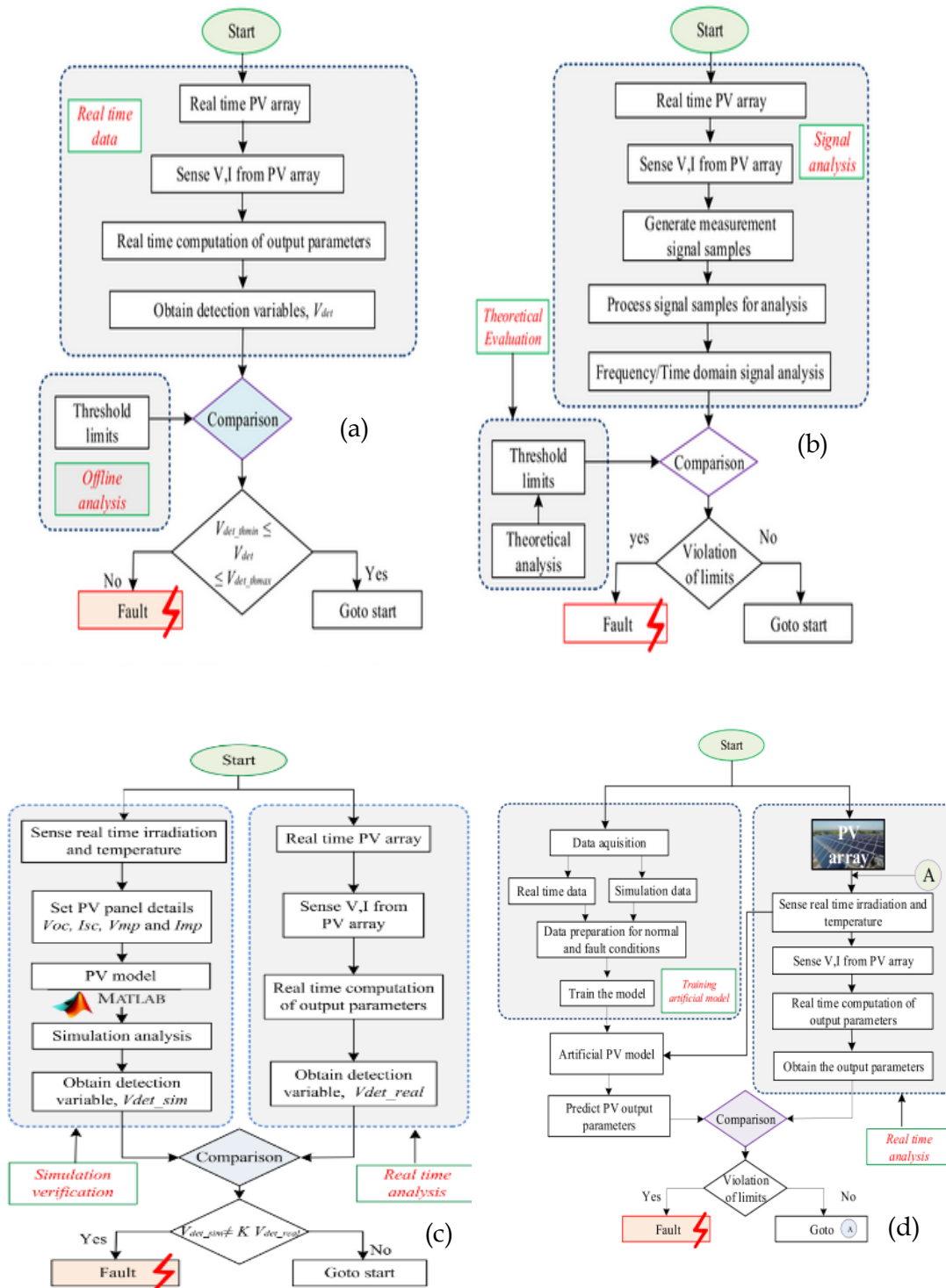


Figure 24 A brief description of RDM, OSA, MBDM and MLT

## 3.2 Hotspot and shading faults

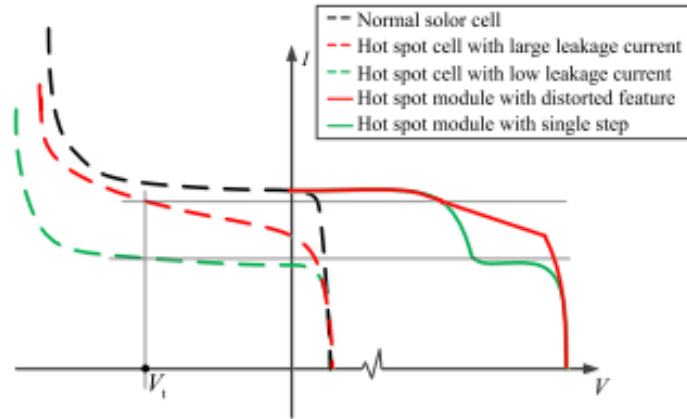
### 3.2.1 Ma's method for hotspot detection based on IV curves

In this paper [38], authors aim to locate panels where hotspot cells are found through analysis of IV characteristics. In their investigation, they analyzed 20 MW solar power station of CECEP (China Energy Conservation and Environmental Protection Group), Jiangsu, China where standard  $3 \times 20$  (cell strings  $\times$  cell count) panels are operated. At first, they gave an explanation for the hotspot phenomenon and how it happens. Consequently, three classes of hot spotted panels (based on number of cell strings within module) of IV curves arose. As the IV curve of solar panels is sampled (by SP750 characterizer device) several features are extracted from sampled IV curve and based on thresholds obtained in different operating voltages decisions are obtained to classify panels. This diagnosis method has 10% false positives when calibrated against infrared imaging (IR). The number of tested panels (positives and negatives) is unindicated.

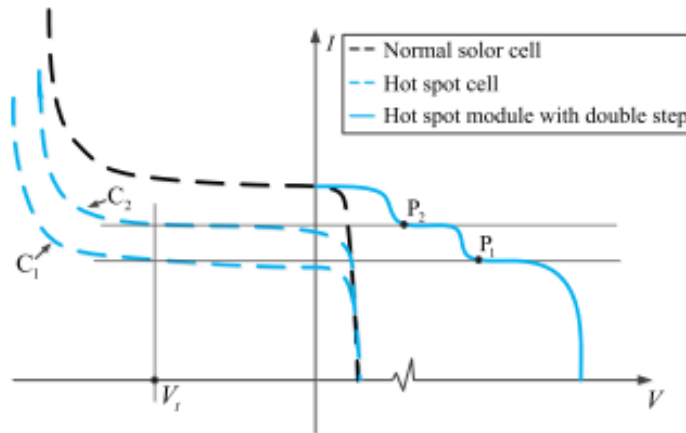
Based on single-diode model, and the assumption that each cell string has a parallel diode, the hotspot occurs as following:

- hotspot occurs as a power mismatch (of  $I_{SC}$ ) between individual cells, where they are converted to a load instead of power generation devices, so they increase in temperature.
- The IV curve of solar panel is superposition of all IV-curves of solar cells as shown in Figure 25 (adopted from [38] ) so when one of the cells has high leakage current, the summation of produced voltage produces a distorted shape of IV characteristics as shown in Figure 25 (a) in the red-line curve.
- Another form of hot spot formation still occurs even when both cells have low leakage current which results in a stepped IV curve as shown in Figure 25 (b).





(a)



(b)

Figure 25 IV characteristics of (a) leaky panel with a hotspot cell or (b) nonleaky panel with a hotspot cell

To diagnose hotspot failure based on the IV curve, authors introduced a new domain of analysis by transforming the IV curve into another computed curve (as shown in Figure 27

(adopted from [38])) and using the later to decide whether there is a hotspot with distorted feature, or a regular stepping hotspot or a normal curve.

The way features are defined is shown in Figure 26. For each voltage sample  $n$  except the last four, a line is drawn connecting the sample  $n$  to the sample  $n + 4$  in the VI plane. Distances between the 3 samples and their projections on the drawn line are calculated and called  $d_{n1}$ ,  $d_{n2}$  and  $d_{n3}$ , the maximum of these three distances is called  $d_{Nmax}$ . A mapping from the original curve of voltage and current to a new domain of voltage and  $d_{Nmax}$  is done and the difference between different category of faults is shown in Figure 27.

Based on the analysis of panel given, authors advised a defined threshold for the differentiation between different classes of faulty and unfaulty panels depending on which region of the IV characteristics the value of  $d_{Nmax}$  is evaluated. The summary of found results is shown in Table 8.

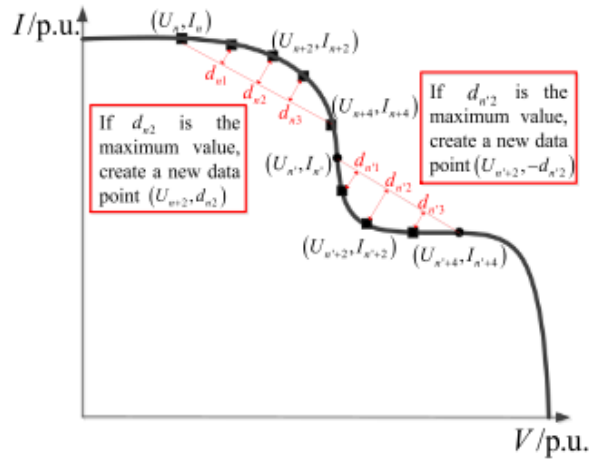


Figure 26 Distance features extracted from a stepped IV characteristics

Table 8 The characteristics of  $d_{Nmax}$  values for different voltage regions

	5 V–10 V	15 V–20 V	20 V–25 V	> 25 V
Normal module			$d_{maxN} > 0.01$	$d_{maxN} > 0.01$
Hot spot module with distorted feature		$d_{maxN} > 0.01$		$d_{maxN} > 0.01$
Hot spot module with single step		$d_{maxN} > 0.01$	$d_{maxN} < -0.02$	$d_{maxN} > 0.01$
Hot spot module with double step	$d_{maxN} < -0.02$	$d_{maxN} > 0.01$	$d_{maxN} < -0.02$	$d_{maxN} > 0.01$

The effectiveness of this method in detecting hot spot faults was compared against infrared images obtained for the same station and it had 10% false-positive rate of detecting hotspots. Authors reason that false positives can occur due to unstable soldering of panel's junction box where the solder point is heated. Hence, the diagnosis does not differentiate between hotspot to irregular shading pattern (some trees for instance), or inherent problems with cell or panel. Besides, the diagnosis method cannot localize the hotspot within the panel as infrared imaging can. It is noteworthy that authors did not justify chosen thresholds or at least ran sensitivity analysis to parameters like sample count (which was chosen to be 32 panel), also whether thresholds may affect false positive rate or not. Furthermore, the number of classes differentiating between normal, hotspot distorted, hotspot single step or hotspot double step depends mainly on number of cell strings which is specific to solar panel's commercial model, beside the limitedness of these thresholds to the chosen panel model. However, this diagnosis

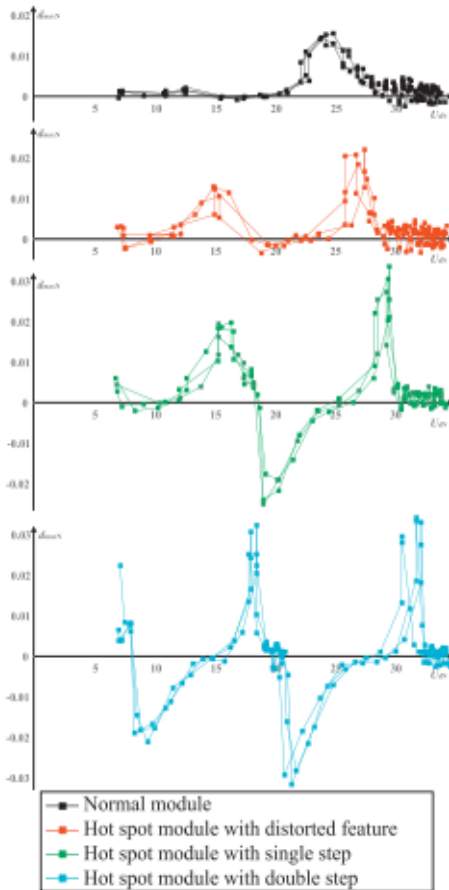


Figure 27 Looking for faults in other domain other than the IV characteristics

method can be further generalized for other panel types.

### 3.2.2 Niazi's method for hotspot detection by infrared imaging

In this paper [39], authors try to detect hotspots by analyzing thermal images of in-field panels. They try to automate the process by using Naïve-Bayes classifier[40]. A whole system view is provided in Figure 28 and it is composed of 8 panel strings, each one is composed of 22 panels and each panel is crystalline silicon and has  $3 \times 20$  cells. The maximum power output of the station is 42.24 kW. The paper mentioned several ways for detecting hot spots like

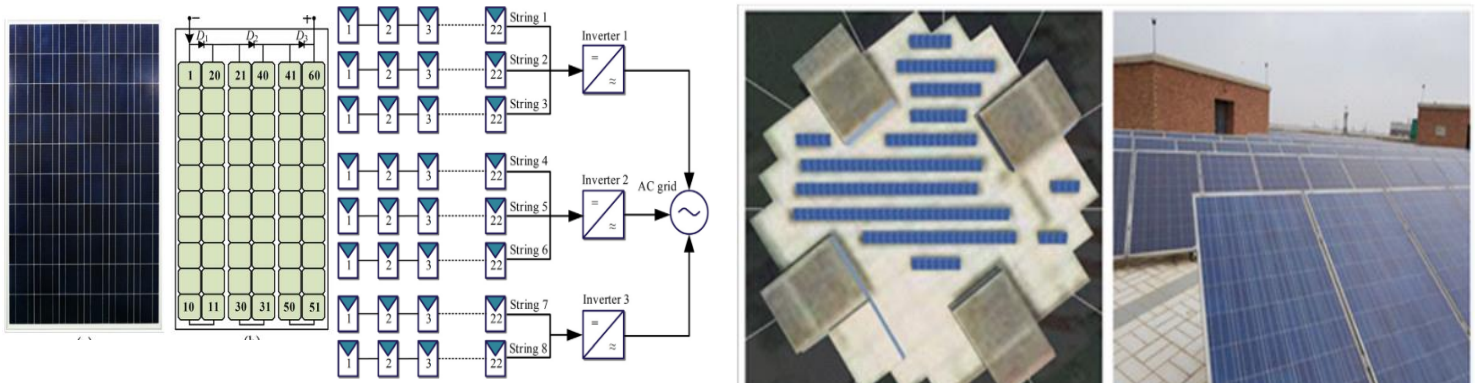


Figure 28 Installed station for the collection of thermal imaging

- IV curve analysis,
- Electroluminescence,
- Fluorescence tests,
- Resonance Ultrasonic Vibrations,
- Thermographic assessment with infrared.

In-field assessments are done by hand-held infrared camera (FLIR VUE Pro 640) positioned 1-2 meters away from each panel to image it at specific wind speed and irradiance above  $700W/m^2$ .

Authors proposed classified panels into three classes:

- Defective (D)
  - Cracked cells
  - Cells with burnt marks
  - Delaminated cells
  - Defective bypass diodes
- Non-defective with Hotspots (NDH)
  - When cell bypassing occurs
  - Temporary irregular shading
- Non-defective with No Hotspots (NDNH)

The algorithm has average 6% false-positive rate and the training dataset has the following characteristics:

1. 375 images each has the following dimensions  $640 \times 512$  with 8 bit color data for each pixel.
2. Each class has similar amount of images 130, 125, 120

The collected data has been preprocessed, then models were trained on it and preprocessing stage included

- a. RGB to grayscale
- b. Histogram equalization of produced intensity image
- c. Manual Labeling by trained professionals

Then the process of feature extraction came after so images are shifted in different angles  $0^\circ$ ,  $45^\circ$ ,  $60^\circ$  and  $90^\circ$ . Some features of images like energy, contrast, homogeneity, and correlation were recorded beside HOG (histogram of oriented gradients of image subcells) features taken from local edges which are important for images at different angles and they depend on size of sampling cells. At the end, the dimensionality of feature space is reduced by principal component analysis so both features of edges and texture are extracted.

Afterward, training stage commenced including “a non-exhaustive k-fold leave-one-out cross-validation method” [41][42] with some specifications demonstrated in [39].

The results of this classifier success are shown in Table 9 (adopted from [39]). Sensitivity means the probability of sticking with the predefined class given that the measurement was actually form that class. The specificity means the probability that the output was outside of this class given the situation the sample was outside of that class. On the other hand, the precision means the ratio of elements truly predicted to identify with a specific class to the elements truly identify with this class. The three different metrics need to be high

The method has potential for being applied on different types of panels. It includes sensitivity analysis for imaging angle on detected features. However, it is cumbersome and requires field manual assessment of all panels.

Table 9 System performance in terms of sensitivity, specificity and precision

Classes	Class 1: Defective	Class 2: NDH	Class 3: NDNH	Model accuracy
Sensitivity	0.969	0.888	0.966	0.941
Specificity	0.995	0.984	0.933	
Precision	0.992	0.965	0.872	

A summary of the analysis algorithm for finding hotspots and examples for hotspot cells are shown in Figure 29.

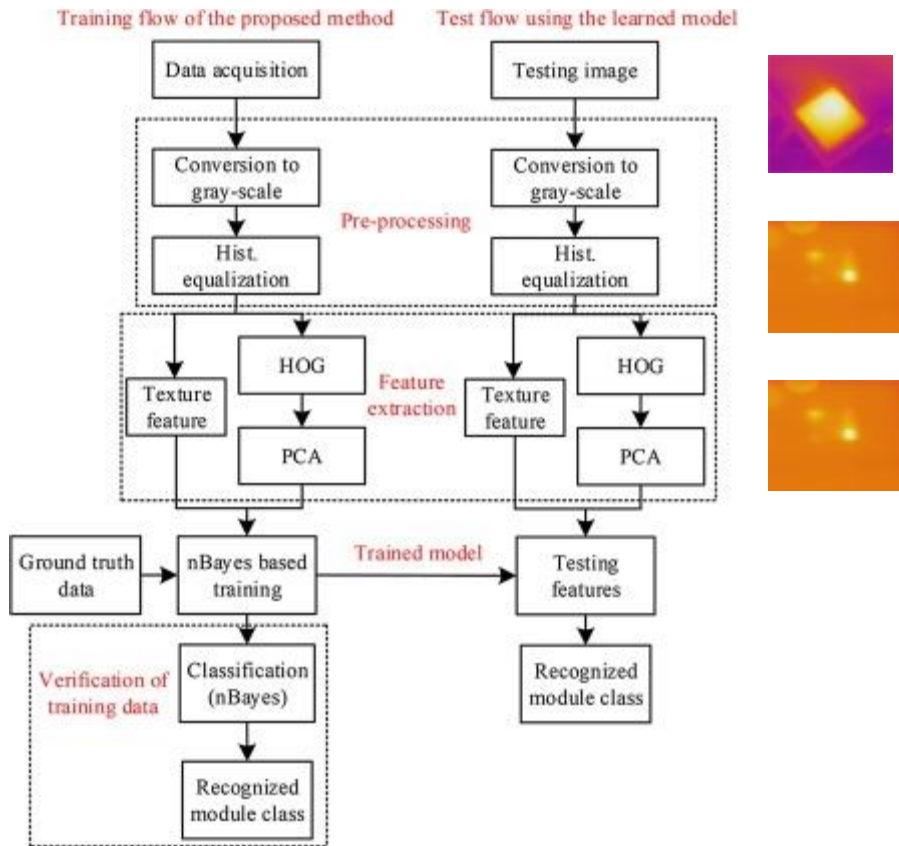


Figure 29 Summary of algorithm used to train on infrared images of solar panels and how to extract faulty panels like those showing hotspot or cracks here.

### 3.3 Modelling solar panel with arbitrary irradiance distribution and partial shading

A similar procedure is implemented in our module[43] to model an arbitrary panel with arbitrary single-diode model, SDM, parameters. The first step as shown in Figure 30, is to define an instance of a panel class with a specific dimension (10 rows and 6 columns as for used panel (see Table 18)). The target measurement was initiated afterward with a specific value for current (from 0 to 10 A). Afterward, all the SDM parameters were defined in NumPy arrays then passed as a list to be the state matrix of the measurement. The SDM parameters are the same in Table 3 except for photocurrent values which are respectively 9, 5 and 2 A for the leftmost, middle, and rightmost strings respectively.

```

1 # the target of this script is to test the simplified panel class
2 import pv_analyser as pv
3 import numpy as np
4 panel = pv.panel() # define a panel object
5 panel.rows, panel.columns = 10, 6 # dimensions of the panel
6 measurement = pv.iv_measurement(
7     current=np.linspace(0,10, 1000)
8 ) # values at which we want to calculate voltage
9 core = np.zeros((panel.rows, panel.columns))
10 rs, rp, idark, ideality, temp = core + 10e-3, core + 1e6, core+0.1e-9, core+1.1, core+25
11 ## All strings can have different irradiance levels
12 iph1 = 9 + np.zeros((panel.rows, panel.columns//3))
13 iph2 = 5 + np.zeros((panel.rows, panel.columns//3))
14 iph3 = 2 + np.zeros((panel.rows, panel.columns//3))
15 iph = np.concatenate([iph1, iph2, iph3], axis=1)
16 measurement.state_matrix = [rs, rp, iph, idark, ideality, temp]
17 panel.load_measurement(source_type='measurement', source=measurement, type='taken')
18 panel.characterize(index=0) # characterise first reading in the panel readings
19 panel.measurements[-1].plot()

```

Figure 30 Code snippet for simulating a panel with specific SDM parameter set

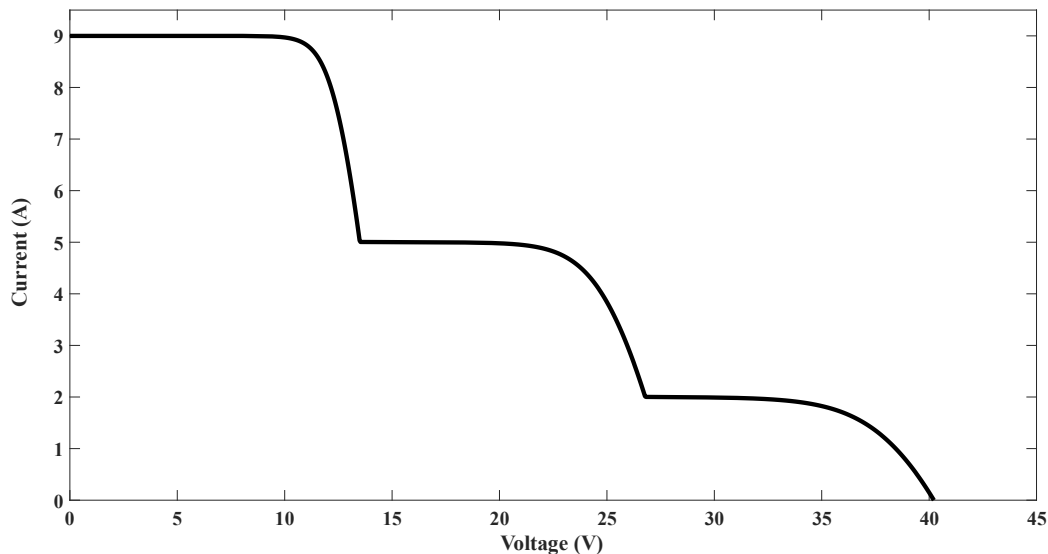


Figure 31 Resulting IV characteristics for shaded panel

To detect the various irradiance levels, present in an IV reading, one must detect first the different photocurrent levels present in the reading. Our modelling can find different irradiance levels (corresponding to current modes) by simply histogramming the output measurement. So for instance the histogram of a noisy version of Figure 31 is shown in Figure 32 and it depicts three peaks corresponding for each  $I_{ph}$ . The relative height of these peaks relates to how many cell strings are affected by being partially shaded and our analysis can locate these peaks and their number. Such procedure of finding current mode can help in estimating incident irradiance as shown in Figure 33.

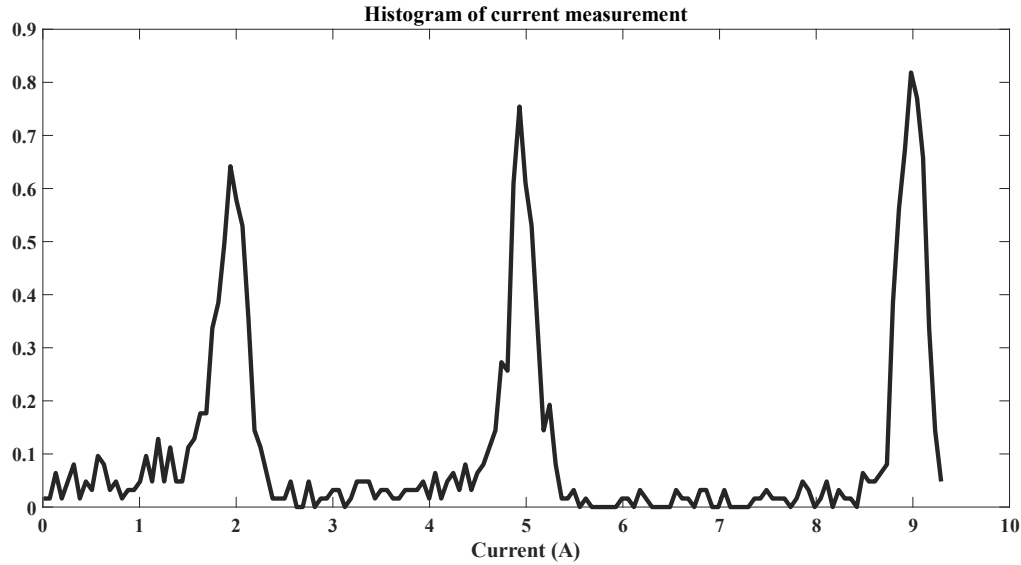


Figure 32 Histogram of a noisy shaded panel reading

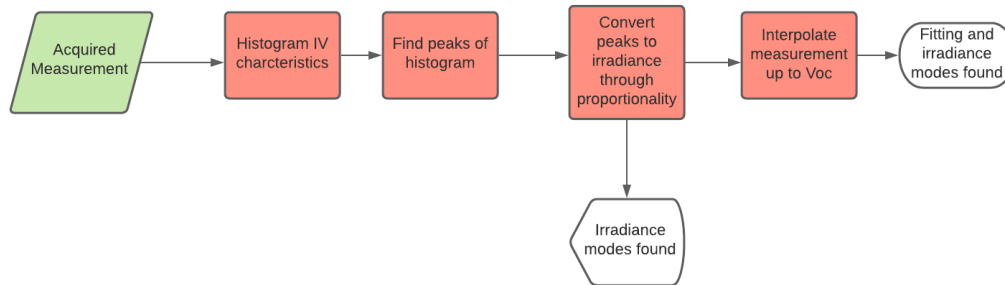


Figure 33 Procedure to estimate approximate irradiance levels from IV characteristics

## 3.4 Summary

In this chapter, an investigation on several faults that can occur to solar panels is surveyed alongside common detection methods and a comparison between them. At the beginning, a very wide review on different faults that may occur to a photovoltaic array is surveyed. Four different methodologies were reviewed in the literature: model-based difference method, MBDM, machine-learning technique MLT, real-difference measurement, RDM and output-signal analysis, OSA. The merits and demerits of either methodology is demonstrated.

Second, a fast detection algorithm based on the IV characteristics of a solar panel was used to differentiate between hotspot failures causing distorted IV curves, stepped IV curves and regular IV curves. The detection method was quite simple but specific to a specific panel type. Finally, a more accurate method of detecting panel faults depended on thermal imaging of solar panels with a handheld infrared camera. Taken photos are gone through image-processing techniques to precondition then extract useful information about the defect class of surveyed panel. The method showed high precision, sensitivity and specificity to all detection classes, but



it has been a cumbersome way of finding and classifying faults.

A combination of the aforementioned methods can be useful in detecting operational faults from IV curves, besides, we show the capability of our mathematical models to detect shading and hotspot faults based on IV characteristics. Keeping in mind, that the cost and simplicity of doing analysis based on IV curves is good compared to other cumbersome techniques that are costlier and fully manual.

# Chapter 4

## Modelling Panel in Field

To model an operating solar panel and be able to know if it works properly or not, you need to be able to have a clear understanding of the surrounding environment and how it influences solar cell behavior. In this chapter, we are going to answer both questions in an appropriate level of detail.

### 4.1 Modelling Environmental Conditions

Modelling environmental conditions is crucial for the accurate prediction of photovoltaic module performance. Not only industrial parameters are technology-specific, but also, they depend on environmental conditions. Most datasheets like [44] contain temperature coefficients for  $P_{MP}$ ,  $I_{SC}$  and  $V_{OC}$ . They are usually expressed as percentages of increasing the temperature by 1 K. Usually,  $V_{OC}$  and  $P_{MP}$  decrease as we increase the temperature in contrary to  $I_{SC}$  [44]. Besides, the positioning of solar panel also affects the solar irradiance it receives and hence the total power it produces. Several studies [45], [46] show the effect of panel tilt angle on received irradiance as well as the effect of panel direction toward south, north or any other direction on the panel performance as well.

#### 4.1.1 Estimating cell temperature

The ambient air temperature can be taken from weather stations, however the actual temperature that the panel operates at is higher than the ambient temperature, depending on the thermal properties of the solar panel. According to **SPAM** (Sandia Photovoltaic Array Modelling) model [47], [48]. The back temperature depends empirically on the total incident irradiance  $Irr_T$ , two thermal correction parameters  $a$  and  $b$ , wind speed  $WS$  and the ambient temperature  $T_a$  as shown in (13). Finally, the cell temperature depends on back temperature and the irradiance ratio of STC irradiance, total irradiance, and a temperature change  $\Delta T$  as shown in (14).

$$T_m = Irr_T \exp[a + b \times WS] + T_a \quad (13)$$

$$T_c = T_m + \frac{Irr_T}{Irr_{STC}} \Delta T \quad (14)$$

The values of thermal coefficients highly depend on the thermal coefficients of the solar panel which are fixture-dependent [48]. A list of values is found in Table 10. In an open-rack design, panel is fixed in a rack in the open air that circulates around the panel and prevents excessive heating of the panel. The back of the panel can be polymer or glass. On the other hand, close-mount fixture prevents the circulation of air when they are mounted on tilted roofs- the back can be glass or polymer

Table 10 Thermal correction factors and temperature change of a solar panel in different fixtures

Solar Panel Fixture	<i>a</i>	<i>b</i>	$\Delta T$
Open-rack glass front and back	-3.47	-0.0594	3
Open-rack glass front and polymer back	-3.56	-0.0750	3
Close-mount glass front and back	-2.98	-0.0471	1
Insulated-back glass polymer back	-2.81	-0.0455	0

#### 4.1.2 Estimating total irradiance incident on a solar panel

The incident irradiance on each solar panel is trickier (compared to temperature) to calculate and it depends on multiple factors. It is important to fix a specific spectrum when comparing different panels, even though the solar spectrum varies at every instance, location of panel on earth and its orientation, location of sun in the sky, atmospheric conditions and the urban surroundings[49], [50].

Several standard spectra are used in simulation and in industrial applications, mainly the blackbody spectrum and the AM1.0/AM1.5 spectra. The spectrum of solar irradiance can be calculated if we estimate the photon flux of an equivalent 6000 K blackbody[23] with equation (15). The photon flux  $n_{ph}$  depends on the solid angle  $\Omega$ , incident photon energy,  $E$ , which is related to its wavelength and on temperature,  $T$ .  $h$  and  $c$  are Planck's constant and speed of light respectively. However actual irradiance varies from black-body approximation in extraterrestrial region depending on the air mass,  $AM$ , which is related to the distance that sun light ray traverses until it reaches the panel and the direct perpendicular distance. Accordingly in space the air mass is 1 and it has the AM1.0 spectrum which is used for testing cells to be used in space and on earth the air mass is other than that but the AM1.5 spectrum is used in industrial testing for terrestrial applications. A depiction of solar spectra (adopted form [23]) is shown in Figure 34.

$$n_{ph} = \frac{2\Omega}{c^2 h^3} \frac{E^2}{\exp\left[\frac{E}{kT}\right] - 1} \quad (15)$$

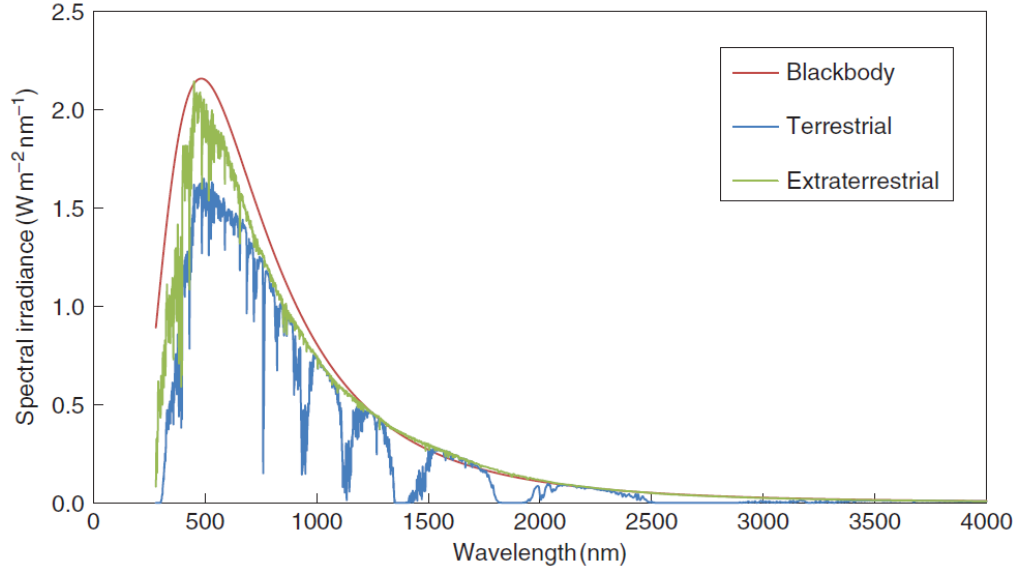


Figure 34 Solar spectra after modelling sun as a black body or after measuring actual spectra in space and on earth

The incident irradiance depends on the location of panel and the sun and the orientation of the panel. In this section we will use parameters that define these locations as depicted in Figure 35 (adopted from [46]).

#### 4.1.2.1 Positioning the panel and the sun

In a plane tangent to the location where solar panel is fixed, to specify the orientation of the panel we use the surface tilt  $\beta$  which is the angle between that plane and the solar panel and use the surface azimuth angle  $\gamma$ . The surface azimuth angle is the angle between the panel orientation and the south direction as shown in Figure 35. Likewise, the location of the sun in the sky is determined by the sun azimuth angle  $\gamma_s$  which is the angle between the sun projection on the tangent plane and the south. In addition, the sun elevation angle  $\alpha_s$  is the angle between the sun incident ray and its projection on the incident plane. Another description for the sun position depends on the zenith angle  $\theta_z$ - angle between an imaginary line normal to the location, called the zenith, and the sun location; so, we have  $\theta_z + \alpha_s = 90^\circ$ .

The procedure to estimate the total irradiance will be described here based on [51] and it aims to know  $\phi, L, \gamma$  and  $\beta$  for the panel and  $\gamma_s, \theta_z$  and  $\theta$  for the sun- which are parameters we are going to explain shortly in (16), (17), (18), (19), (20) and (21) and we express them in degrees.

First, we estimate the solar time  $t_s$  from the local time  $t_l$  by (16)

$$t_s = t_l + \frac{1}{15} (\phi_{tz} - \phi) + E \quad (16)$$

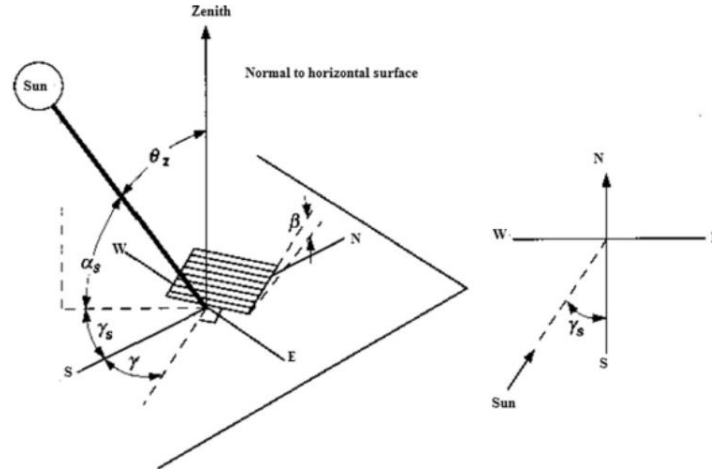


Figure 35 Location of the sun described by altitude, zenith and azimuth angles, and panel is described by tilt and azimuth angles

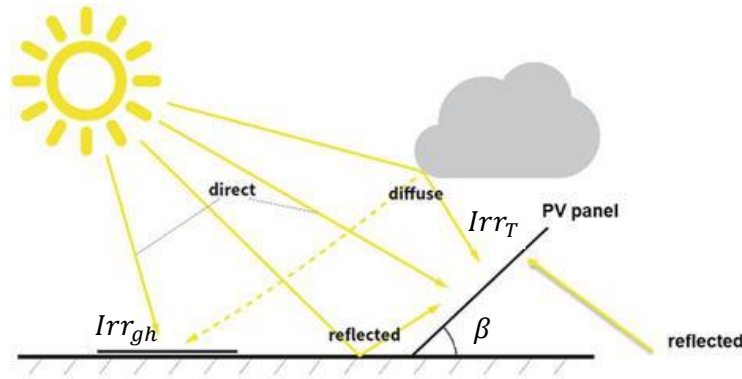


Figure 36 Different types of irradiance incident on a solar panel

The variables  $\phi_{tz}$  and  $\phi$  are the reference latitude of the time zone in degrees and the current latitude in degrees and  $E$  is a correction factor given by (17), where  $B$  depends on the Julian day number  $n$

$$\begin{cases} E = 0.0002865 + 0.0071358 \cos B - 0.1225341 \sin B - 0.0558293 \cos 2B - 0.1561998 \sin 2B \\ B = (n - 1) \times 360/365 \end{cases} \quad (17)$$

Afterward the hour angle  $\omega$  is calculated

$$\omega = 15^\circ(t_s - 12) \quad (18)$$

Declination  $\delta$ , is the angle between the plane of rotating earth with respect to the sun and it changes seasonally and is given by

$$\delta = 23.45^\circ \sin\left(\frac{360}{365}[284 + n]\right) \quad (19)$$

Accordingly, the incidence angle  $\theta$  of light ray as shown in Figure 36 is calculated by (20) where

$L$  is the longitude in degrees.

$$\begin{aligned} \cos \theta = & \sin \delta \sin L \cos \beta \\ & - \sin \delta \cos L \sin \beta \cos \gamma \\ & + \cos \delta \cos L \cos \beta \cos \omega + \cos \delta \sin L \sin \beta \cos \omega \cos \gamma + \cos \delta \sin \beta \sin \gamma \sin \omega \end{aligned} \quad (20)$$

The solar zenith angle  $\theta_z$  is calculated by setting  $\beta = 0^\circ$  in (20) and solving for  $\theta$  and subsequently, the solar azimuth is calculated by (21) where  $sgn(\omega)$  is the signum function returning  $-1$  if the number is negative and  $1$  if it is positive.

$$\gamma_s = sgn(\omega) \left| \cos^{-1} \left[ \frac{\cos \theta_z \sin L - \sin \delta}{\sin \theta_z \cos L} \right] \right| \quad (21)$$

The air mass  $AM$  is calculated empirically as in [52] to be

$$AM = 1 / [\cos \theta_z + 0.5057(96.08^\circ - \theta_z)^{-1.634}] \quad (22)$$

#### 4.1.2.2 Irradiance Models

Three types of irradiances are basic to calculate the total irradiance,  $Irr_T$ , incident on a solar panel (assuming uniform incidence and clear-sky conditions) and all are measured with assumption that  $\beta = 0^\circ$ - direct normal irradiance, **DNI** (given the symbol  $Irr_{dn}$ ), diffuse horizontal irradiance, **DHI** (given the symbol  $Irr_{dh}$ ), and the global horizontal irradiance, **GHI** (given the symbol  $Irr_{gh}$ )[51]. Such three components can be found historically in [53]–[58] for most of the world. Additionally, several mathematical models exist for estimating the three components in clear-sky conditions namely

- Perez-Ineichen model [59]–[62] : which is the most accurate/complex of the mentioned models.
- Haurwitz model [63], [64]: fails multiple times to return valid **DNI** and **DHI**.
- Simplified-Solis model [65], [66] which is a very fast model but overestimates the **DNI** and **GHI**

After knowing the positions and orientation of panel and sun by we move forward to calculate the irradiance. Different models exist for the estimation of irradiance: the Liu-Jordan model, the Klucher model and the Perez-Ineichen model [67]–[69] The most accurate and complex of them all [51] is the Perez-Ineichen model as it accounts for most phenomena related to solar irradiation.

The total irradiance can be found by (23) where  $Irr_N$  is the normal irradiance as shown in Figure 36,  $Irr_D$  is the diffuse irradiance and  $Irr_R$  is the reflected irradiance

$$Irr_T = Irr_N + Irr_D + Irr_R \quad (23)$$

The three models agree on how to calculate  $Irr_N$  and  $Irr_R$

$$\begin{cases} Irr_N = Irr_{dn} \cos \theta \\ Irr_R = Irr_{gh} \sigma \left[ \frac{1 - \cos \beta}{2} \right] \end{cases} \quad (24)$$

$\sigma$  is the albedo coefficient [70]-[72]-which is a number depending on the surroundings of the panel (shown in Table 11).

Table 11 Albedo values for different location types

Location Type	$\sigma$	Location Type	$\sigma$
Urban	0.18	Asphalt	0.12
Grass	0.20	Concrete	0.30
Fresh Grass	0.26	Aluminum	0.85
Soil	0.17	Copper	0.74
Sand	0.40	Fresh Steel	0.35
Snow	0.65	Dirty Steel	0.08
Fresh Snow	0.75	Sea	0.06

To calculate  $Irr_D$ , several parameters need to be calculated in between

$$\epsilon = \frac{\frac{Irr_{dh} + Irr_{dn}}{Irr_{dh}} + 5.535 \times 10^{-6} \theta_z^3}{1 + 5.535 \times 10^{-6} \theta_z^3} \quad (25)$$

$\epsilon$  is called the clearness and the extraterrestrial radiation  $Irr_e$  can be calculated empirically[61], [73]-[75] as

$$Irr_e = 1367 \left[ 1 + 0.033 \cos \left( \frac{360n}{365} \right) \right] W/m^2 \quad (26)$$

The brightness of the sun  $\Lambda$  is a used parameter that is calculated as

$$\Lambda = AM Irr_{dh} / Irr_e \quad (27)$$

Depending on the value of  $\epsilon$ , Perez-Ineichen model calculated the brightness coefficients as in (28) based on coefficients given in Table 12

$$\begin{cases} F_1 = \max \left\{ 0, f_{11}, f_{12} \Lambda, \frac{f_{13} \theta_z \pi}{180^\circ} \right\} \\ F_2 = f_{21} + f_{22} \Lambda + \frac{f_{23} \theta_z \pi}{180^\circ} \end{cases} \quad (28)$$

Table 12 Coefficients for Perez-Ineichen model

$\epsilon$	$f_{11}$	$f_{12}$	$f_{13}$	$f_{21}$	$f_{22}$	$f_{23}$
<b>1 – 1.056</b>	-0.008	0.588	-0.062	-0.060	0.072	-0.022
<b>1.056 – 1.230</b>	0.130	0.683	-0.151	-0.019	0.066	-0.029
<b>1.230 – 1.500</b>	0.330	0.487	-0.221	0.055	-0.064	-0.026
<b>1.500 – 1.950</b>	0.568	0.187	-0.295	0.109	-0.152	0.014
<b>1.950 – 2.800</b>	0.873	-0.392	-0.362	0.226	-0.462	0.001
<b>2.800 – 4.500</b>	1.132	-1.237	-0.412	0.288	-0.823	0.056
<b>4.500 – 6.200</b>	1.060	-1.600	-0.359	0.264	-1.127	0.131
<b>&gt; 6.200</b>	0.678	-0.327	-0.250	0.156	-1.377	0.251

Once the brightness coefficients are found additional two intermediate parameters are found

$$\begin{cases} a = \max\{0, \cos \theta\} \\ b = \max\{\cos 85^\circ, \cos \theta_z\} \end{cases} \quad (29)$$

Then finally we can find the diffuse irradiance  $Irr_D$  as in

$$Irr_D = Irr_{ah} \left[ (1 - F_1) \left( \frac{1 + \cos \beta}{2} \right) + F_1 \frac{a}{b} + F_2 \sin \beta \right] \quad (30)$$

Then we finally use substitute (30) and (24) in (23) to find the total irradiance incident on a solar panel.

## 4.2 SDM Explained

### 4.2.1 Why SDM and its limitations?

Several phenomena cannot be modelled with **SDM**. For instance, many solar cells exhibit solar alternating-current output. In normal direct-current operation, electrons are separated toward the n-type region and holes are separated to the p-type region after photogeneration, however, when illumination periodically shines on the surface of a solar cell an AC current is produced that surpasses the original DC current which is useful when we consider solar cell as a broadband photodetector (an application totally different to power generation)[76].

Modelling solar cell at different irradiance, temperature is a difficult task, so different variations in solar cell models exist to account for environmental conditions including number of resistors used (finite or infinite), number of diodes and dependence on environmental conditions [77]. An example of these variations is the use of single/double/triple diode models, **SDM**, **DDM** and **TDM** namely[78] as depicted in Figure 37.

It was noted in [79], that the photogenerated current in a solar cell, was not a result of a single diode connected between the two main layers of the semiconductor, rather than multiple diodes connected in parallel whose effect is a great energy dissipation affecting the conversion efficiency of the solar cell. As a solution, it was proposed in [79] to use **DDM** on the expense of having larger number of parameters for mathematical modelling so instead of having single  $I_{dark}$ , we have  $I_{s1}, I_{s2}, n_1$  and  $n_2$  for both diodes.



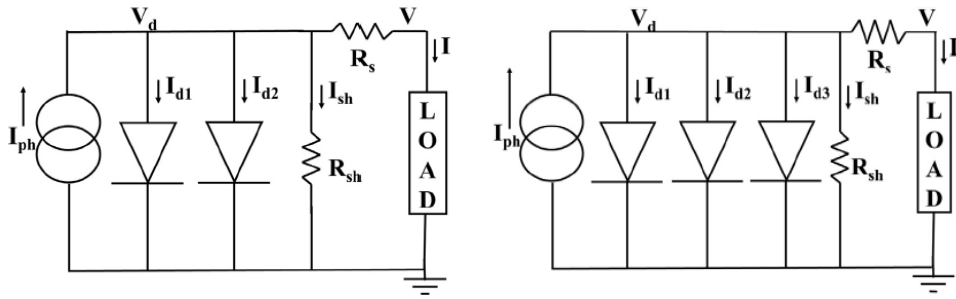


Figure 37 DDM and TDM for a solar cell

In **SDM**, the value of ideality factor was  $1 \leq n \leq 2$  to combine the effects of both diffusion and recombination together and it was chosen to fit experimental data in most situations [78]. If  $n$  is 1, diffusion and recombination will occur at the bulk of cell and the quasi-neutral regions of the emitter. If  $n$  is 2, then recombination is occurring at the space-charge region mainly. As a result, the value of  $n$  in between implies the existence of both mechanisms simultaneously.

For **DDM**, two values for idealities are proposed namely  $n_1 = 1$  and  $n_2 = 2$  to account for both mechanisms and accordingly the value of saturation currents of both diodes specify the dominance of either mechanism. However, for industrial panels,  $1 \leq n_1 \leq 1.5$  and  $2 \leq n_2 \leq 5$  for proper modelling of solar cell [78]. The values of  $I_{s2}$  is larger 3 – 7 orders of magnitude that  $I_{s1}$ [80].

For **TDM**, an additional diode is added so  $n_1 = 1, n_2 = 2$  and  $2 \leq n_3 \leq 5$ , the purpose of the added parameter is to account for the recombination current at defect regions and edges. The value of  $n_3$  increases as of increasing defect density especially increasing localized defects due to laser-cutting and scratching [81].

A comparison between **SDM** and **DDM** based on [77] is found in Table 13 and it shows that the main advantage for **DDM** is accuracy in shadow conditions and in the vicinity of open-circuit point [80], [82]. However, the DDM is not applicable for most solar cell technologies and takes great time to implement and to extract model parameters. It is apparent that **SDM** is sufficient for most applications and technologies with acceptable error.

Table 13 Comparison between SDM and DDM in different aspects

	<b>SDM</b>	<b>DDM</b>
<b>Accurate in the normal condition</b>	Yes	Yes
<b>Accurate in the shadow condition</b>	No	Yes
<b>High computational effort</b>	No	Yes
<b>More applicable and used for most PV types</b>	Yes	No
<b>Sufficiently describes the PV characteristics</b>	Yes	Yes
<b>Depending on the cell temperature</b>	Yes	Yes
<b>Depending on the irradiance</b>	Yes	Yes
<b>Easy to implement</b>	Yes	No
<b>Applicable for both indoor and outdoor conditions</b>	Yes	Yes

## 4.2.2 Modelling from cell up to array

In this thesis, we will use the following terminology for describing a photovoltaic panel. The physical shape of the panel is same as in Figure 6, however, internally, it is connected as in Figure 38. So, the panel is composed of  $r$  rows and  $c$  columns and has  $n$  diodes in its junction box. The number of diodes divides panel columns evenly, so each group of columns form a cell string where all cells are connected in series. The way these cells are connected in series is a zigzag shape and in total, the panel is regarded as a series connection of cell strings and each cell string that has  $m$  cells (i.e.,  $mn = rc$ ) is bypassed with a bypass diode.

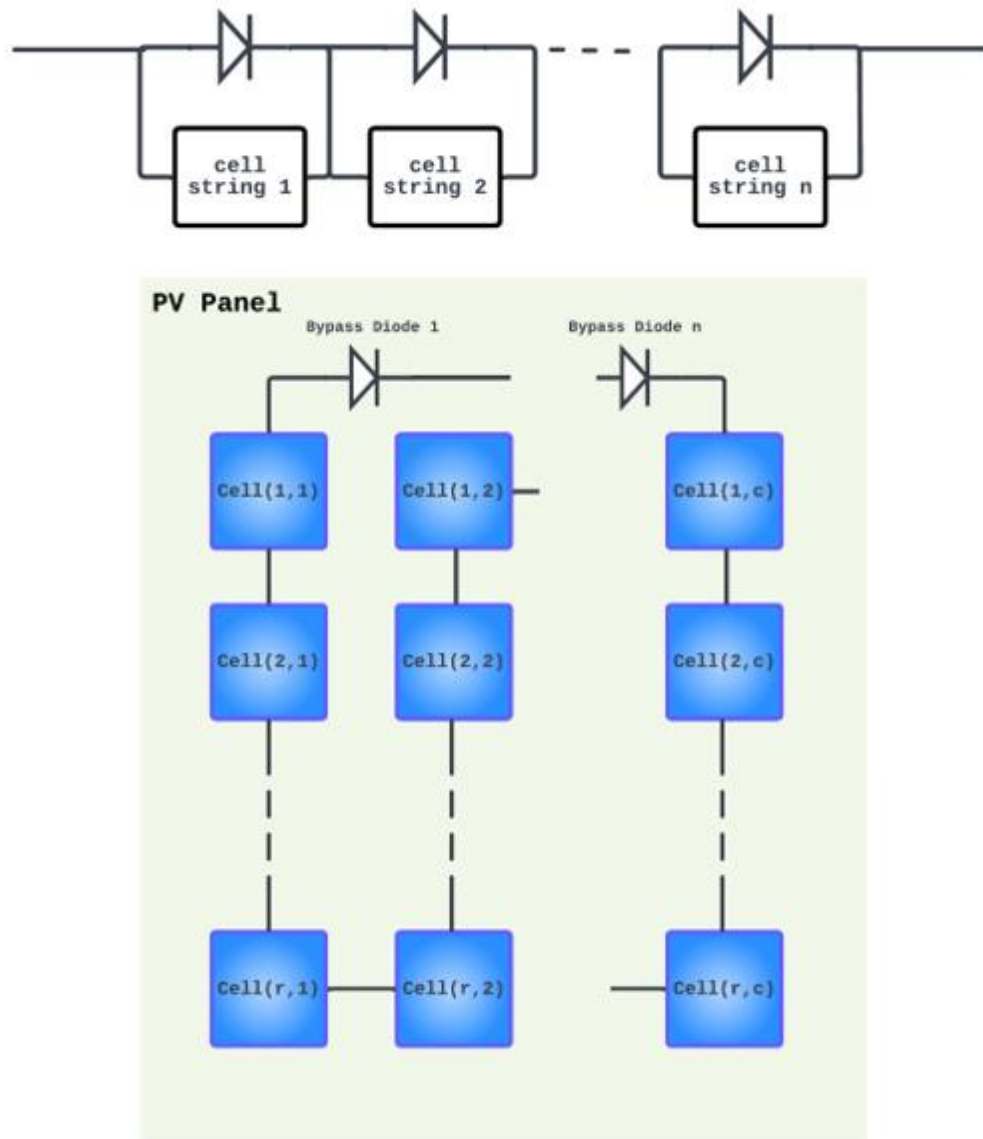


Figure 38 Internal connection of a photovoltaic panel as a series connection of cell strings and cells are positioned in physical panel

To get the IV characteristics of the whole panel one must find the IV of each cell string at the beginning by solving (11) at different currents and after that we can use Kirchoff voltage law to find the IV characteristics of the cell string number  $i$  as in (31)

$$V_{string,i} = \sum_{k=1}^m V_{cell,k} \text{ and } 1 \leq i \leq m \quad (31)$$

It is noted that we do the sum over the voltage, but for current, the cell with lowest  $I_{SC}$  fixes the  $I_{SC}$  of the whole cell string the same to make sure that the same current passes through the whole string.

#### 4.2.2.1 Cell string with different irradiance levels

Assume we have three cells in series, each with SDM parameters demonstrated in Table 3. We will define a simple cell string object as shown in Figure 39 (with aid of our analysis module [43]) and pass the different SDM values for each cell within the cell string.

```

2 import pv_analyser as pv
3 import numpy as np
4
5 core = np.zeros((3,))
6 rs = core + 10e-3
7 rp = core + 1e6
8 iph = np.array([9, 9, 9_])
9 idark = 0.1e-9 + core
10 ideality = 1.1 + core
11 temperature = 25 + core
12 cell_string = pv.cell_string(
13     rs=rs,
14     rp=rp,
15     idark=idark,
16     iph=iph,
17     ideality=ideality,
18     temp=temperature
19 )
20 current = np.linspace(0, 9.1, 1000)
21 cell_string.characterize(current=current)
22 cell_string.measurement.plot()

```

Figure 39 Code snippet for defining a cell string

We show here three different plots when all of cells have 9-A photocurrent, or 5-A photocurrent or when only one of them has 5-A photocurrent. The three curves are demonstrated at Figure 40. It is noticeable that the lowest short-circuit current is the current of the whole string. A summary of important features of the three curves is found in Table 14. Also, the fill factor increases significantly when there is great mismatch between the photocurrent of single cells within a cell string a situation which can occur when all substrings of the solar panel has two different levels of irradiance that are far apart.

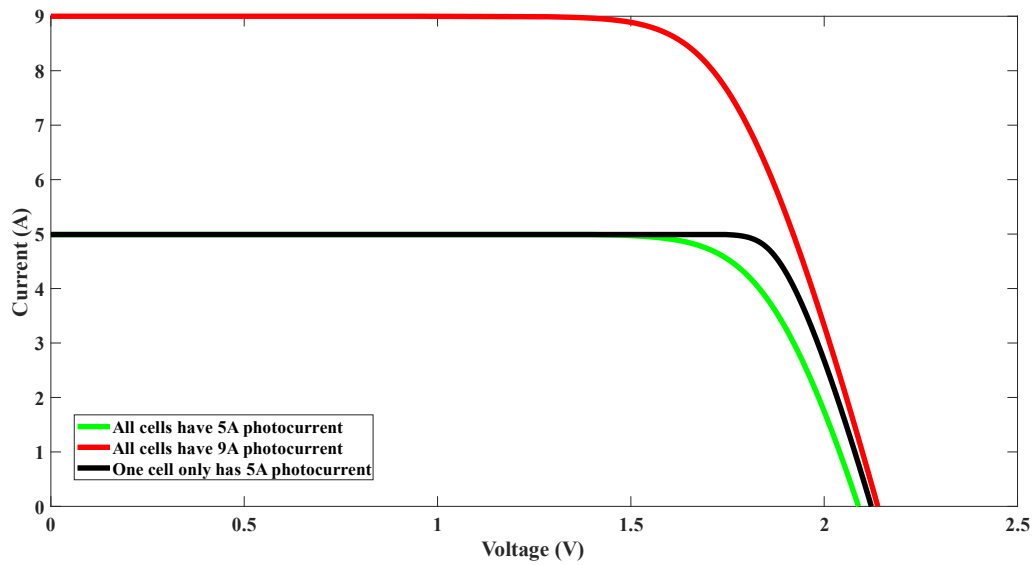


Figure 40 IV characteristics for a cell string of three irradiance distributions

Table 14 Comparison between strings of different photocurrents

	All cells have 9A $I_{ph}$	All cells have 5A $I_{ph}$	One cell has 5A $I_{ph}$
$I_{SC}$ (A)	9	5	5
$V_{OC}$ (V)	2.139	2.089	2.122
$FF$	0.724	0.771	0.842
$P_{MP}$ (W)	13.928	8.038	8.919

#### 4.2.2.2 Finding the IV characteristics of a panel

In [83], authors tried to speed up finding the IV characteristics of an array of solar panels. Such array is composed of parallelly-connected panel strings, where each string is serially connected panels (or modules in terms of the paper) with additional blocking diode. Here, it is assumed that each panel has different short-circuit current and no internal bypass diodes,  $I_{SC}$ . Finding IV characteristics this way speeds up modelling huge non-linear network of solar cells at each time of model characterization. It is shown as well, what happens when each panel has different irradiance level as an effect over the IV characteristics.

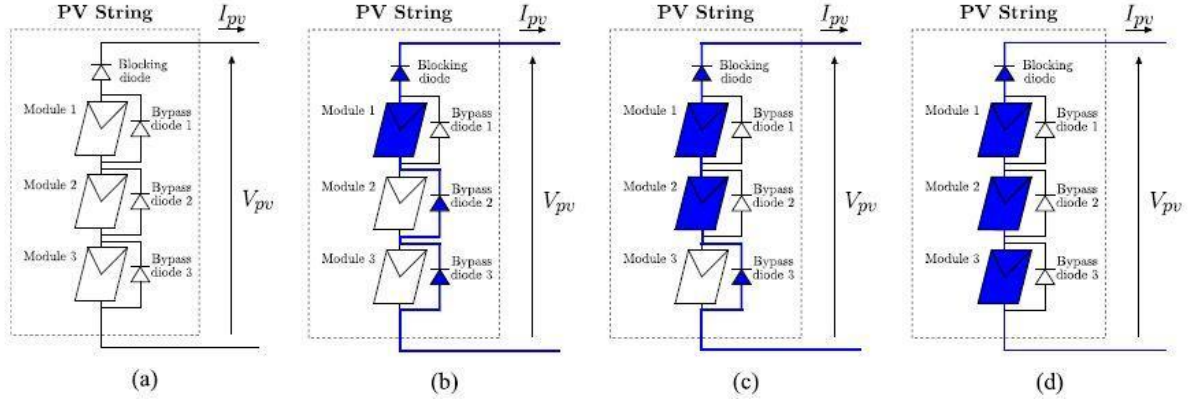


Figure 41 Active current path when (a) all panels are shaded, (b) when only one panel produces current and the two other panels are bypassed, (c) when only one panel is bypassed for being shaded and (d) when all panels are active.

In Figure 41 (adopted from [83]), each module is governed by an irradiance level corresponding to a specific current flow. As we scan the IV characteristics, at each current level, modules with higher or equal  $I_{SC}$  are activated, so current passes through them, while other remaining modules are bypassed by diodes. So, in Figure 41 (a), it represents the situation when no current passes through the modules, (b) when at specific current level only one panel has an  $I_{SC}$  higher or equal, so this is the only panel capable of producing this level of current, so other two panels are bypassed as if they are not they will be treated as loads. The same applies for (c) and (d) but with different number of active panels.

Authors in [83], provided the IV characteristics of each module (in Figure 41) on its own and then gave a conclusion on the overall IV. Figure 42 (adopted from [83]), shows the IV of three different panels subject to  $1000 W/m^2$ ,  $600 W/m^2$  and  $200 W/m^2$ . Each irradiance level corresponds to a different  $I_{SC}$ , so if we imagine the current axis to run from 0 to  $I_{SC1}$ , so for  $0 \leq I \leq I_{SC3}$ , the three panels are active as in Figure 41 (d), and their voltage drops are added resulting in (32), where  $i$  is the number of module in the  $n$  modules.

$$V_{OC} = \sum_{i=1}^n V_{OC,i} \quad (32)$$

Further, for  $I_{SC3} \leq I \leq I_{SC2}$ , only panels with  $1000 W/m^2$  and  $600 W/m^2$  irradiance are active beside an operating bypass diode. Likewise, for  $I_{SC2} \leq I \leq I_{SC1}$ , only panel with  $1000 W/m^2$  irradiance is active beside two operating bypass diodes. So we can tell that, for all connected modules, (33) holds

$$I_{SC} = I_{SC,1} \quad (33)$$

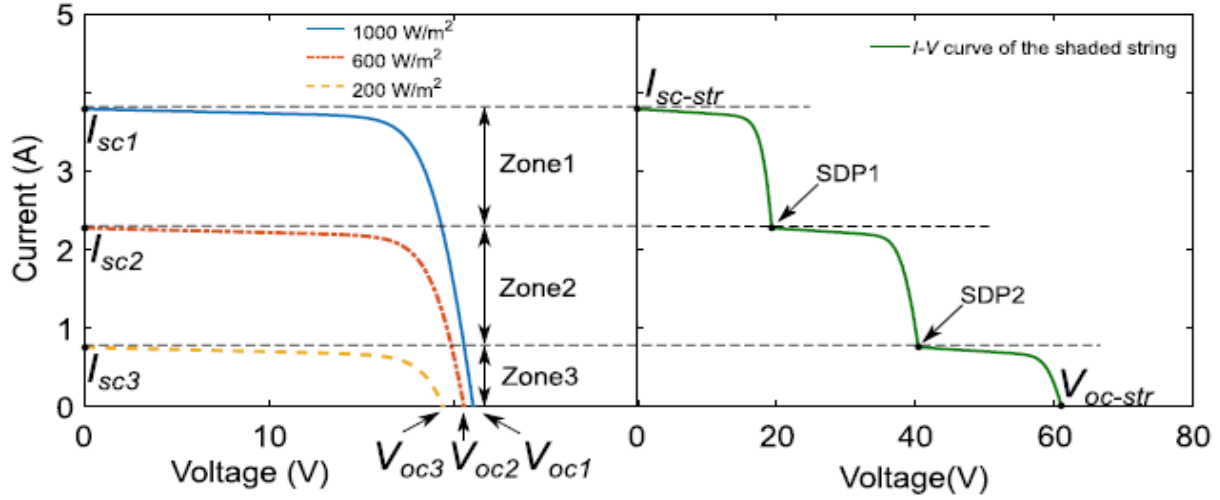


Figure 42 The IV characteristics of three different panels in Figure 41, and their resultant IV when connected together

Based on [83], we can find the IV characteristics where  $V$  is a function of by noticing in which zone we are calculating the voltage. First, we sort the short-circuit currents of all modules so  $I_{sc,1} > I_{sc,2} > \dots > I_{sc,n}$  and each zone  $z$  has current  $I_{sc,z+1} < I \leq I_{sc,z}$  then the voltage for current in zone  $z$  is given by

$$V(I) = \left[ \sum_{i=1}^z V_i(I) \right] + \left[ \sum_{i=z+1}^n V_{diode}(I) \right] + V_{blocking}(I) \quad (34)$$

In our modelling approach we replace each panel in the model proposed in [83], by a cell string, because each cell string has a single bypass diode, and we will make sure that it has a different  $I_{sc}$  by perturbing similar  $I_{sc}$  values with an acceptable error. We can also assume that all bypass diodes are identical and can be modelled with a simple diode equation. Furthermore, we can neglect the blocking diode component in (34) as within a panel we do not have such a diode so and based on (7), (34) can be edited to be (for each zone  $z$ )

$$V(I) = \left[ \sum_{i=1}^z V_i(I) \right] + (n - z) \frac{\alpha kT}{e} \ln \left( \frac{I}{I_s} + 1 \right) \quad (35)$$

such that  $\alpha$  and  $I_s$  are the ideality and reverse saturation current for the bypass diode.

In normal conditions, where uniform irradiance is incident over the panel, we can use a good approximation of the IV characteristics based on [84] where we can modify (11) to be

$$I = I_{ph} - I_0 \left[ \exp \left[ \frac{e(V + IR_S)}{nN_s kT} \right] - 1 \right] - \frac{V + IR_S}{R_p} \quad (36)$$

here,  $R_S$  is the series resistance of the panel as a whole,  $N_S$  is number of cells in series in a panel. The ratio  $R_{S_{panel}}/R_{S_{cell}} = R_{P_{panel}}/R_{P_{cell}} = N_S$  is shown to be true in most situations [85]. However, the relation of the diode reverse saturation current between cell and panel is ambiguous. But based on experimentation, diode reverse saturation current of panel model is larger.

## 4.3 SDM parameter extraction

The circuit parameters of the solar cell:  $R_S, R_P, I_{ph}, I_{dark}$  and  $n$  are not provided for actual solar panel. Rather than that, they can only be extracted from IV measurements. Finding circuit parameters is crucial for directly evaluating the panel performance. The key challenge is the extreme nonlinearity given by the SDM model in (36).

The parameter extraction methods can be divided into three families [86]:

1. **Family 1:** manipulating the SDM model mathematically to reach a feasible set of solvable equations which are non-iterative methods.
2. **Family 2:** Exploitation of numerical approaches to calculate the parameters of SDM, called iterative algorithms.
3. **Family 3:** Metaheuristic approaches depending on stochastic optimization techniques like genetic algorithms, particle swarm, simulated annealing, ant colony and other more.

We will focus on families 1 and 2, as they are simpler in implementation and as stochastic methods in family 3 needs a lot of parameters to fit within the implementation of the algorithms itself.

### 4.3.1 Family 1 approaches

Three important points in the IV curve are used to do parameter extraction: the SC point, OC point and the maximum power point. If we substitute in (36) with  $I = 0$  to derive an equation at OC (38), or when we substitute with  $V = 0$  to find an equation at the SC point (39), when we substitute at the maximum power point to conclude (40), or when  $\frac{dI}{dV} = 0$  to find the point of maximum power(41) we reach the following set of equations [87]:

Given that

$$\begin{cases} V_{th} = \frac{kT}{e} \\ A = \exp\left(\frac{V_{MP} + I_{MP}R_S}{nN_S V_{th}}\right) \end{cases} \quad (37)$$

where  $V_{th}$  is called the thermal voltage, and  $A$  is an arbitrary variable to simplify the form of the equations given below

$$I_{ph} - I_0 \left[ \exp\left(\frac{V_{OC}}{nN_S V_{th}}\right) - 1 \right] - \frac{V_{OC}}{R_P} = 0 \quad (38)$$

$$I_{SC} - I_{ph} + I_0 \left[ \exp\left(\frac{I_{SC}R_S}{nN_S V_{th}}\right) - 1 \right] + \frac{I_{SC}R_S}{R_P} = 0 \quad (39)$$

$$I_{MP} - I_{ph} + I_0[A - 1] + \frac{V_{MP} + I_{MP}R_S}{R_P} = 0 \quad (40)$$

$$\frac{I_{MP}}{V_{MP}} - \frac{nN_S V_{th} + I_0 R_P A}{nN_S V_{th}(R_S + R_P) + I_0 R_P R_S A} = 0 \quad (41)$$

An additional equation that is also taken in consideration [88] derived from derivative of power substituting the power derivative into (41)

$$V_{MP} n N_S V_{th} (I_0 R_P + I_{ph} R_P - 2V_{MP}) + I_0 R_P A [P_{MP} R_S - V_{MP} (n N_S V_{th} + V_{MP})] = 0 \quad (42)$$

The different noniterative approaches depend on simplifying (38),(39),(40),(41), and (42) to get some formulas that are easier to manipulate and reach best solutions, otherwise the solution of the system of these nonlinear equations would be very complex, although it was suggested in [88] to do so with good initial guesses.

In [85], seventeen non-iterative methods for finding the SDM circuit parameters from industrial parameters are reviewed and their performance in terms of accuracy, robustness and complexit, were comparatively assessed on the NREL dataset [89]. The NREL dataset contains 1025665 different IV measurements for 22 different PV panels that are monocrystalline/multi-crystalline/amorphous silicon, heterojunction-with-intrinsic-thin-layer, CIGS and CdTe thin film panels. At all these measurements, accompanying environmental conditions.

In

Table 15 (adopted from [85]), a comparison between the different non-iterative methods was done. For accuracy, two measures were used for error, the root-mean-square error, **RMSE** (43), and the normalized version of the same error, **NRMSE** (44) [86]. The robustness of algorithms were denoted by their capability to give meaningful physical parameters so all parameter values must be positive reals, and when the algorithm executes smoothly without any errors. According to the table, Cannizzaro's method [90] has the lowest maximum NRMSE, while for robustness Saloux's method[91] is the most robust. So we will investigate both methods shortly.

$$RMSE = \sqrt{\frac{1}{N} \sum_{i=1}^N (I_{measured} - I_{calculated})^2} \quad (43)$$

$$NRMSE = \frac{RMSE}{\sqrt{\frac{1}{N} \sum_{i=1}^N I_{measured}^2}} \quad (44)$$



Table 15 Performance of seventeen different methods for parameter extraction on the NREL dataset

Method	Accuracy (RMSE)				Robustness		Complexity	
	Absolute (A)		Normalized (%)		Irregularities	Failures	Execution Time (s)	
	Mean	Max	Mean	Max				
Phang	0.016	4.210	0.38	69.4	387,440	9952	13.1	1.3
* Sera	0.026	2.471	0.74	49.6	794,670	52	1.3	1.3
Saleem	0.018	2.255	0.47	45.3	22,810	24	10.7	2.1
* Saloux	0.029	1.271	0.79	25.5	2	0	1.2	1.2
* Accarino	0.034	0.880	1.09	17.7	2804	25	1.5	1.5
Khan	0.043	4.201	1.19	69.3	511,210	8242	13.2	1.4
Cubas1	0.011	2.445	0.36	49.1	529,530	2445	8.2	1.1
* Cubas2	0.026	2.433	0.64	48.8	626,150	53	1.3	1.3
* Cubas3	0.024	0.430	0.83	13.0	1878	224	2.0	2.0
* Bai	0.032	2.544	0.93	51.1	6390	37	1.7	1.7
* Aldwane	0.021	1.032	0.59	20.7	416,650	29	1.3	1.3
* Cannizzaro	0.013	0.431	0.39	11.3	100	28	2.1	2.1
Toledo	0.007	1.119	0.20	97.7	451,220	392	14.0	2.5
Louazani	0.122	1.449	3.43	27.0	64,194	30,612	12.5	1.1
* Batzelis	0.028	0.932	0.87	18.7	412	0	1.5	1.5
* Hejri	0.231	6.761	7.21	129.4	794,670	14,057	5.4	5.4
* Senturk	0.034	1.285	1.09	25.8	27,847	0	1.2	1.2

The asterisk "\*" denotes methods that rely only on datasheet information. Bold font indicates the lowest value in the respective column.

#### 4.3.1.1 Saloux's method

The method relaxes equations (38), (39) and (41) by substituting  $R_S = 0$  and  $R_P = \infty$  so

$$I_{ph} = I_{SC}$$

(45)

$$n = \frac{V_{MP} - V_{OC}}{N_S V_{th} \left( \ln \left( 1 - \frac{I_{MP}}{I_{SC}} \right) \right)}$$

(46)

$$I_0 = \frac{I_{SC}}{\exp \left( \frac{V_{OC}}{n N_S V_{th}} \right) - 1}$$

(47)

The reasoning in this assumption is that series resistance is almost a negligible value when a panel is perfectly connected, and the leakage current is almost zero.

#### 4.3.1.2 Cannizzaro's method

The basic assumption is that the SDM can be reduced to involve four parameters only based on which resistor is more dominant in its effect whether it is  $R_S$  or  $R_P$ . To do so, some intermediate parameters are estimated as in (48)

$$\begin{cases} \gamma_v = I_{MP}/I_{SC} \\ \gamma_i = V_{MP}/V_{SC} \\ r = \frac{\gamma_i(1 - \gamma_v)}{\gamma_v(1 - \gamma_i)} \\ SPR = \frac{1 - \gamma_i}{\exp(-r)} \end{cases} \quad (48)$$

The parameter  $SPR$  is the series-to-parallel ratio and determines which resistance we will consider in our four-parameter model. So, if  $SPR \geq 1$

Then

$$R_S = \frac{V_{OC} \gamma_v (1 - \gamma_i) \ln(1 - \gamma_i) + (1 - \gamma_v)}{I_{SC} \gamma_i (1 - \gamma_i) \ln(1 - \gamma_i) + \gamma_i}, \quad R_P = \infty \quad (49)$$

otherwise,

$$R_S = 0, R_P = \frac{V_{OC} \lambda_2 w + \lambda_1}{I_{SC} w + \lambda_1} \quad (50)$$

given that

$$\begin{cases} \lambda_1 = \frac{1 - \gamma_v}{1 - \gamma_i} \frac{2\gamma_i - 1}{\gamma_i + \gamma_v - 1} \\ \lambda_2 = \frac{\gamma_v}{1 - \gamma_i} \\ w = W_{-1}\{SPR \lambda_1 \exp(-\lambda_1)\} \end{cases} \quad (51)$$

and the  $W_{-1}\{\}$  is the lower branch of the Lambert W function that can be approximated by

$$W_{-1}\{x\} = -1 - \sigma - 2/M_1 \left( 1 - \frac{1}{1 + \frac{M_1 \sqrt{\sigma/2}}{1 + M_2 \sigma \exp(M_3 \sqrt{\sigma})}} \right) \quad (52)$$

with  $\sigma = -1 - \ln(-x)$ ,  $M_1 = 0.3361$ ,  $M_2 = -0.0042$  and  $M_3 = -0.0201$

Afterward, other parameters can be found by (53), (54), and (55)

$$n = \frac{1}{N_S V_{th}} \left[ \frac{V_{MP} - V_{OC} + I_{MP} R_S}{\ln \left( \frac{(I_{SC} - I_{MP}) \left( 1 + \frac{R_S}{R_P} \right) - \frac{V_{MP}}{R_P}}{I_{SC} \left( 1 + \frac{R_S}{R_P} \right) - \frac{V_{OC}}{R_P}} \right)} \right] \quad (53)$$

$$I_{ph} = I_{SC} \left( 1 + \frac{R_S}{R_P} \right) \quad (54)$$

$$I_0 = \left( I_{SC} - \frac{V_{OC}}{R_P} \right) \exp \left( -\frac{V_{OC}}{n N_S V_{th}} \right) \quad (55)$$

### 4.3.2 Family 2 approaches

Family 2 approaches are iterative in nature and they use numerical techniques to set of regular roots of (38),(39), (40), (41) and (42).

The choice of either family 1 approach or family 2 approach is dependent on the type of IV measurement. If the measurement is taken from datasheet, then taken curves will be less noisy and the analytical solutions in family 1 will be sufficient to estimate parameters. However, when measurements are noisy and taken experimentally from a panel working in field then numerical approaches will be sufficient [86].

#### 4.3.2.1 Stornelli's method

In [92], the SDM parameters are estimated in two stages:

1. An intermediate model where  $R_p = \infty$  is used to estimate  $n, R_S, I_{dark}$ , and  $I_{ph}$ .
2. Results from the intermediate model are fed into another step of finding the  $R_p$  value.

The rationale behind this is a simple observation, that the change of  $R_S$  affects the slope at the OC point, and changing the  $R_p$  changes the slope at the SC point, so what will happen if we separate both effects?

If we take the limit of  $R_p \rightarrow \infty$  for expression in (38) we have

$$I_{ph} = I_{dark} \left[ \exp\left(\frac{V_{OC}}{nN_S V_{th}}\right) - 1 \right] \quad (56)$$

and if we took the limit  $R_p \rightarrow \infty$  for (39), then we substituted with result in (56) we find that

$$I_0 = \frac{I_{SC}}{\left[ \exp\left(\frac{V_{OC}}{nN_S V_{th}}\right) - \exp\left(\frac{R_S I_{SC}}{nN_S V_{th}}\right) \right]} \quad (57)$$

then, if we also take the limit  $R_p \rightarrow \infty$  for (41), substitute with (56) and (57) then rearrange to have  $R_S$  as left hand side we reach

$$R_S = \frac{V_{OC}}{I_{MP}} + \frac{nN_S V_{th}}{I_{MP}} \ln\left(\frac{nN_S V_{th}}{nN_S V_{th} + V_{MP}}\right) - \frac{V_{MP}}{I_{MP}} \quad (58)$$

similarly, the voltage at maximum power is

$$V_{MP} = \left[ nN_S V_{th} \ln\left(\frac{I_{ph} + I_0 - I_{MP}}{I_0}\right) \right] - R_S I_{MP} \quad (59)$$

From (56),(57), and (58) there is a clear dependence on  $n$  or we have three equations in four variables. The paper sweeps  $n$  from [1: 2] until the calculated  $V_{MP,calculated}$  (through (59)) matches with  $V_{MP}$  given in the datasheet with a predefined tolerance.

In the second stage, we use the  $n$  and  $R_S$  from first stage and remaining parameters will be initialized as calculated in stage 1. But as we move forward, we will perturb the value of  $R_P$  until the calculated value of  $I_{MP,calculated}$  matches with  $I_{MP}$ . To calculate the initial value we use for  $R_P$  we use (40) and (41) and after some algebraic manipulations ( $A$  is given in (37)) we reach

$$R_P = \frac{V_{MP}(V_{MP} + I_{MP}R_S)}{V_{MP}I_{ph} - V_{MP}I_0(A - 1) - P_{MP}} \quad (60)$$

At each iteration,  $I_{dark}, I_{ph}$  are recalculated by solving (38) and (39) simultaneously, while  $R_P$  is perturbed and both  $R_S$  and  $n$  are kept constant.

The algorithm fits nicely around the maximum power point and has simple mathematical implementation; however, it may converge to irregular parameter values especially the  $R_P$  value as the algorithm may continue to perturb  $R_P$  until acceptable error in  $I_{MP}$  is reached which can be difficult to reach. This result will be demonstrated in the results chapter.

#### 4.3.2.2 Laudani's method with our modifications

The true power of Laudani's method [93], is its capability to extract parameters even from a noisy IV measurement. In fitting, it does not depend only on the maximum power point but also, it tries to fit all other points which gives greater accuracy. At the expense of greater accuracy, there will be higher complexity. However, the algorithm tries to minimize the complexity by reducing the number of parameters that it will try to find and utilizing the interdependencies of these parameters as well as using best-educated initial guesses of the used two parameters. The method, then, can be used straightforwardly to reach deterministic solutions better than those achieved by other stochastic algorithms.

The extraction of SDM parameters is a nonconvex optimization problem that is multimodal with different local minima. The use of deterministic algorithms to find the global minimum of this optimization problem is highly sensitive to the initial guesses, meaning that, it can simply get trapped in one of these local minima. A common solution of this problem is to use several heuristic/stochastic algorithms like artificial neural networks and evolutionary algorithms. Although these stochastic algorithms can in general find the global minimum, but the computational cost of this achievement is very high with sometimes error higher than deterministic algorithms.

The power of Laudani's method lies in the fact that it converts the nonconvex optimization problem into a convex one and then allow regular deterministic algorithms to run finding the global minima.

First, (36) can be converted from implicit to an explicit relationship between voltage and current by means of Lambert W function as follows

$$I = f_I(V, \boldsymbol{\theta}) = \frac{R_P(I_{ph} + I_0) - V}{R_S + R_P} - \frac{nN_S V_{th}}{R_S} W \left\{ \frac{I_0}{nN_S V_{th}} \frac{R_S R_P}{R_S + R_P} \exp \left[ \frac{R_P(V + R_S(I_{ph} + I_0))}{nN_S V_{th}(R_S + R_P)} \right] \right\} \quad (61)$$

Such that  $\boldsymbol{\theta} = (n, R_S, R_P, I_{ph}, I_{dark})$  which is a vector of SDM parameters. The IV measurement is a list of points  $(V_n, I_n)$  whose count is  $N$  the optimization problem can be

written as

$$\min_{\theta} \sum_{n=1}^N [I_n - f_I(V_n, \theta)]^2 \quad (62)$$

The minimized error functional can be any other form so in our method we will use another functional as it shows higher similarity between reconstructed IV curves and measured ones which is the maximum absolute error, so the problem is now formulated as in (63) instead of (62).

$$\min_{\theta} \max_n |I_n - f_I(V_n, \theta)| \quad (63)$$

At the beginning, Laudani renames parts of the equations in (38), (39), (40) and (41) to be as follows

$$\begin{cases} EXP_{OC} = \exp\left(\frac{V_{OC}}{nN_S V_{th}}\right) \\ EXP_{SC} = \exp\left(\frac{R_S I_{SC}}{nN_S V_{th}}\right) \\ EXP_{MP} = \exp\left(\frac{V_{MP} + R_S I_{MP}}{nN_S V_{th}}\right) \end{cases} \quad (64)$$

The paper then provides two reduced forms, each of these forms formulate  $\theta$  as a function of  $(n, R_S)$  so  $\theta = \theta(n, R_S)$ .

**For the first reduced form RF#1:**

After we substitute (38) into (40) and using the expressions provided in (64) one can say that

$$I_{dark} = \frac{I_{MP} + \frac{1}{R_P} (V_{MP} - V_{OC} + R_S I_{MP})}{EXP_{OC} - EXP_{MP}} \quad (65)$$

similarly, from (41) and using the expressions provided in (64) one can say

$$I_{dark} = \frac{I_{MP} + \frac{1}{R_P} (R_S I_{MP} - V_{MP})}{\frac{EXP_{MP}}{nN_S V_{th}} (V_{MP} - R_S I_{MP})} \quad (66)$$

Equating (65) and (66), and simplifying one can find that

$$R_P = \frac{D}{I_{MP} [(V_{MP} + nN_S V_{th} - I_{MP} R_S) EXP_{MP} - nN_S V_{th} EXP_{OC}]}$$

(67)

such that

$$D = (R_S I_{MP} - V_{MP}) [EXP_{MP} (I_{MP} R_S + V_{MP} - V_{OC} - n N_S V_{th}) + EXP_{OC} n N_S V_{th}] \quad (68)$$

Similar manipulations for (38),(39),(40), and (41) will result in the following equations

$$I_{dark} = \frac{n N_S V_{th} I_{MP} (V_{OC} - 2V_{MP})}{D} \quad (69)$$

$$I_{ph} = \frac{I_{MP}}{D} [V_{OC} EXP_{MP} (V_{MP} - I_{MP} R_S + n N_S V_{th}) + n N_S V_{th} (2V_{MP} (1 - EXP_{OC}) - V_{OC})] \quad (70)$$

### For the second reduced form RF#2:

By different manipulations of (38),(39),(40), and (41) one can reach the following set of expressions

$$\left\{ \begin{array}{l} R_P = \frac{S}{EXP_{OC} (I_{MP} - I_{SC}) + EXP_{MP} I_{SC} - EXP_{SC} I_{MP}} \\ I_{dark} = \frac{1}{S} [V_{OC} (I_{SC} - I_{MP}) - V_{MP} I_{SC}] \\ I_{ph} = \frac{1}{S} [I_{SC} V_{OC} (EXP_{MP} - 1) + I_{SC} V_{MP} (1 - EXP_{OC}) + I_{MP} V_{OC} (1 - EXP_{SC})] \end{array} \right. \quad (71)$$

such that  $S = EXP_{SC} (V_{MP} + R_S I_{MP} - V_{OC}) + EXP_{MP} (V_{OC} - R_S I_{SC}) + EXP_{OC} (R_S I_{SC} - R_S I_{MP} - V_{MP})$

As Laudani stated that RF#1 is very useful when extracting information from datasheet curves, as they depend mainly on knowing the maximum power point which is accurately identifiable from datasheet measurements. However, in RF#2, one can replace  $(V_{MP}, I_{MP})$  with  $(V_n, I_n)$  for any  $n$  and achieve similar results so it is more stable against measurements error compared to RF#1.

### Defining the search space for $n$ and $R_S$

Based on [94], the following inequalities hold for both  $R_S$  and  $n$ :

- $0.5 \leq n \leq 2.5$  which is a value that is acceptable in the literature.
- $0 \leq R_S \leq R_S^{max}(n)$  such that

$$R_S^{max}(n) = \frac{n N_S V_{th}}{I_{MP}} \left[ 1 + W \left\{ - \exp \left( \frac{V_{OC} - 2V_{MP} - n N_S V_{th}}{n N_S V_{th}} \right) \right\} \right] + \frac{V_{MP}}{I_{MP}} \quad (72)$$

Based on experimentation that Laudani did, he proposed following initial values  $(n_0, R_{S_0}) = (1, 0.9R_S^{max}(1))$  to be fed to the optimization algorithm that solves (62). At the end, Laudani used 'isqnonlin' MATLAB function to do the minimization process.

### 4.3.3 Comparison between different Family 2 approaches

Both algorithms, Stornelli's algorithm[92] and Laudani's algorithm [93] were compared on both the datasheet IV characteristics and the experimental measurements that we have. The datasheet IV measurements are for our used panel type (see Table 18) and they are given at different irradiances as shown in Figure 52. We will use the NRMSE defined in (44) as a measure of the quality of the parameter extraction.

By looking to Figure 43, one can find that at low irradiance, Laudani's algorithm is best fit and at high irradiance Stornelli's algorithm will be the best fit. The value of NRMSE at different irradiance levels is shown in Figure 44. Furthermore, the value of extracted parameters is shown in Table 16. It is evident from these sets of values the multimodality of the parameter extraction problem as they both show different set of SDM parameters for the same IV characteristics. Furthermore, both  $R_S$  and  $R_p$  decrease with increasing irradiance as shown in (80) and (81), however they do not decrease with the same rate. Also, the value of ideality factor seems to be dependent on irradiance and not assumed constant.

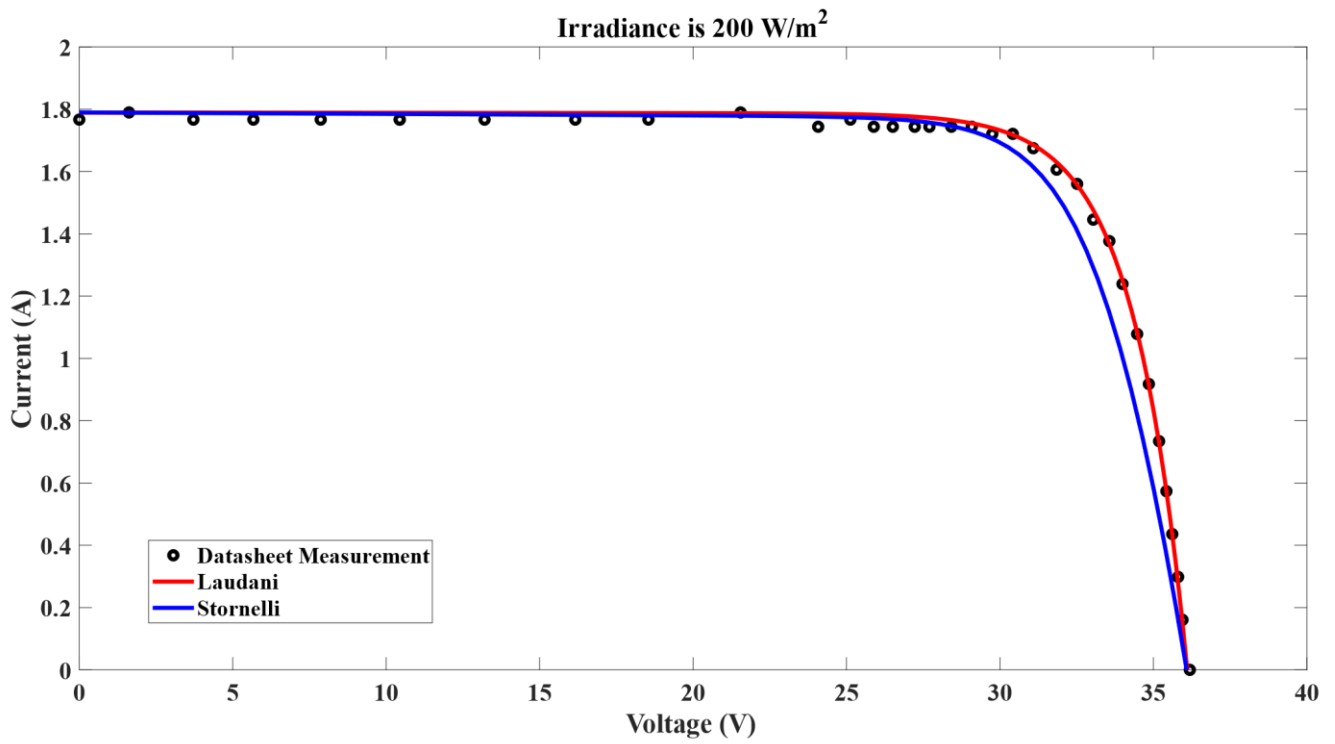
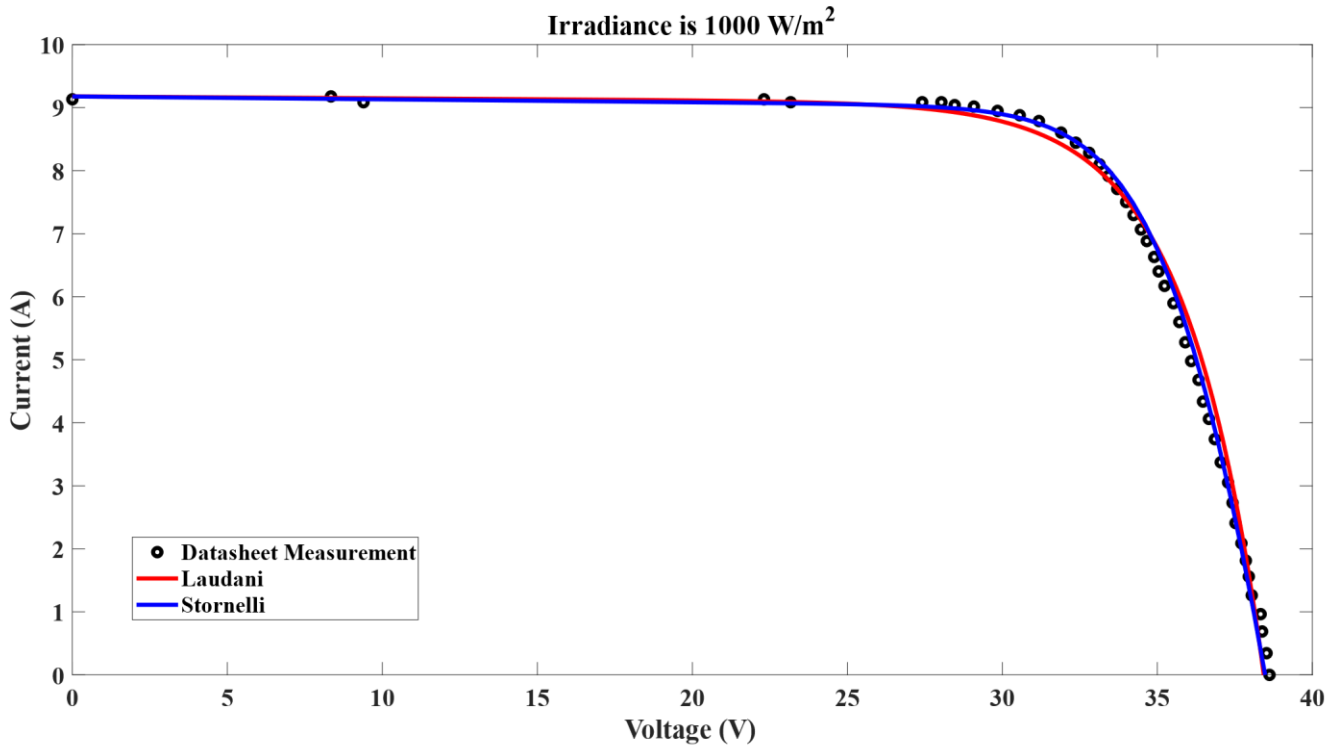


Figure 43 Fitting of both algorithms at low and high irradiance



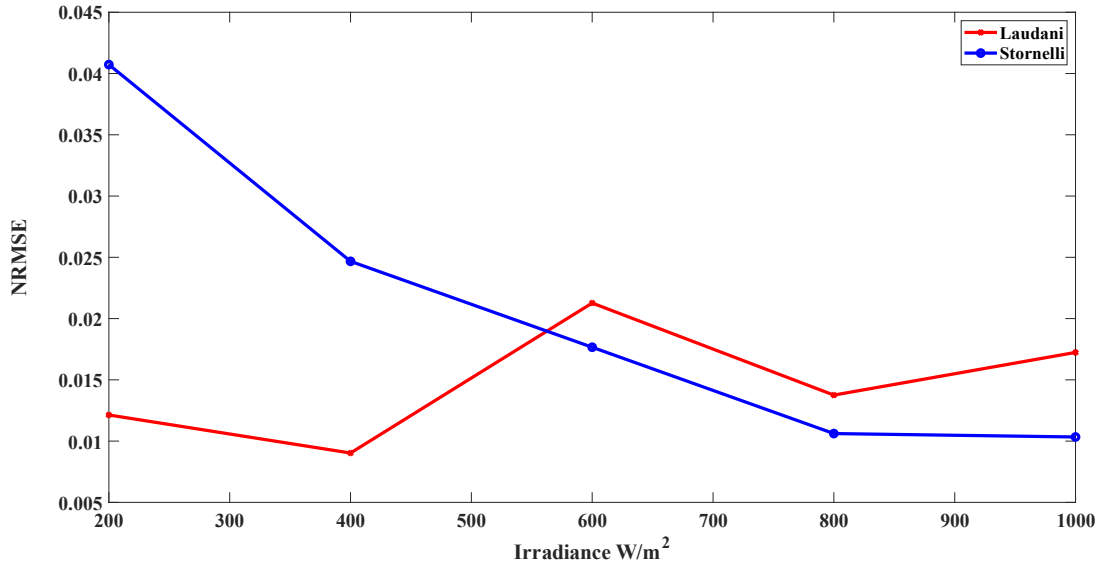


Figure 44 Error for both algorithms at different irradiance levels

Table 16 Extracted parameters using both methods

	$R_S$		$R_P$ (k $\Omega$ )		$I_{ph}$ (A)		$I_{dark}$ (nA)		$n$	
	Laud.	Stor.	Laud.	Stor.	Laud.	Stor.	Laud.	Stor.	Laud.	Stor.
<b>200</b>	1 $\mu\Omega$	0.7998 $\Omega$	12.935	2.113	1.789	1.7904	1.945	0.119	1.1347	1
<b>400</b>	1 $\mu\Omega$	0.4588 $\Omega$	1.419	1.354	3.646	3.650	57.810	0.114	1.3458	1
<b>600</b>	1 $\mu\Omega$	0.0246 $\Omega$	0.232	0.259	5.482	5.484	3.372	3.161	1.1537	1.15
<b>800</b>	1 $\mu\Omega$	0.1554 $\Omega$	0.446	0.266	7.342	7.347	614.8	0.97	1.5192	1.09
<b>1000</b>	1 $\mu\Omega$	0.1721 $\Omega$	0.347	0.216	9.178	9.185	1948.2	1.01	1.624	1.09

## 4.4 Translating circuit parameters at different environmental conditions

A very important question arises when we deal with operating solar panels is how to expect their behavior at different environmental conditions. In this regard, we reviewed [87], which provides a summary of different methods used to translate SDM parameters at different environmental conditions.

We begin by defining the intermediate variables where temperature is in  $K$  and irradiance in  $W/m^2$ .

$$\begin{cases} Irr^\nabla = \frac{Irr}{Irr_{STC}} \\ T^\nabla = \frac{T}{T_{STC}} \\ \Delta T = T - T_{STC} \end{cases} \quad (73)$$

Authors in [95], extracted the circuit parameters of Shell M55 solar panel which is made of multi-crystalline silicon. The datasheet of this panel includes IV curves at different temperatures and irradiances. It is noticed that for ideality factor, it increases with temperature and decreases with more irradiance. For series and parallel resistances, their values decrease with increasing temperature and irradiance. The photocurrent increases with both temperature and irradiance. While for the diode reverse saturation current, it increases with temperature and decreases with irradiance. Authors came with purely empirical formulas that curve-fit extracted parameters and reused them in restimulating the IV characteristics.

A good approach for translating circuit parameters is to translate industrial parameters first using simple algebraic equations either empirical or physical then do a parameter extraction algorithm on translated parameters, that is to avoid dealing with unmeasurable circuit parameters.

#### 4.4.1 Valerio's model

Valerio in [96], generalized the SDM model given in (36) to include the effect of both irradiance and temperature and be on the form

$$\begin{aligned} I(Irr^\nabla, T) = Irr^\nabla I_{ph}(T) - I_{dark}(Irr, T) \left[ \exp \left[ \frac{Irr^\nabla (V + KI \Delta T) + IR_S}{Irr^\nabla n N_S V_{th} T} \right] - 1 \right] \\ - \left[ \frac{1}{R_p} (Irr^\nabla (V + KI \Delta T) + IR_S) \right] \end{aligned} \quad (74)$$

given that  $K$  is called curve correction factor and it is defined in the IEC891 standard. The photocurrent depending on temperature and irradiance is given by (75) where  $\mu_{isc}$  is the thermal coefficient of short-circuit current in  $A/C^\circ$

$$I_{ph}(Irr^\nabla, \Delta T) = Irr^\nabla (I_{ph,STC} + \mu_{isc} \Delta T) \quad (75)$$

and empirically, the dependence of diode current on both temperature and irradiance can be expressed recursively as a dependence on temperature like in (75)

$$I_0(Irr^\nabla, T) = \exp \left[ 1.25 (Irr^\nabla - 0.2) \ln \left( \frac{I_0(1, T)}{I_0(0.2, T)} \right) + \ln (I_0(0.2, T)) \right]$$

(76)

The total photocurrent in (74) changed with irradiance and temperature and it agreed with the trend found in [95]. The dependence of diode reverse saturation current also increases with irradiance as shown in (76). However, the new  $R_S$  can be expressed as (77) and both  $R_p$  and  $n$  are constant

$$R_S(Irr^\nabla, \Delta T) = K\Delta T + \frac{R_{S,STC}}{Irr^\nabla} \quad (77)$$

#### 4.4.2 Short-circuit current model

Many authors [96]–[98] adopted (75) as a relation for short-circuit current variation. However, some researchers noticed the nonlinear change of short-circuit current with irradiance, so they raised  $Irr^\nabla$  to the power  $\alpha$  in (75). This exponent has value close to 1 and is given by (78)

$$\alpha = \ln\left(\frac{I_{SC,1}}{I_{SC,2}}\right) / \ln\left(\frac{Irr_1}{Irr_2}\right) \quad (78)$$

#### 4.4.3 Open-circuit voltage model

Several models were reviewed for finding the dependence of  $V_{OC}$  on the irradiance and temperature in [87], but we chose the one showing dependence on both temperature and irradiance [96], [97], [99]–[101] as shown in (79)

$$V_{OC}(Irr^\nabla, \Delta T) = V_{OC,STC} + \mu_{voc}\Delta T + C_1 \ln(Irr^\nabla) + C_2 \ln(Irr^\nabla)^2 + C_3 \ln(Irr^\nabla)^3 \quad (79)$$

The coefficients  $C_1 = 5.4685 \times 10^{-2}$ ,  $C_2 = 5.9739 \times 10^{-3}$  and  $C_3 = 7.6162 \times 10^{-4}$  for silicon and  $\mu_{voc}$  is the thermal coefficient of  $V_{OC}$  in  $V/C^\circ$ . However, we find this empirical equation highly dependent on panel type and for our study, we use specific coefficients for each panel type that best-fit datasheet values.

#### 4.4.4 Series and parallel resistance model

In [87], it was shown that parallel resistance is either assumed constant or changes only with irradiance so

$$R_p = \frac{R_{p,STC}}{Irr^\nabla} \quad (80)$$

And  $R_S$  can change linearly as in (77) or logarithmically depending on irradiance and temperature as shown in

$$R_S = T^\nabla(1 - 0.217 \ln(Irr^\nabla))R_{S,STC} \quad (81)$$

#### 4.4.5 Ideality model

Based on [102], ideality is assumed to depend only on temperature by

$$n = n_{STC} T^\nabla \quad (82)$$

However, it was shown in [95] that depends on the logarithm of irradiance as well. This conclusion seems to be panel specific. For instance, in [103], a physics-based model was developed for a mono-crystalline solar cell. In this study, the ideality decreased with increasing the temperature for low irradiance and increased nonlinearly at high irradiance. On the contrary to [95], it increased with increased irradiance. However, the range of ideality variation in all situations is relatively small so it is safer to keep the ideality independent on environmental conditions to avoid panel-specific conclusions. Or provide a suitable empirical formula for each type of commercial panels which is tedious as many datasheets do not include IV measurements at different temperatures.

#### 4.4.6 Photocurrent and diode reverse saturation current model

Both photocurrent and diode reverse saturation current can be given in terms of  $R_S, R_P, I_{SC}, V_{OC}$  and  $n$ , so we can solve (38) and (39) simultaneously and use (64) to find (83)

$$\begin{cases} I_0 = \frac{I_{SC} - (C - D)}{EXP_{OC} - EXP_{SC}} \\ I_{ph} = EXP_{OC} I_0 + C \end{cases} \quad (83)$$

given  $C = V_{OC}/R_P$  and  $D = I_{SC}R_S/R_P$ .

#### 4.4.7 Efficiency model

In most datasheets, there is given a thermal coefficient for the maximum power  $\mu_{mp}$  (given in  $W/C^\circ$ ) so

$$P_{MP} = Irr^\nabla (P_{MP,STC} + \mu_{mp} \Delta T) \quad (84)$$

plugging (12) into (84) one can reach

$$\eta = \eta_{STC} + \frac{\mu_{mp} \Delta T}{A Irr_{STC}} \quad (85)$$

Another solution is to find  $I_{MP}$  and  $V_{MP}$  by solving (40) and (41) simultaneously (numerically), then using (12) we can find efficiency and maximum power.

#### 4.4.8 Verifying parameter translation from datasheet measurements

To test the accuracy of our parameter translation module, we could compare the IV curves

found in the datasheet(see Figure 52 and Table 18 for specifications of used panel) by IV curves generated when parameters are translated from STC to other irradiances. First, we found the  $V_{OC}$  correction factors in (86) by linearly fitting data from datasheet together and they were  $[c_0, c_1] = [-0.0119, 1.5321]$ . Afterward, we used the method `pv_analyser.panel.translate_parameters()` to find translated curves at different irradiance levels, then we compared our expectations to the datasheet recorded values. A comparison between expectations and datasheet value is shown in Figure 45, and it is shown that at low irradiance the expected maximum power is lower than actual value and this error diminishes as we increase irradiance. The accuracy of the parameter translation against irradiance is shown in Figure 46 and it shows greater accuracy at higher irradiances.

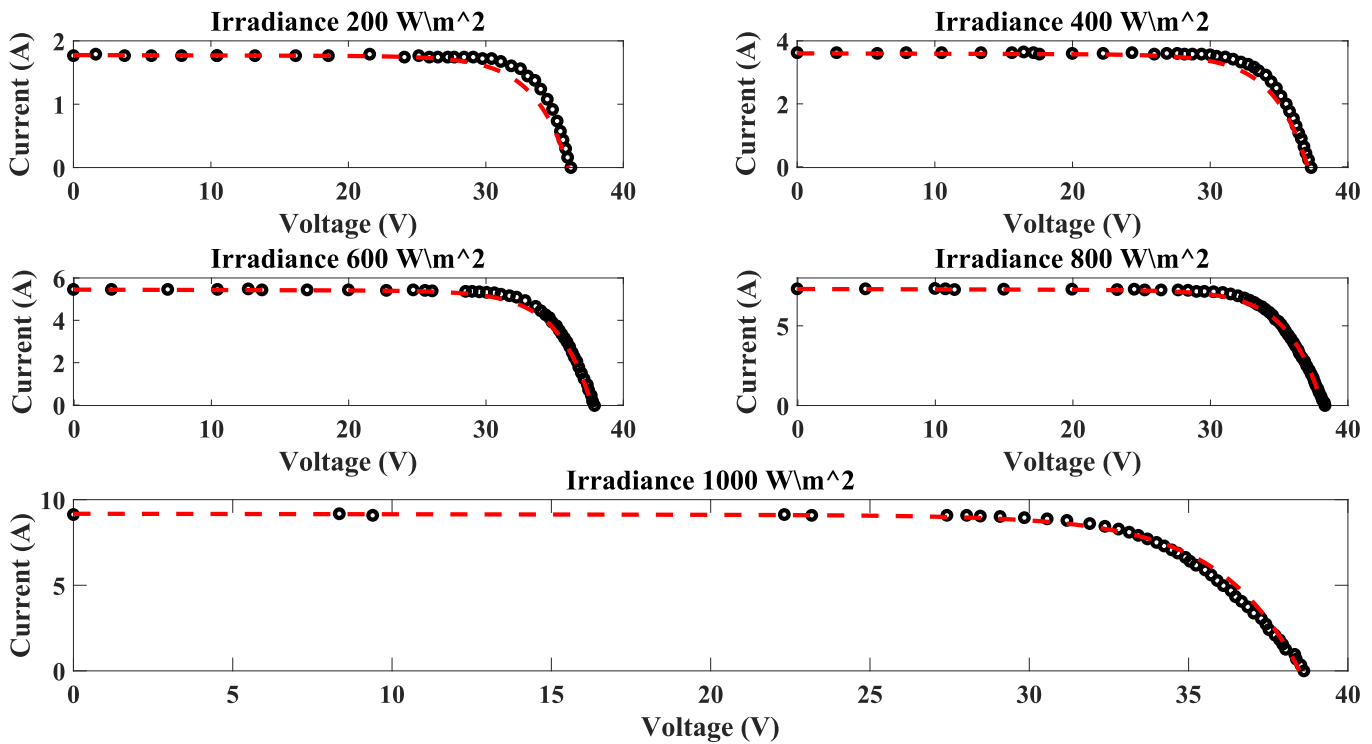


Figure 45 Curves translated from STC curve compared to the datasheet value (in dots)

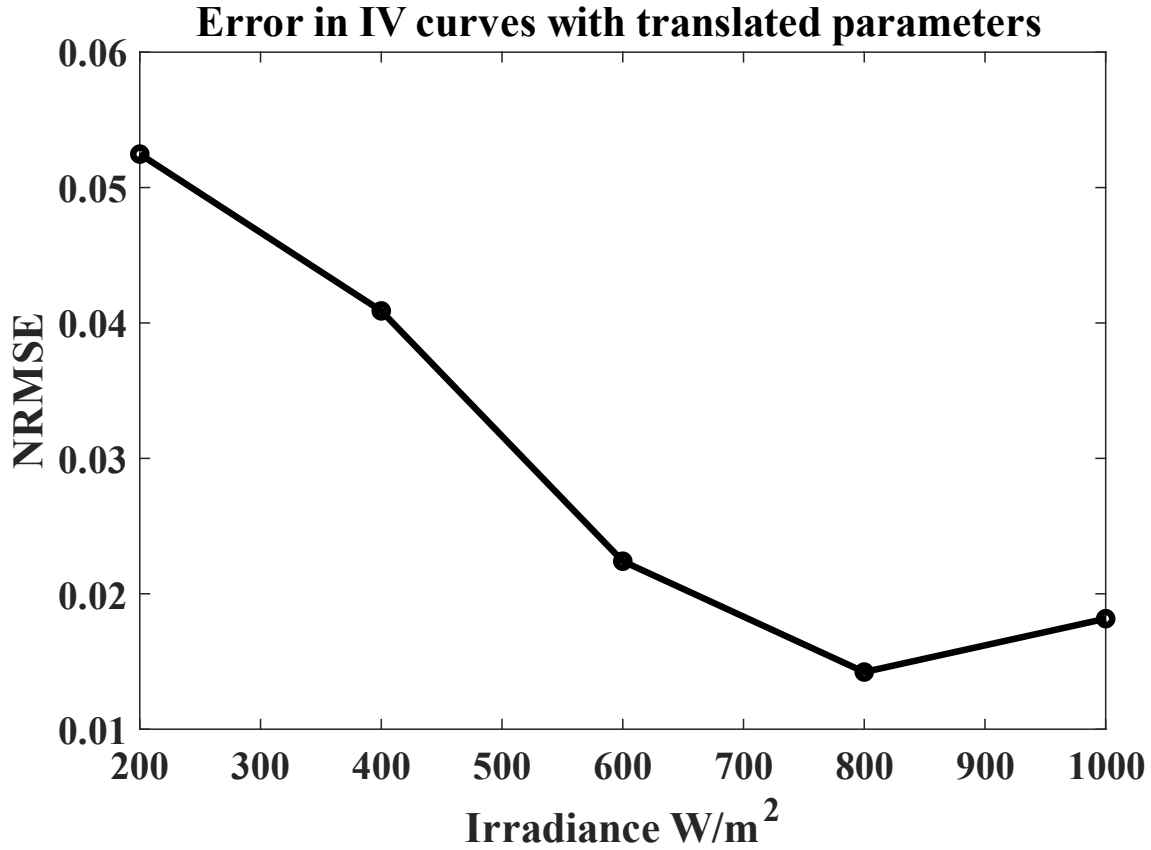


Figure 46 Error in translated IV curves when parameters are extracted initially by Laudani's algorithm

## 4.5 Summary

The aim of this chapter is to be able to build an accurate model capable of simulating a solar panel under various environmental conditions.

At the beginning, we modelled the two important components of the environmental conditions: temperature and irradiance. We noticed that the cell temperature will differ than ambient temperature. The reason behind this is how the panel is fixed in the station and how air circulation cools it. Furthermore, the amount of incident irradiance also affects the temperature of the panel. For irradiance, it depends on the position of the sun throughout the day and the positioning of the panel itself, and we tried to calculate the irradiance component normal to the surface of the panel.

The other component is modelling the panel given its environmental conditions. We utilized the single-diode model for its simplicity and robustness. We could model the whole panel given that each cell has different parameters of its single-diode model. At the end, we gave a simple equation that approximates the current-voltage characteristics when irradiance is distributed uniformly over the panel.

A big issue comes to surface when we want to know the values of single-diode model parameters from a current-voltage measurement and we elaborated on different methods available in the literature to do this task, then for sound reasons, we advised the use of a modified

version of a numerical algorithm.

Finally, to judge the performance of a panel given some environmental conditions, we showed how single-diode model parameters change in different environmental conditions.

At the end, a complete model of the panel is produced from bottom up and in various environmental conditions.

# Chapter 5

## Installed Site and Analysis Module

In this chapter, we demonstrate the installed site capabilities and a complete description of the analysis module used to model different faults, and to be integrated with actual station for the purpose of implementing analytics of all types.

### 5.1 Site Description

#### 5.1.1 Location

The solar power plant is installed within the American University in Cairo, AUC, campus, at  $30.017695^{\circ} N$ ,  $31.506666^{\circ} E$  with  $328\text{ m}$  altitude above the sea level. A satellite view of the station location is shown at Figure 47. The tilt angle of installed panels is  $26^{\circ}$  and the azimuth of installed panels (calculated from station satellite view) is  $143.1301^{\circ}$  where zero azimuth is aligned at the north and  $180^{\circ}$  azimuth is toward the south. Since the location has a sandy environment, its albedo is 0.4 (see Table 11) and its fixture is open-rack glass front and polymer back (see Table 10).



Figure 47 Actual installed station V.S. satellite view from Google Maps

The Global Solar Atlas [104] provides useful information about expected power production of installed station alongside with other environmental parameters like those shown in Table 17. The maximum power production of the station per year is  $2372.7\text{ kWh/m}^2$  of the station area which occurs when panels are tilted at  $29^{\circ}$ .



Table 17 Irradiance incident on station per year, best panel tilt angle and maximum power production per year

Parameter	Value
Direct normal irradiation	2171 kWh/m <sup>2</sup>
Global horizontal irradiation	2147.5 kWh/m <sup>2</sup>
Diffuse horizontal irradiation	724.4 kWh/m <sup>2</sup>
Global tilted irradiation at optimum angle	2381.2 kWh/m <sup>2</sup>
Optimum tilt of PV modules	29°
Total Global tilted irradiation	2372.7 kWh/m <sup>2</sup>

Panels are numbered for simulation purposes as shown in Figure 48.

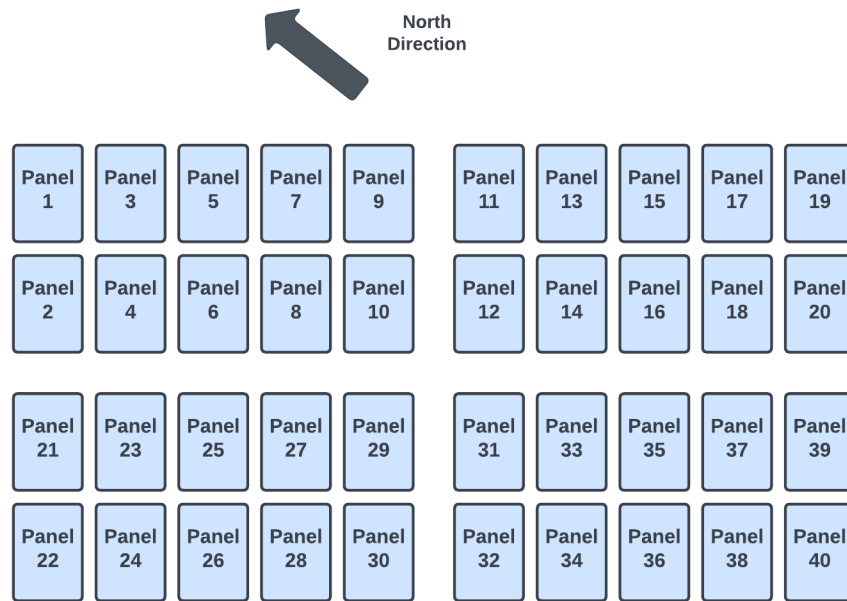


Figure 48 Panel numbering

### 5.1.2 System architecture

The station topology is on-grid topology as shown in Figure 49. It consists of 5 panel strings, each string has 20 solar panels (total 100 panels), Two strings are connected to the inverter's input (40 panels in total are considered active), the inverter's output is connected to the AUC grid on one hand through the AC output switchboard that contain switching elements and a bidirectional energy meter, and on the other hand to the AUC grid connection switchboard, which is the first interface of the plant with the grid. The AC output switchboard and the AUC grid connection switchboard are connected through an 80-m AC, 4-wire cable, and all equipment are earthed for personnel safety and proper functioning of the equipment.

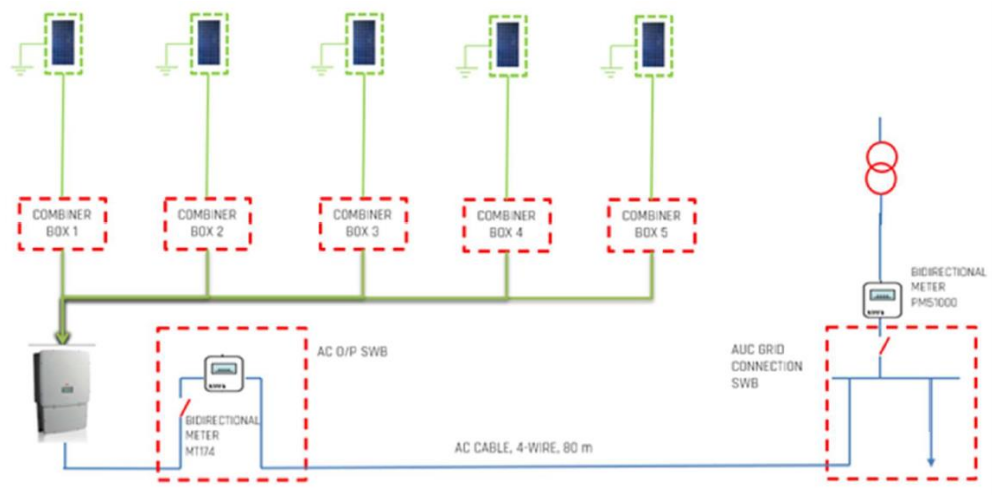


Figure 49 On-grid topology of the station

The logical architecture of the station is composed of panels, characterizers, power conversion, weather station, network communication and the analysis module. The interconnection of these parts is shown in Figure 50. On-site devices refer to the inverter and the weather station. Characterizers are interconnected with an MQTT broker implemented on a RaspberryPi board. Besides, the backend is a control system interfacing the database having logs of all IV characterizations beside all readings of weather and inverter data. Also, the backend controls the rate at which characterizations of the 40 active panels are made (e.g., how many times a day panels are characterized). The backend is connected to the GUI and to the analysis module that gives insights about current performance of the station, which is in fact the core of this thesis.

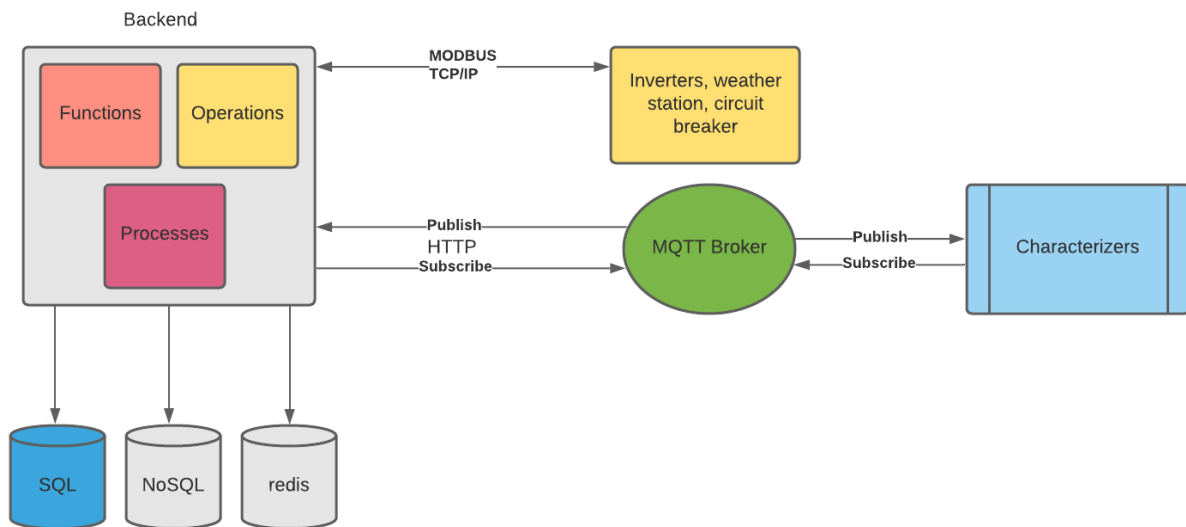


Figure 50 System Architecture

### 5.1.3 Panel specifications

The panels installed in the site (as of Dec. 2022) are of the type Suntech STP275-20/Wfw[44] shown in Figure 51 and they have the following specifications shown in Table 18. In addition, the standard panel IV characteristics at different irradiance conditions can be found at [105] as CSV files and they are depicted at Figure 52.

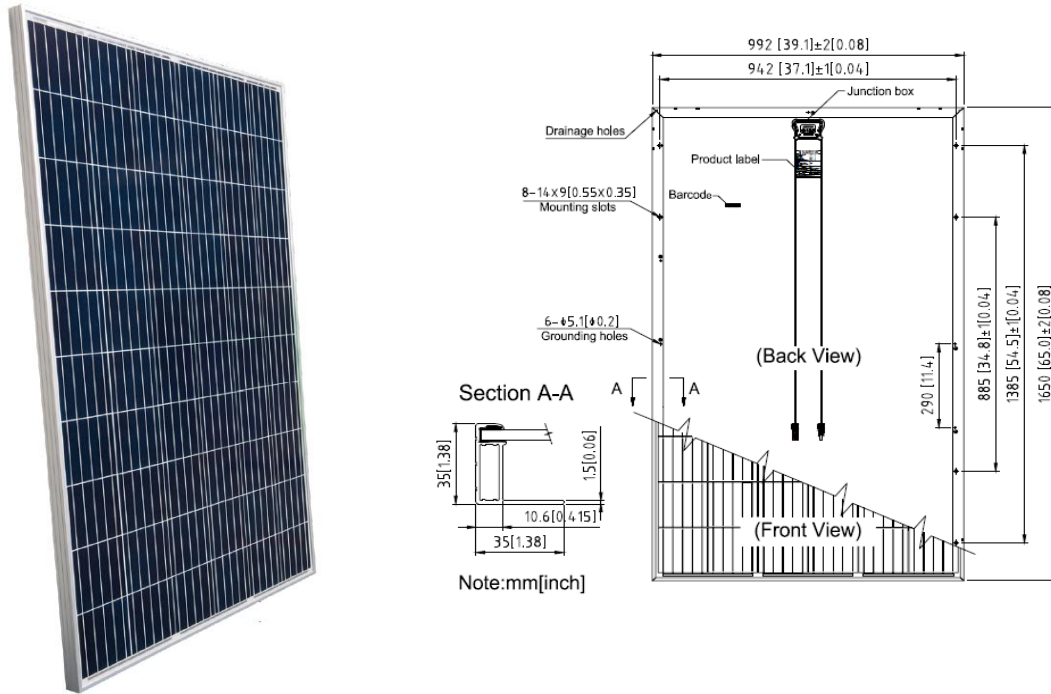


Figure 51 Actual panel used with a schematic showing its dimensions

Table 18 Specifications of panel type Suntech STP275-20/Wfw

$P_{MP}$	275 W	Temperature Coefficient of $P_{MP}$	-0.41%/K
$V_{MP}$	31.2 V	Temperature Coefficient of $V_{OC}$	-0.33%/K
$I_{MP}$	8.82 A	Temperature Coefficient of $I_{SC}$	0.067%/K
$V_{OC}$	38.1 V	Cell Type	Polycrystalline cells of 6-inch diameter
$I_{SC}$	9.27 A	Number of cells	6 columns × 10 rows ( $c = 60$ )
$\eta$	16.8%	Dimensions	1.65 m × 0.922 m (Area is 1.5213 m <sup>2</sup> )
Operating Temperature	-40°C to 85°C	Junction Box	IP68-rated three bypass diodes (every two columns are shunted with a diode)

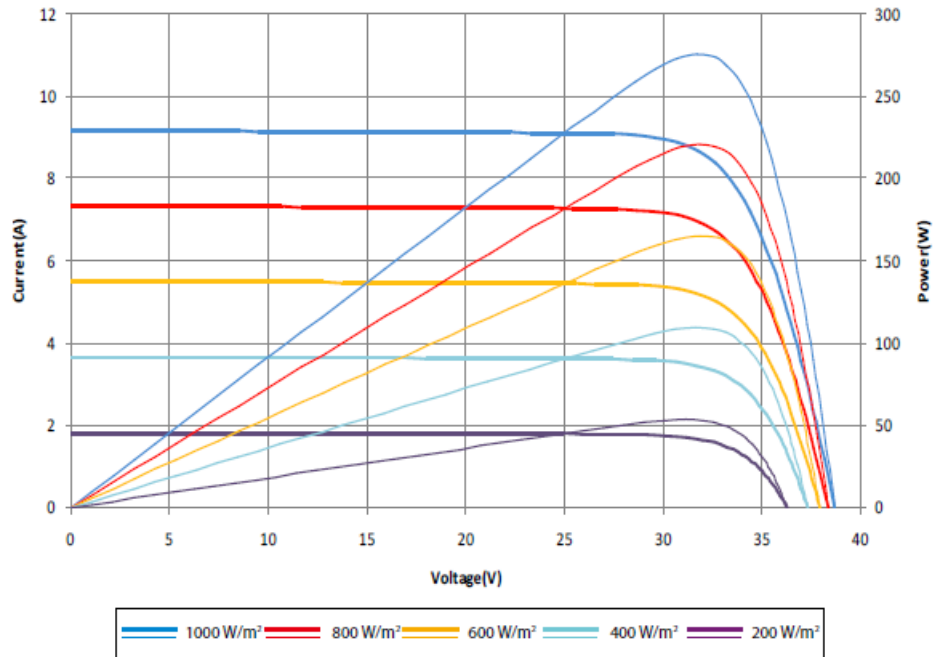


Figure 52 IV characteristics of used panel at different irradiance levels

#### 5.1.4 Characterizers

Characterizers (as shown in Figure 53) are used to collect IV readings from each panel of the 40 active panels. They are designed, tested, and calibrated by CND research team. As there is multiple phases of their design we had two different versions that we will assess in our analysis.



Figure 53 Characterizers used in this research developed by CND

### 5.1.5 Power conversion

Solar energy conversion from DC to AC and stabilizing the energy output with the grid is performed by the inverter, also known commercially as the power conditioner or grid-tied inverter or the string inverter. Besides its main two functions, the inverter is a multifunctional device that has numerous advantages in the power system, so we selected the inverter with an additional combiner box, the -SX400, which adds more control, protection, and measurement features to the inverter such as measurement of string currents and fuses to protect the input of the inverter and surge arrestors to protect the DC and AC lines. For economic reasons, a single inverter is installed whose type is TRIO-27.6-TL-OUTD manufactured by ABB, and it is shown in Figure 54 with specifications given in Table 19.

A wireless communication datalogger has been installed in the inverter, the wireless datalogger is an accessory supplied with the ABB inverter and its type code is VSN300. The datalogger sends information over Modbus TCP protocol to the ABB Webserver through the plant gateway.



Figure 54 ABB inverter of model TRIO-27.6-TL-OUTD

The internal circuit of the inverter can be divided into four main circuits, the DC input circuit, the AC output circuit, the power module circuit and the communication and control circuit.

The power module circuit is the main switching circuit consisting of IGBT power modules for DC to AC conversion besides other functions. It consists of two MPPT inputs (two DC-DC converters) to reduce string mismatch issues, hence both MPPTs are connected in parallel to the DC link (Bulk capacitors) which clears the DC ripple from the waveform, and on the other side the DC link is connected in parallel to the power module, which takes the DC input from the DC link and converts it to three-phase AC power, which in turn is connected to line filters in series, furthermore, the AC line is protected by an AC surge arrestor.

The DC input circuit is embedded in the -S2X400 inverter combiner box, it consists of two MPPT inputs. Each MPPT input consists of five parallel inputs, total inputs are 10. All DC inputs are protected by fuses on the positive and negative wires and input currents are sensed and data is sent to the control unit for display, and each MPPT line is protected by a surge DC surge arrestor to protect the input from voltage transients exceeding the maximum input voltage.

Table 19 Specifications of TRIO-27.6-TL-OUTD by ABB

<b>Absolute maximum DC input voltage</b>	<b>1000 <math>V_{DC}</math></b>
<b>Rated DC input voltage</b>	620 $V_{DC}$
<b>Number of independent MPPTs</b>	2
<b>Maximum DC input power for each MPPT</b>	16 kW
<b>Maximum DC input current for each MPPT</b>	32 A
<b>Maximum DC input current</b>	64 A
<b>Rated output AC power</b>	27.6 kW
<b>Maximum output AC power</b>	27.6 kW
<b>Rated AC grid voltage</b>	400 V

### 5.1.6 Weather station

An environmental measurement system (shown in Figure 55) is installed to measure the environmental conditions on-site. It is a system consisting of a weather station, a rain bucket, a control switchboard a data logger and solar backup power. The weather station can measure solar radiation, atmospheric pressure, humidity, ambient temperature, wind speed and wind direction. An additional rain bucket is installed to measure rain/precipitation.



Figure 55 Installed weather station

The weather station uses a data logger (shown in Figure 56 ) to convert the SDI-12 signals into other protocols suitable for communication over the communication network. Furthermore, it is essential to store historical data and it can also transmit the data over the cellular network in case there is a problem in the communication network.



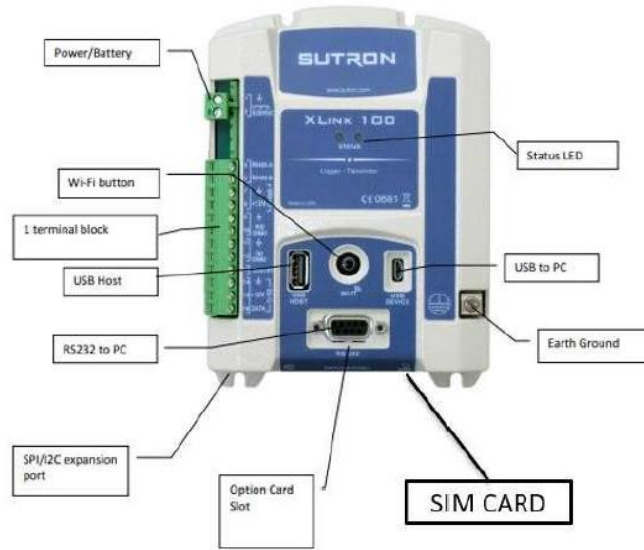


Figure 56 Data-logger for the weather station- main ports

### 5.1.7 Communication with station

A wide area network communication system has been installed, with several local area networks, LANs, that organize communication between the station and all partners in the project. Every device in the station LAN has an IP address and should communicate over the industrial protocol Modbus-TCP except for panel characterizers that communicate through wireless MQTT protocol. The inverter communicates over Modbus TCP directly through standard IEEE 802.11 wireless communication, and the data is received by the router, which sends it to the webserver used for the project. An image of the communication box used in the station is shown in Figure 57.

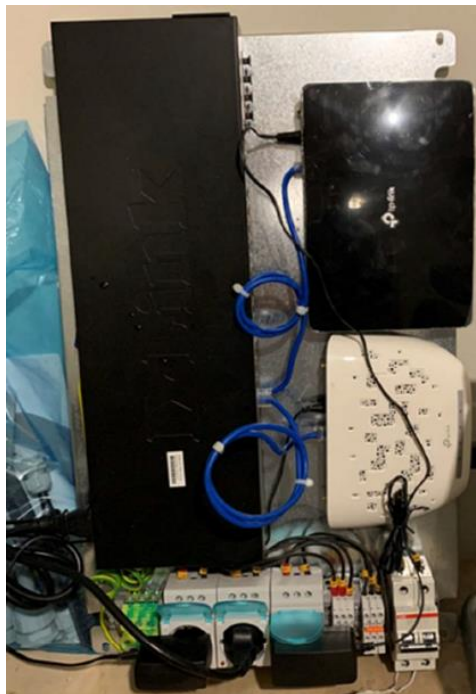


Figure 57 Communication box used at the station

# 5.2 Analysis Module

The full module (shown in Figure 58) is written in python 3.7 can be found in [43]. It includes the setup file “setup.py” that installs all required python packages. The analysis module has some dependencies which are other python packages, some functions and, finally, some python classes designed to model different solar panels and their respective measurements from the station. The analysis module has the capability to model a solar panel beginning from a cell to an array, even when each cell has its own set of SDM parameters. In this regard, we have previously demonstrated several phenomena that could be modelled with our module. An exact description of the module functionality is found in the appendix.

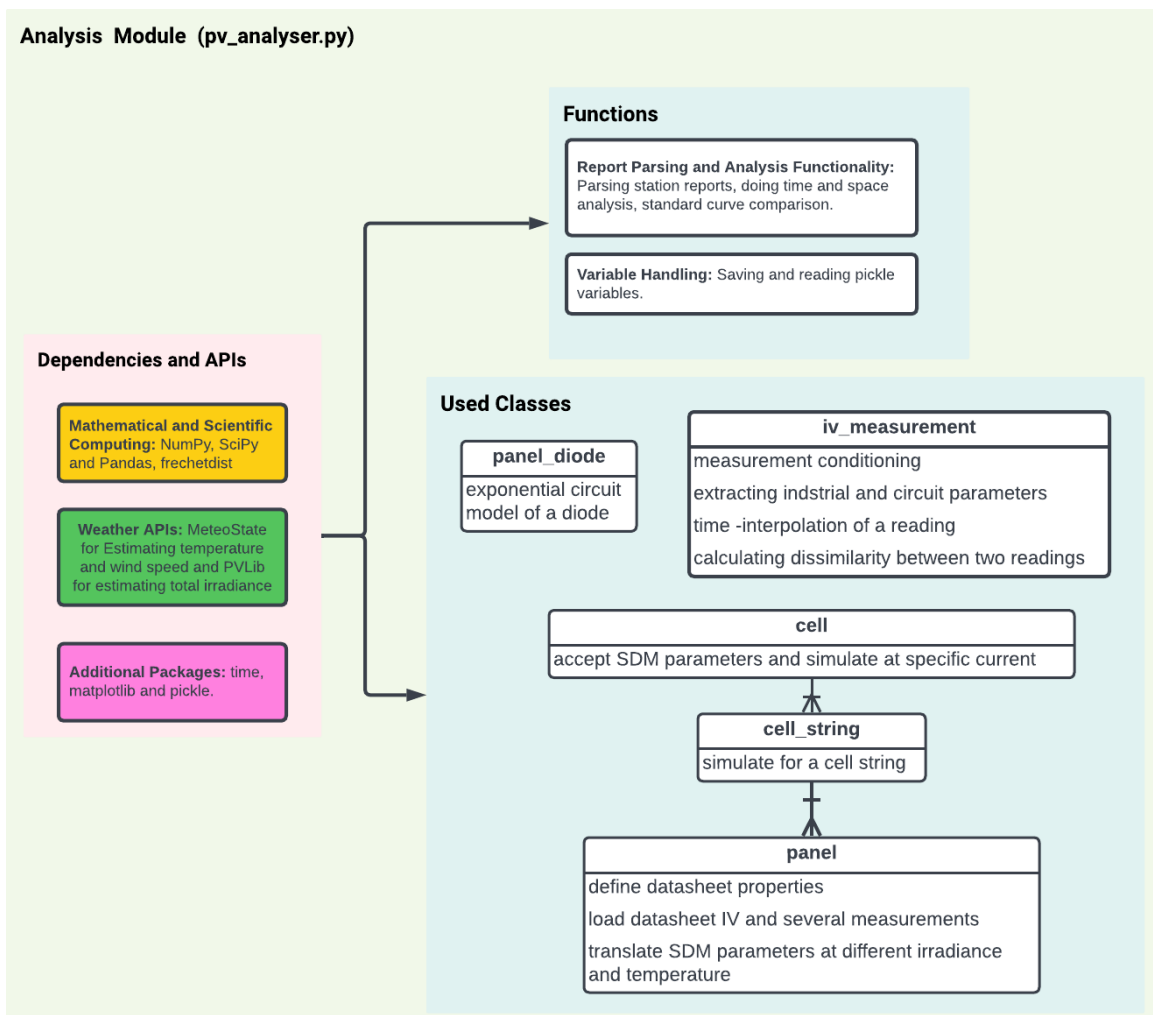


Figure 58 Architecture of analysis module



## 5.3 Summary

In this chapter, a full description of the real system that we used to conduct our research is developed- beginning from the physical station, its location and topology passing by the specifications of installed panels and the characterizers used to collect measurements from the station. Besides, the communication layer used to collect and organize collected data from the station is described as well. The other part of the story is how we are going to analyze collected data by means of an analysis module written in Python 3.7 and based on panel-in-field modelling we explained in chapter 4. So, at the end, we have the hardware and the collected data needed to be analyzed by proper means.

# Chapter 6

## Analysis Procedures and Results

In this chapter, we will begin describing the dataset we have from the installed station and try to assess its quality and the quality of characterizers in different aspects. As we proceed to do our analysis, we will assess the quality of our analysis module, its capability to emulate different faults and extract them. The real power of our analysis begins from the capability of extracting SDM parameters and translating them into different environmental conditions. Finally, we will conduct a space and time analysis of the dataset and reach some conclusions.

### 6.1 Description of Dataset

The first dataset included two active characterizes (first version) attached to panels 1 and 2 (see Figure 48). The dataset includes 8184 readings between June 20, 2021, to October 18, 2021. The number of daily readings varies through this duration as shown in Figure 59. Of these readings 4555 readings were by characterizer 1 and 3629 readings by characterizer 2.

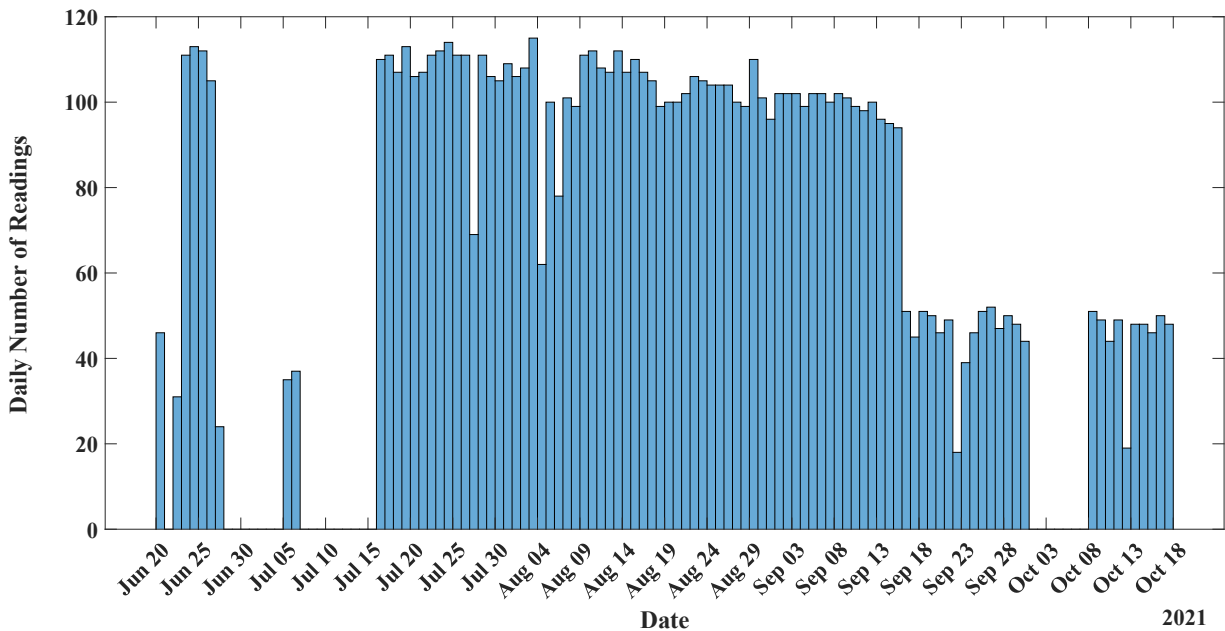


Figure 59 Daily number of readings in dataset 1

The second dataset included thirty-nine active characterizes (second version) between March 10, 2022, and June 8, 2022, with 37466 accepted readings out of 39539 (94%) The number of daily readings through this dataset is shown in Figure 60. Also, the number of active characterizers changed through the time of acquiring the dataset as in Table 20. It is noteworthy that the number of daily readings decreased when higher number of characterizers were active. Not all characterizers have the same proportion of readings as shown in Figure 61. For instance, panel number 39 has no readings at all, and panels 12, 33 and 38 have very little number of readings compared to other panels.

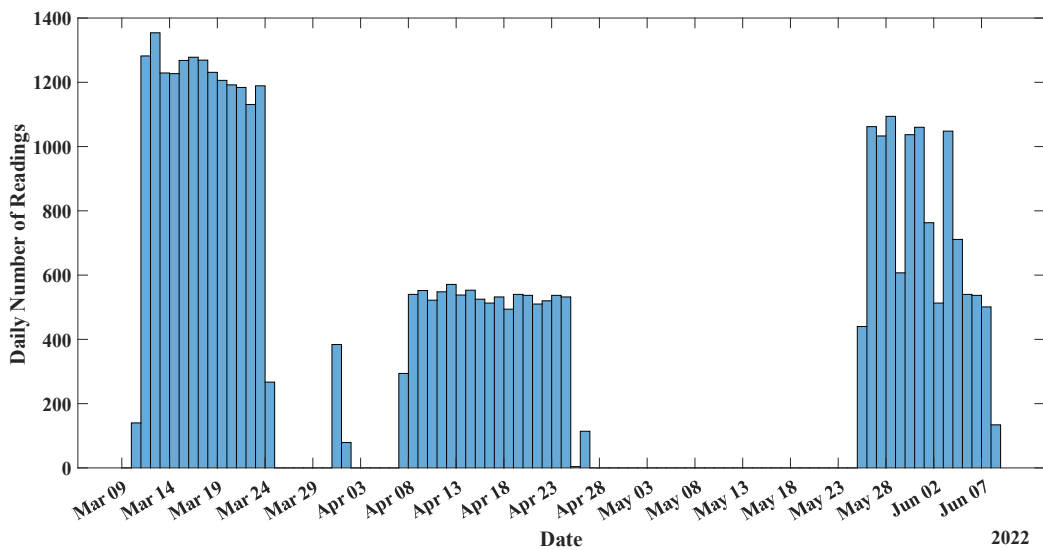


Figure 60 Daily number of readings in dataset 2

Table 20 Number of active characterizers throughout time

By the beginning of this date	Number of active Characterizers
March 11, 2022	24
March 12, 2022	25
April 1, 2022	30
April 2, 2022	37
April 8, 2022	39

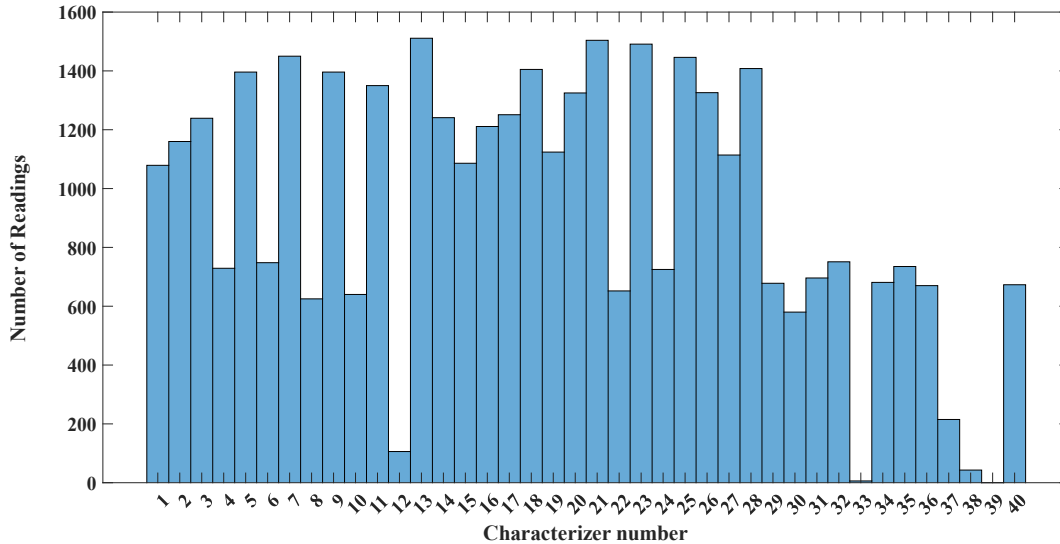


Figure 61 Readings by each of the active characterizers

## 6.2 Limitations of characterizers

The quality of IV measurement depends on the quality of the characterizer itself and it shows to which extent we can rely on these measurements to derive conclusions about station faults.

### 6.2.1 Characterizer measurements irregularities

Both datasets collected included different types of irregularities which we will discuss below. To remove these irregularities readings with point count lesser than a specific threshold (5 by default) were discarded and those with negative values were removed as well, Moreover, all sampled measurements were conditioned with the function `pv_analyser.iv_measurement.extract_features` with optional input `condition_measurement` set to the value `True`.

#### 6.2.1.1 Small number of points

Occasionally, a small number of points is taken from the characterizer when it replies to two consecutive measurement requests at low levels of irradiance. For example, check Figure 62, for a reading from dataset 2 with lesser than five points exactly before the sunset.

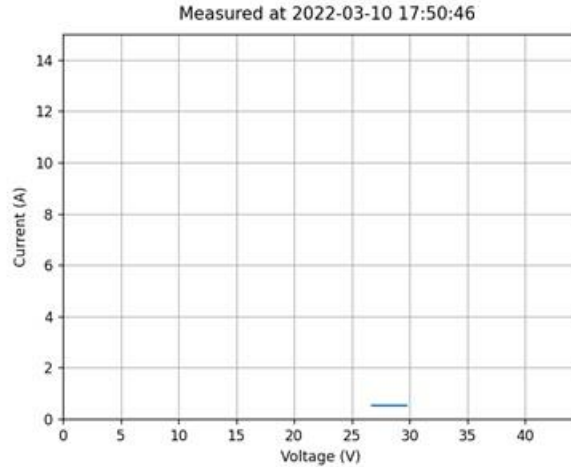


Figure 62 Small number of points before sunset

### 6.2.1.2 Current saturation near short-circuit or open-circuit regions

In some readings, the current saturates above specific voltage which is mainly due to the self-powering of our characterizers from panels themselves. The problem with current saturation is that it can be mistaken to be shading effect. However, the only difference between both is that in case of shading current drops at the end after being saturated for a while. An example from dataset 2 is shown in Figure 63. On the other side, the first versions of characterizers in dataset 1 included variations near the short-circuit region of the IV characteristics as shown in Figure 64, where the response of characterizer (version 1) is so slow compared to irradiance change either increasing or decreasing irradiance.

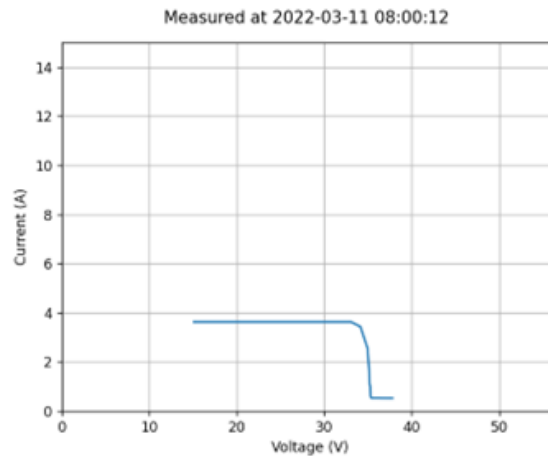


Figure 63 Presence of current saturation in some reading

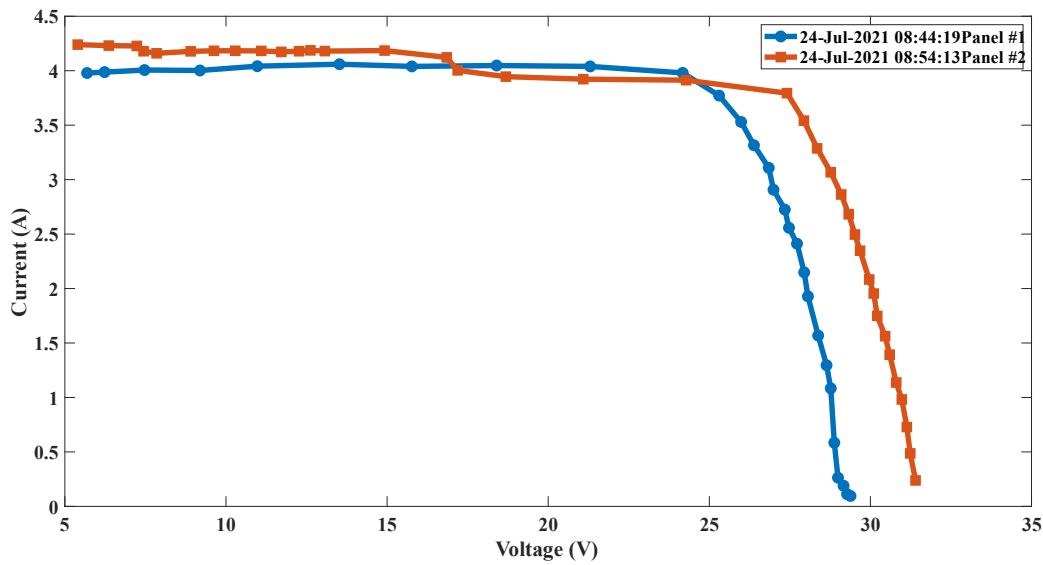


Figure 64 Problems in readings from dataset 1. Panel 1 has slight increase of current at short-circuit region and panel 2 has sudden decrease in short-circuit current before the maximum power point.

### 6.2.1.3 Missing points at low voltage

In both datasets, points were missing at low voltages as shown in Figure 64 (for dataset 1) and in Figure 63 (for dataset 2). For dataset 1, the main reason was the internal design of the characterizer while for dataset 2, each characterizer was self-powered from the panel itself which increased the minimum voltage per characterization.

### 6.2.1.4 Noisiness and varying sampling rate

Most readings were prone to noise, due to varying conditions during measurement and calibration issues. An example of noisy measurement in dataset 2 is shown in Figure 65. It is

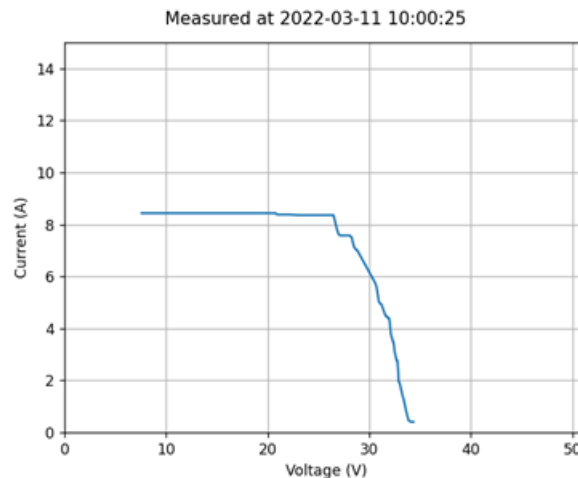


Figure 65 Noisy measurement from dataset 2

noteworthy that in both datasets there have been more voltage samples near the maximum power points and before the open-circuit point and less toward the short-circuit point. The varying sampling rate is due to the non-linearity of the used DC/DC converter within our characterizer.

An example for a conditioned reading is shown in Figure 66. It is shown that so many points are taken near the open-circuit point, with fewer near the short-circuit region. All remedies for irregular sampling, current saturation and noisiness were used to produce the shown conditioned reading.

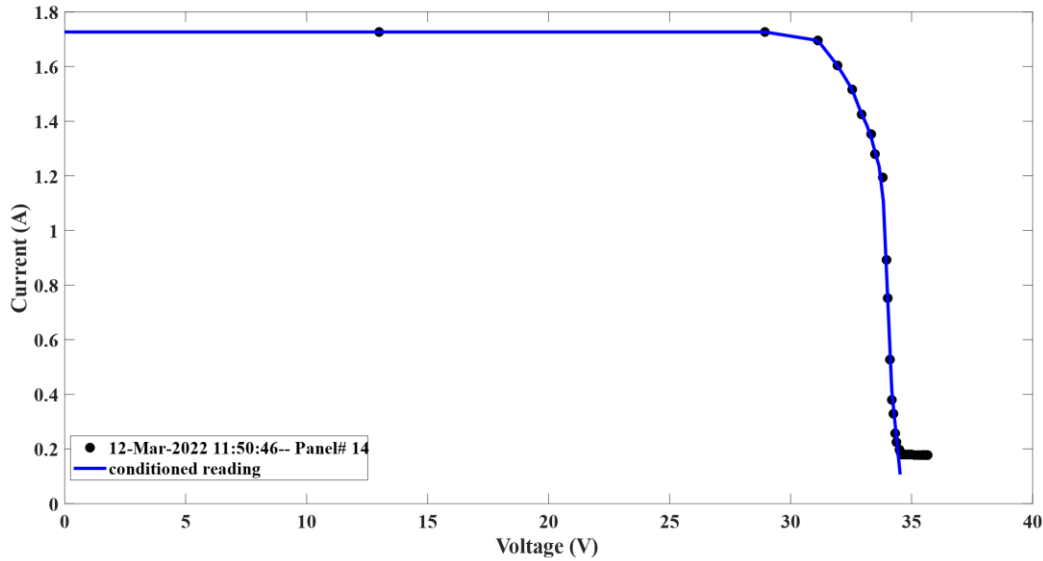


Figure 66 Original reading being conditioned

## 6.2.2 Measures for characterizers quality

To assess the quality of characterizers, we provide four measures of quality and the reasoning behind them:

1. Minimum voltage of each characterization  $V_{min}$ . It is very important to scan the IV characteristics fully to detect features such as shading or any other issues that can happen. So, the lower the value of  $V_{min}$  the better.
2. Mean voltage step  $V_{step}$  which is the average spacing between different points in the IV characteristics and the lower  $V_{step}$  the better in assessing all important regions in the IV curve.
3. Point count  $PC$ , the higher point count means better quality of the IV measurement.
4. Fill factor,  $FF$ , the reason behind having fill factor (as defined in (12)), is to ensure that the measurements given are realistic enough and to some extent follow the technology measures given in Table 6. So, this measure is technology specific, and we are here limiting its meaning to polycrystalline silicon.

The distribution of all quality parameters is shown below for both datasets.

For  $V_{min}$  (as shown in Figure 67), all of characterizers in dataset 1 has  $V_{min} \leq 6.09 V$ , while

for dataset 2,  $V_{min} \geq 7\text{ V}$  which shows clearly that the new characterizers are lesser in this aspect. The spread of  $V_{min}$  values is higher in the second dataset which means that we can lose more features than in dataset 1.

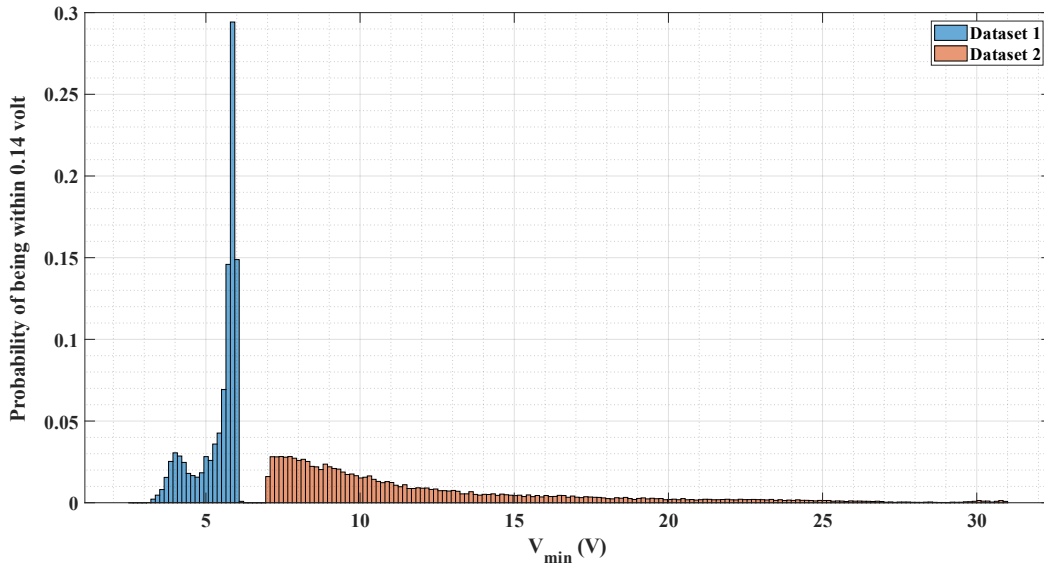


Figure 67 Probability of having a  $V_{min}$  with a specific value of both datasets

For  $V_{step}$  (see Figure 68), characterizers in dataset 2 have better resolution in their IV measurements with most of  $V_{step}$  lower than 1 volt. The mean  $V_{step}$  value dropped from 0.8348 in first dataset to 0.6635 in the second dataset which is good.

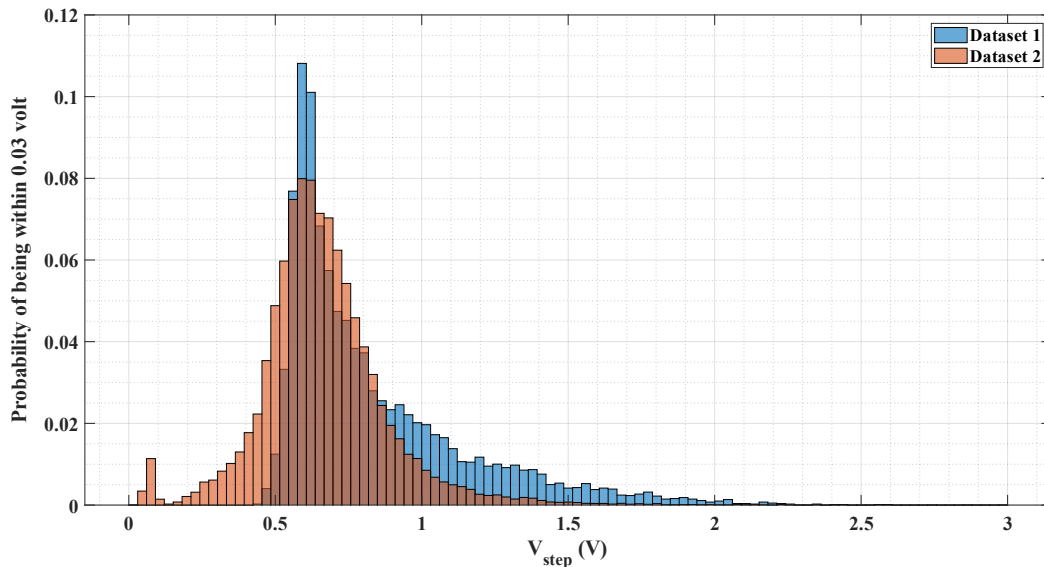


Figure 68 Probability of having a specific  $V_{step}$  for both datasets

Similarly, the point count  $PC$  was lower in first dataset it was on average 32 points then it increased to 36 points in the second dataset as shown in Figure 69. Interestingly, very high number of points was achievable by second version of characterizers.



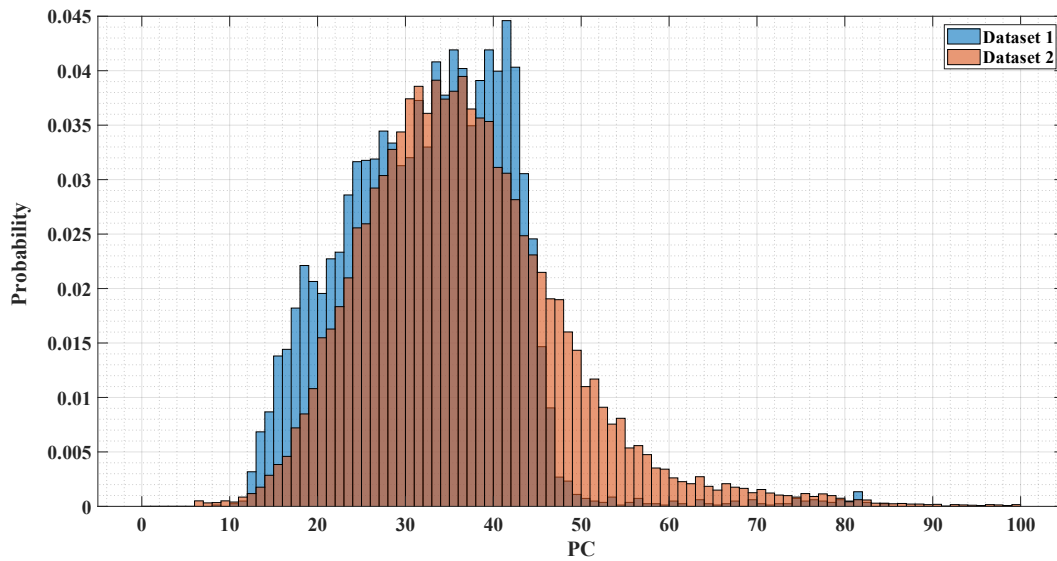


Figure 69 Probability of having a specific point count

Unfortunately, the fill factors of the second dataset are high compared to the first one (see Figure 70). The high fill factors indicate that points near the open-circuit voltage can be misrepresented. The average fill factor of the second dataset is 0.8388 compared to 0.7818 in the first dataset. Whether these values are correct given specific environmental conditions will be studied afterward.

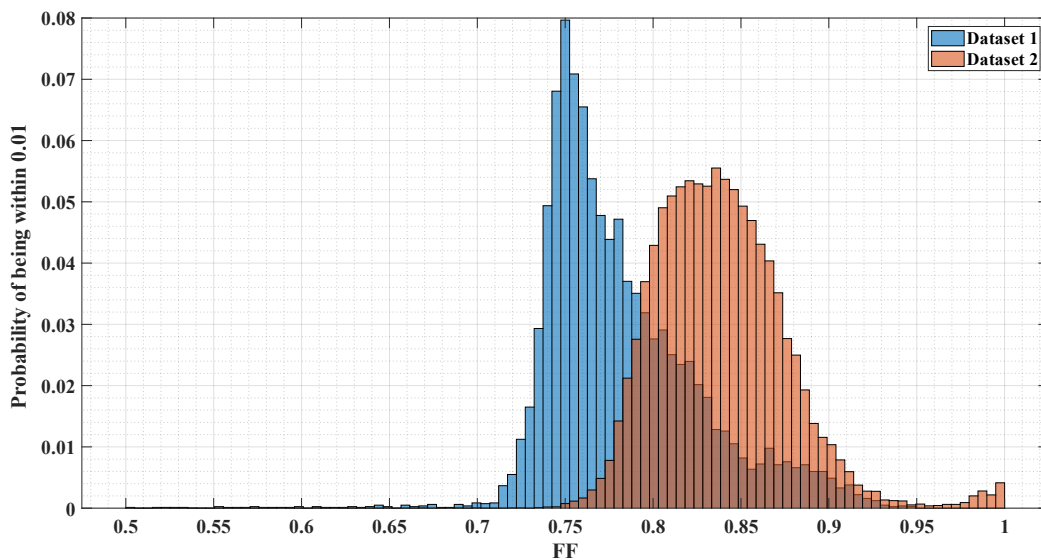


Figure 70 Probability of having a specific fill factor in both datasets

An evaluation of characterizer performance metrics is shown in Table 21 and Table 22 for both datasets. Based on Table 22, characterizer 33 has the best performance in terms of all metrics approximately, but unfortunately, this is statistically insignificant as analysis is done on 6 readings only (see Figure 61). The best characterizers we will depend on in our future analysis

are characterizers: 8 then 13 based on their good quality metrics and sufficiently high number of readings.

Table 21 Quality metrics for all characterizers in dataset 1

Panel ID	$V_{min}$			$V_{step}$			$PC$			$FF$		
	Min.	Avg.	Max.	Min.	Avg.	Max.	Min.	Avg.	Max.	Min.	Avg.	Max.
1	3.1952	5.3512	6.0905	0.44901	0.86239	3.1129	8	28.953	84	0.22184	0.78912	0.93198
2	3.2649	5.4966	6.0881	0.4501	0.80009	2.5936	10	35.685	82	0.53193	0.77261	0.94767

Table 22 Quality metrics for all characterizers in dataset 2

Panel ID	$V_{min}$			$V_{step}$			$PC$			$FF$		
	Min.	Avg.	Max.	Min.	Avg.	Max.	Min.	Avg.	Max.	Min.	Avg.	Max.
1	7.0268	11.639	26.905	0.27705	0.75672	1.725	13	32.075	54	0.53609	0.8429	0.96678
2	7.008	10.943	28.18	0.2373	0.80227	3.1546	9	30.45	54	0.67075	0.84524	0.95971
3	7.011	12.001	28.394	0.2697	0.66392	1.8896	12	36.021	64	0.75999	0.83585	0.97437
4	7.0067	11.626	26.95	0.46939	1.213	2.9992	8	21.32	36	0.52415	0.84041	0.96438
5	7.0094	11.795	28.545	0.30522	0.68921	1.3642	15	34.964	54	0.65135	0.83341	0.95094
6	7.0026	13.431	38.878	0.02868	0.42755	1.201	6	42.924	79	0.77906	0.86723	1
7	7.0156	11.774	28.7	0.2351	0.61232	1.4169	14	37.414	59	0.7851	0.85125	0.95749
8	7.0005	8.5734	20.955	0.205	0.58389	2.1272	11	49.771	97	0.7608	0.82586	0.94662
9	7.0027	12.051	30.887	0.23069	0.80743	2.1315	12	27.338	49	0.77947	0.85076	0.94526
10	7.0039	12.32	26.564	0.29925	0.75869	1.3798	13	28.553	49	0.76699	0.82999	0.94553
11	7.004	11.882	27.393	0.20842	0.67237	2.1069	12	37.007	68	0.75106	0.83198	0.95365
12	7.0021	8.8616	26.621	0.1611	0.84128	3.5044	7	46.349	133	0.58815	0.82778	0.98413
13	7.0272	12.362	27.783	0.24876	0.57822	1.3577	19	39.895	67	0.76872	0.83536	0.93882
14	7.0115	12.583	28.131	0.18083	0.52164	1.2689	17	43.545	74	0.76135	0.82824	0.95049
15	7.0021	11.789	27.445	0.22529	0.71653	1.8084	13	33.625	63	0.76766	0.84	0.9282
16	7.0001	11.664	27.826	0.18387	0.6894	1.4486	14	35.389	70	0.75903	0.82653	0.9652
17	7.0085	11.469	29.73	0.20361	0.71084	1.6344	15	33.082	68	0.77929	0.84152	0.95787
18	7.0044	11.703	27.503	0.25193	0.61085	1.8023	14	39.944	68	0.75138	0.82589	0.95214
19	7.0186	17.951	31.788	0.048292	0.66449	2.2162	10	35.3	99	0.78906	0.89344	1
20	7.0116	11.362	27.081	0.26558	0.60246	1.3731	18	38.992	71	0.7777	0.83776	0.94439
21	7.015	12.65	28.192	0.21303	0.73326	2.3438	13	29.665	49	0.77898	0.84774	0.94236
22	7.0104	11.294	24.484	0.24781	0.55245	1.0192	20	40.753	59	0.75965	0.82969	0.92895
23	7.0036	12.031	30.184	0.17905	0.58276	2.1193	12	39.52	66	0.74082	0.82563	0.92401
24	7.0205	12.395	27.629	0.18924	0.56075	1.3211	18	42.2	63	0.76862	0.83416	0.93612
25	7.0094	12.063	26.815	0.079018	0.61894	1.358	18	38.151	64	0.61648	0.83555	0.95076
26	7.0038	11.846	29.237	0.1975	0.70747	1.7971	13	32.243	51	0.77196	0.84054	0.95095
27	7.0035	11.668	26.878	0.24529	0.61358	1.4705	19	40.84	58	0.76712	0.8341	0.94264
28	7.0106	12.355	27.946	0.211	0.71322	2.2412	14	31.889	58	0.73907	0.82387	0.92492
29	7.0186	11.514	25.431	0.23001	0.608	0.95686	18	34.339	50	0.78212	0.85091	0.91399
30	7.0103	11.336	24.463	0.32777	0.78628	1.4006	15	28.626	42	0.73448	0.81527	0.89502
31	7.0259	11.542	24.625	0.299	0.70877	1.6633	16	30.559	45	0.76896	0.85068	0.91296
32	7.0352	11.181	24.724	0.28807	0.60856	1.0679	20	38.561	57	0.75212	0.81878	0.9099
33	7.0385	9.4593	12.094	0.67104	0.74231	0.87257	32	35.167	41	0.81715	0.84055	0.87677

34	7.0068	14.052	30.778	0.030733	0.2553	0.58393	15	70.443	126	0.79958	0.85002	0.98358
35	7.0006	12.134	25.239	0.20334	0.5997	1.5017	10	34.624	61	0.79911	0.8625	0.93139
36	7.0028	11.113	25.173	0.29187	0.81787	1.802	9	25.184	43	0.76878	0.82847	0.92959
37	7.0793	9.3122	23.904	0.38414	0.55217	1.0328	16	34.051	45	0.77984	0.82316	0.97006
38	7.2163	10.221	13.885	0.45262	0.69595	1.0504	26	37.07	42	0.76755	0.81794	0.86585
39	-	-	-	-	-	-	-	-	-	-	-	-
40	7.0003	10.622	24.335	0.29246	0.65228	1.3561	15	35.973	55	0.72604	0.83039	0.94265

It is also noteworthy, how characterizers' performance changes with time, to be able to detect any issues with future development of the characterizers. In Figure 71, the value of  $V_{min}$  is averaged overall the second dataset for a specific hour for three example characterizers, namely 8, 25 and 40. It is shown that at sunny hours (from 10:00 to 14:00), the value of  $V_{min}$  is at its lowest and it increases when sun goes away.

In totally opposite trend, in dataset 1, the value of  $V_{min}$  is higher during sunny time. It is favorable that  $V_{min}$  be lower when the sun irradiance is low to allow the characterizer to detect more possible issues like shading etc.

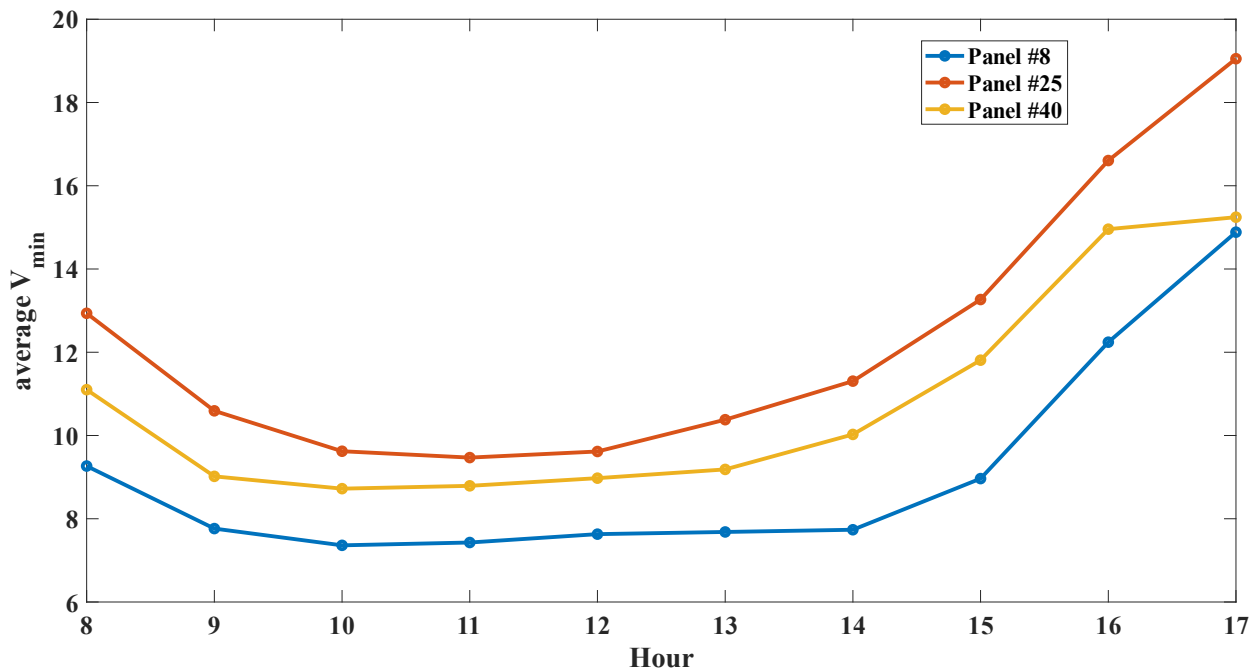


Figure 71 Change of minimum voltage against hour of the day (dataset 2)

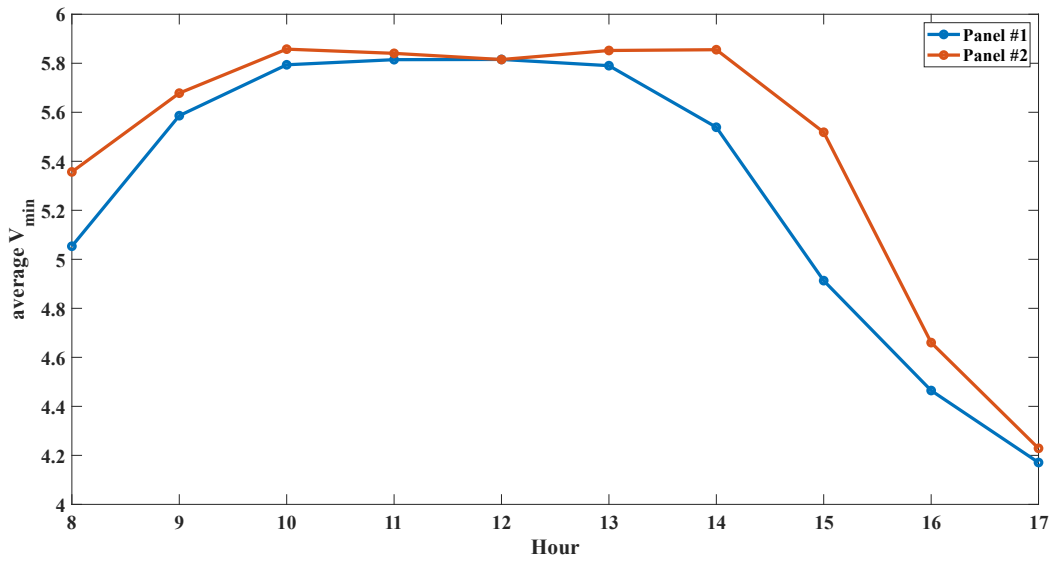


Figure 72 Change of minimum voltage per hour of the day (dataset 1)

Another notice is related to the point count, as it is noticed that at sunny hours, there are a lot of points per reading compared to non-sunny hour. A depiction of average point count per hour for three characterizers is shown in Figure 73 and it shows how characterizer 8 is better than other characterizers most of the time

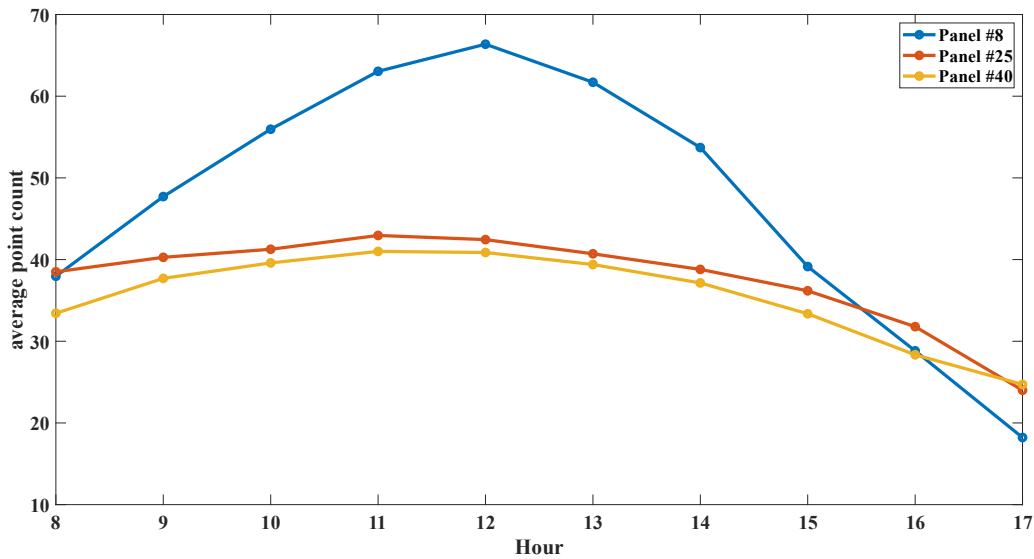


Figure 73 Average number of points per reading against hour in dataset 2

## 6.3 Parameter extraction

### 6.3.1 Parameter Extraction on given dataset

Based on Table 16 and Figure 44, we found that Laudani's algorithm is efficient when short-circuit current is below 5.48 A (corresponding to 600 W/m<sup>2</sup> and 25 C°) so based on the both datasets, 58.17% of measured IV curves have  $I_{SC} \leq 5.48$  A so we used Laudani for parameter extraction for its lower NRMSE error but keeping in mind that temperatures of real solar panels can differ from modelled temperature values which affects in turn the quality of parameter extraction (i.e., the temperature at which parameter extraction is done can be different from reality introducing slight errors in parameters).

For dataset 1, 99.95% of curves had parameters extracted, while for dataset 2, it was 98.85%. For the extracted curves (as shown in Figure 74), the first dataset has higher error than the second dataset. If we take the threshold error to be 0.05 then 83.97% of the first dataset lie below this threshold and 91.69% of the second dataset lie below that threshold, which implies the high quality of the implemented parameter extraction algorithm. The probability of having NRMSE less than or equal to some value is shown in Figure 75 and it illustrates how the fitting algorithm is more successful in dataset 2 rather than dataset 1.

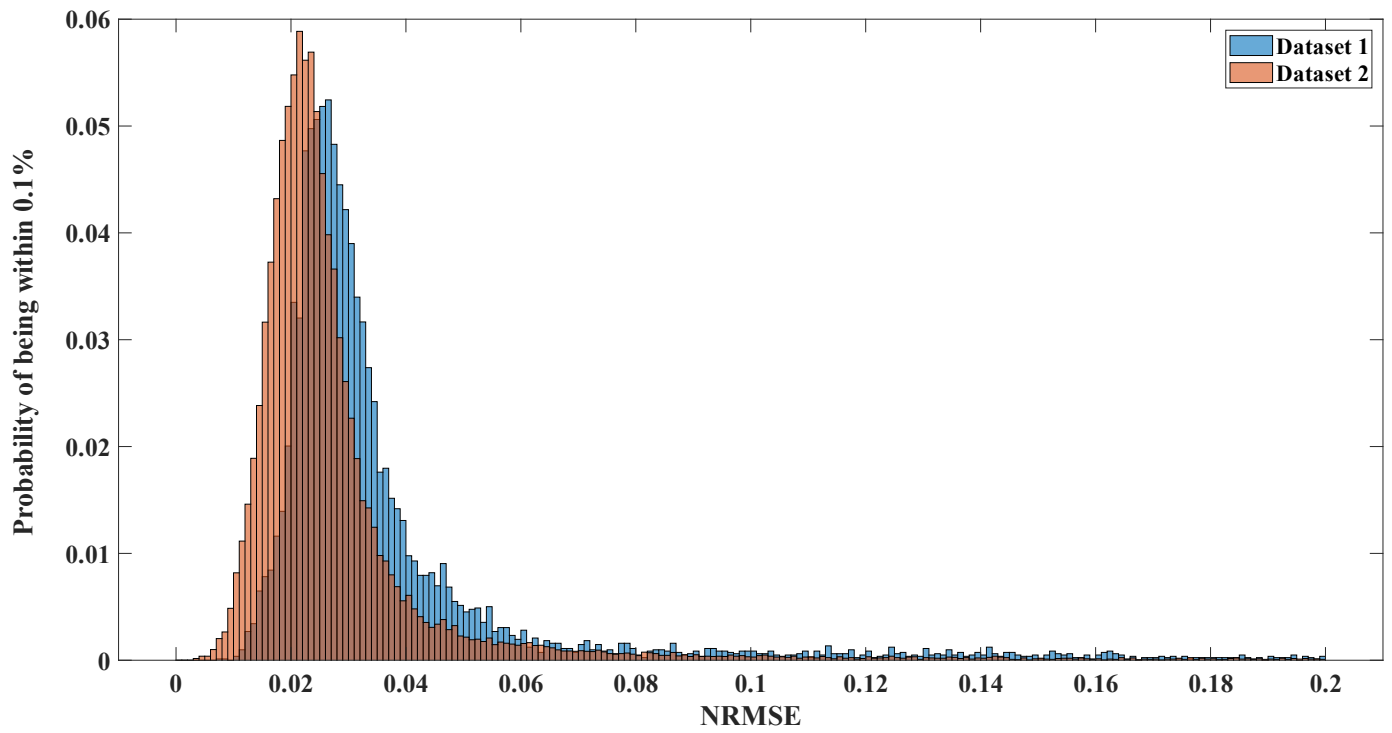


Figure 74 Histogram of NRMSE based on Laudani's parameter extraction for both datasets

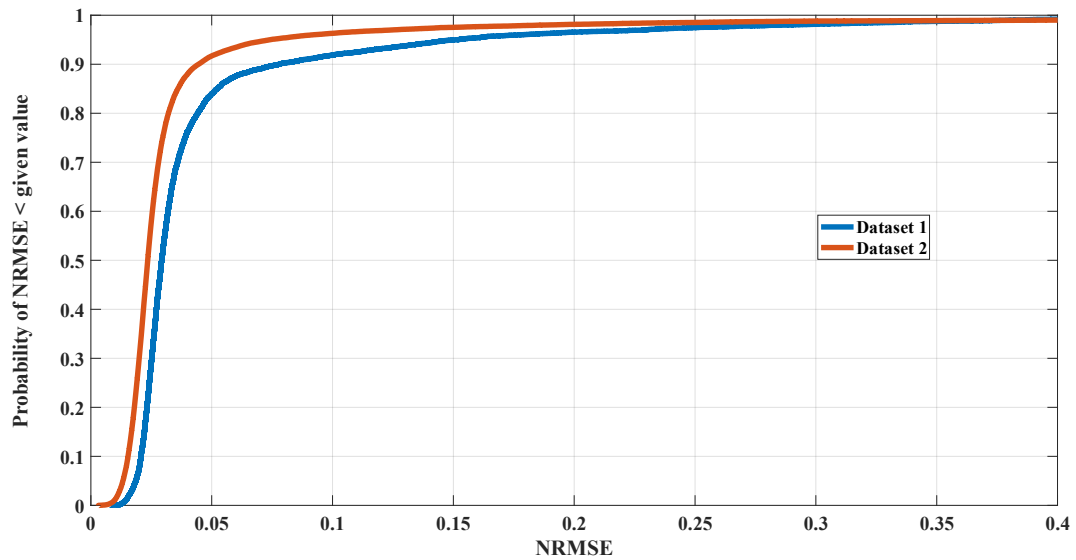


Figure 75 Probability of NRMSE lesser than a specific value

## 6.4 Parameter translation & weather models

### 6.4.1 Verifying weather models from datasets

To check the accuracy of our weather models combined with some insights about characterizers' performance. For each measurement, for any industrial parameter  $\rho$  we compute the ratio of the measured industrial parameter to the expected industrial parameter based on our model,  $\rho/\rho_{expected}$ . It is expected if our model is successful that this ratio be below 1. That is because for instance, if we correctly estimated the irradiance,  $I_{SC}$  must be lower or equal to the expected  $I_{SC}$  but never more. Also the same applies for  $V_{OC}$ ,  $P_{MP}$ ,  $FF$  and  $\eta$  (based on (75), (79), (84), (85), and (12)). For a specific  $\rho$  it is expected that  $P\left[\frac{\rho}{\rho_{expected}} \leq 1\right] = 1$  to make sense of the measurement and the weather model. Otherwise, there can be two explanations, whether the weather model is not completely accurate, or the characterizers have an issue giving some parameters that are exaggerated or misrepresentative.

In Figure 76, it is shown that weather models are more successful in dataset 1 than in dataset 2. That is because the percentage of having a higher expectation than measured is higher in the first dataset rather than the second. A summary of percentage of parameters lesser than or equal to expected parameters is shown in Table 23. In both datasets, the correctness of  $V_{OC}$  seems to be undoubtable (through both measurement and model). In first dataset, all parameters make sense except for the fill factor where only 51.86% of the data has been lower or equal to expectation. The same applies for dataset 2 where the boundary drops to only 14.80%. It is probably an issue with characterizers as they have much high fill factors compared to expected fill factors. In this regard, the performance of the first version of characterizers is much better.

Since same weather model was applied on both datasets, and the same weather model gave more sense in dataset 1 than in dataset 2, then there is for sure an issue with characterizers used in dataset 2

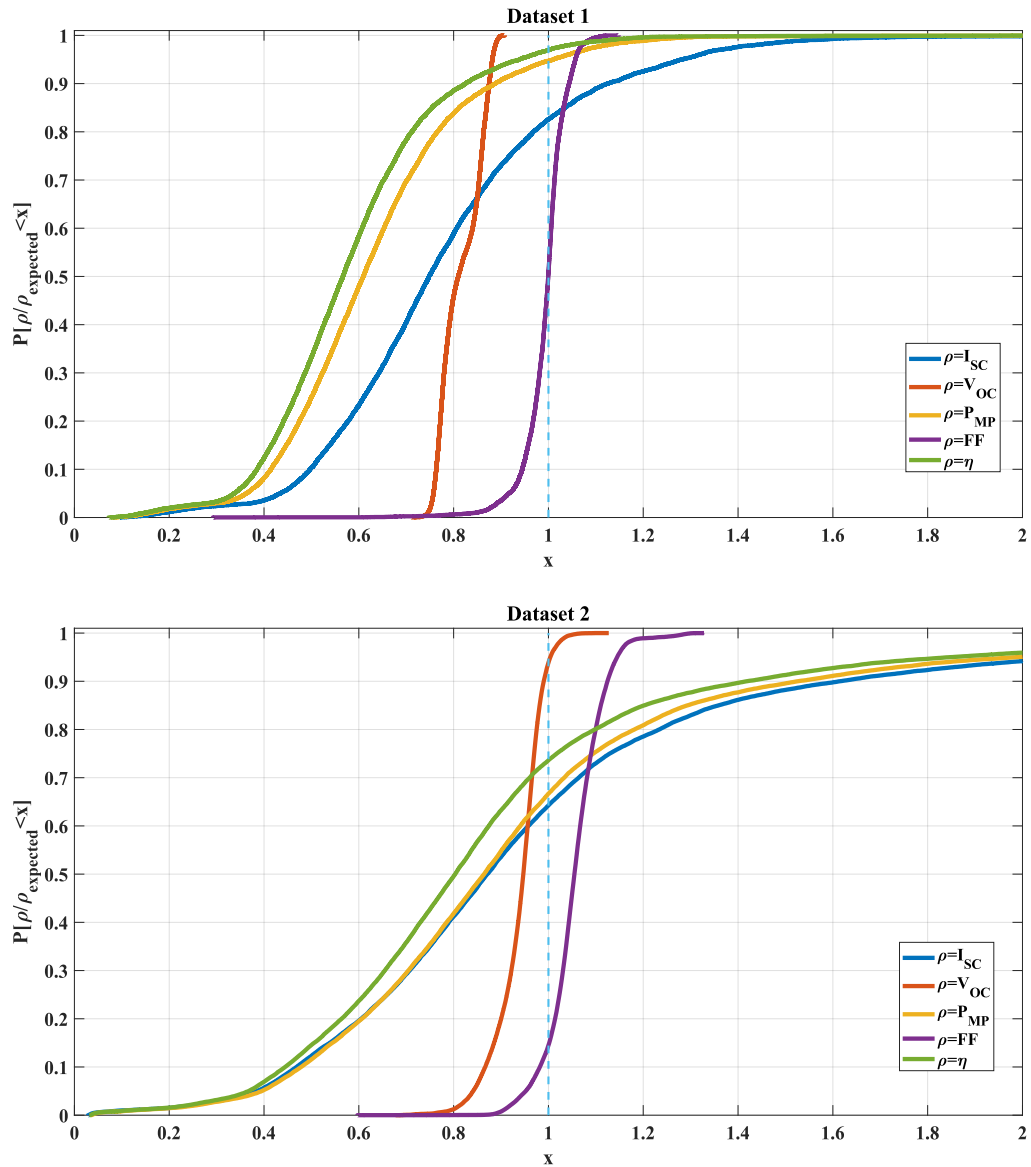


Figure 76 Probability of having ratio of parameter to its expected value lower than a given  $x$ , for both datasets



Table 23 Percentage of dataset curves where measured parameters are less than or equal to the expectation

	Dataset 1	Dataset 2
$I_{SC}$	82.62%	64.30%
$V_{OC}$	100.00%	94.13%
$P_{MP}$	94.72%	66.70%
$FF$	51.86%	14.80%
$\eta$	96.99%	73.66%

## 6.4.2 Distribution of Environmental conditions

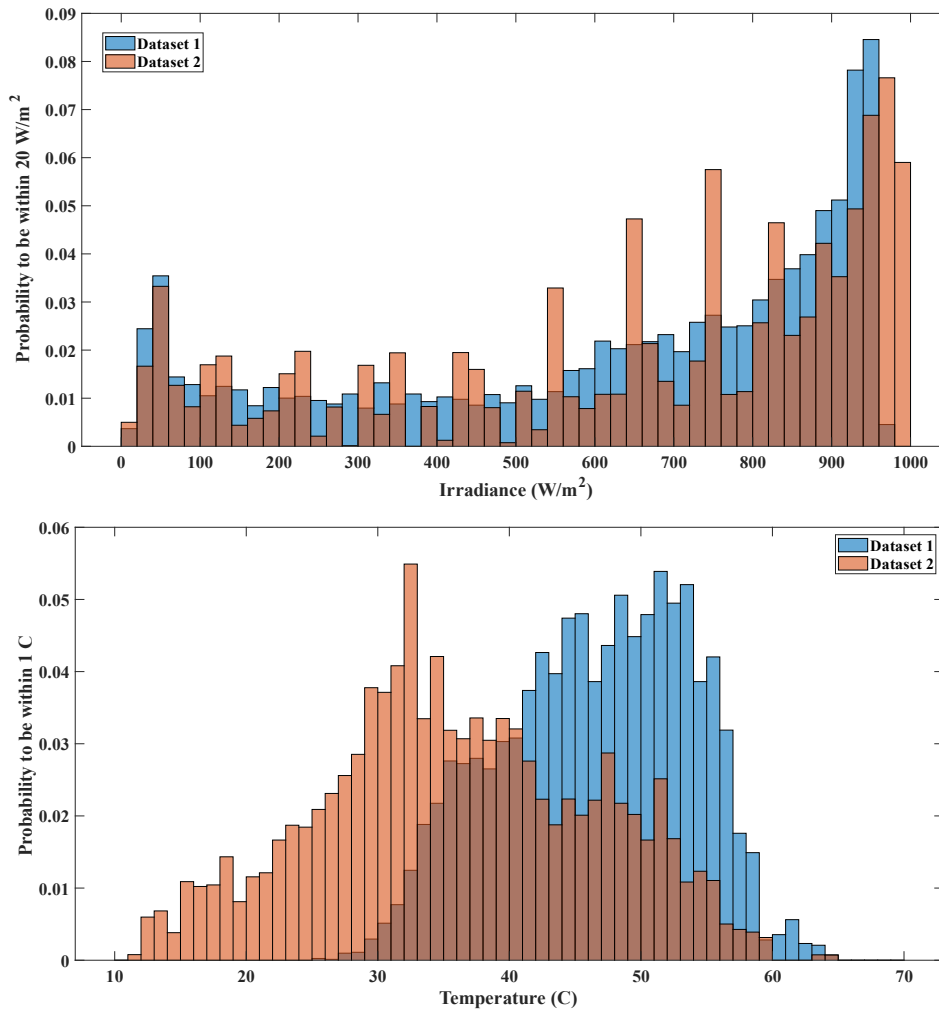


Figure 77 Probability distribution of cell temperature and irradiance in both

Since we knew the issues of readings coming out of characterizers, we, now, can trust

more our weather models and rely on characterizers' readings that comply with our given models. The distribution of cell temperature and irradiance are both shown in Figure 77. The temperature in dataset 2 is lower than these in dataset 1 (as being before summer is colder), but for irradiance, the clear-sky irradiance is very similar in both distributions.

## 6.5 Doing data analysis

We will look to collected data in several ways (as it is expected by user of analysis module- we will look through time and space. By time, we mean looking on the historical trend of parameters for a specific panel. By space, we mean looking for the surroundings of a panel at some duration and checking how panel parameters are coherent with parameters extracted from other panels. Last, but not least, we can provide expected IV characteristics for each panel and try by inspection to compare both the expected and measured to inspect characterizer or panel issues.

### 6.5.1 Analysis in time

To check if the panel is faulty or not, one must evaluate the performance of each panel against time. If there is a big deviation between expected parameters and measured parameters, one should suspect the existence of a problem. In the following analysis we will restrict our view on dataset 2, as it has more readings, and it has larger set of characterizers. To make sure, that we have reliable results we did analysis on characterizers 8 and 35, the choice of characterizer 8 is for its perfect performance (see Table 22, Figure 71 and Figure 73) and the choice of characterizer 35 is for its regular performance. We did our analysis overall the duration of dataset 2.

For panel 8, as shown in Figure 78, the short-circuit current is well enveloped by the expected value provided by our model. At some instances, the measured  $I_{SC}$  exceeds the expected one, at only very low irradiance (see  $I_{SC}$  before Apr 25, 2022). However, it is found that the measured  $I_{SC}$  drops considerably below the expected  $I_{SC}$  due to dusting of panel surfaces.  $V_{OC}$  is also well-enveloped by our model but its waveform is not clearly periodic like that of the  $I_{SC}$  and it is more sensitive for differences between expected irradiance and actual received irradiance, such that the difference between expectation and measurement widens noticeably at the end. Both  $I_{SC}$  and  $V_{OC}$  give trust into our weather model. Although the fill factor tracks the expected waveform but it seems to saturate below specific level and never goes deeper than this. This saturation on the top becomes more apparent in the period after May 25, 2022, as the dust has covered the panel, lowered the effective irradiance on the panel, and lowered the temperature and such sudden decrease beside the instability of characterizer at low irradiance (high  $V_{min}$  and lower number of points)

For panel 35, as shown in Figure 79, the short-circuit current agree very nicely but with subtle oscillations between Apr. 21 and Apr 24, 2022. These oscillations seem to be unpredictable but do not affect the whole waveform. Also, for dusting,  $I_{SC}$  drops after May 25. For  $V_{OC}$ , the waveform is followed accurately, but with subtle difference that increases whenever dusting is present. Interestingly, the fill factor is clipped severely compared to the fill factor at panel 8 which indicates a quality issue of characterizer 35 (compared to characterizer 1).

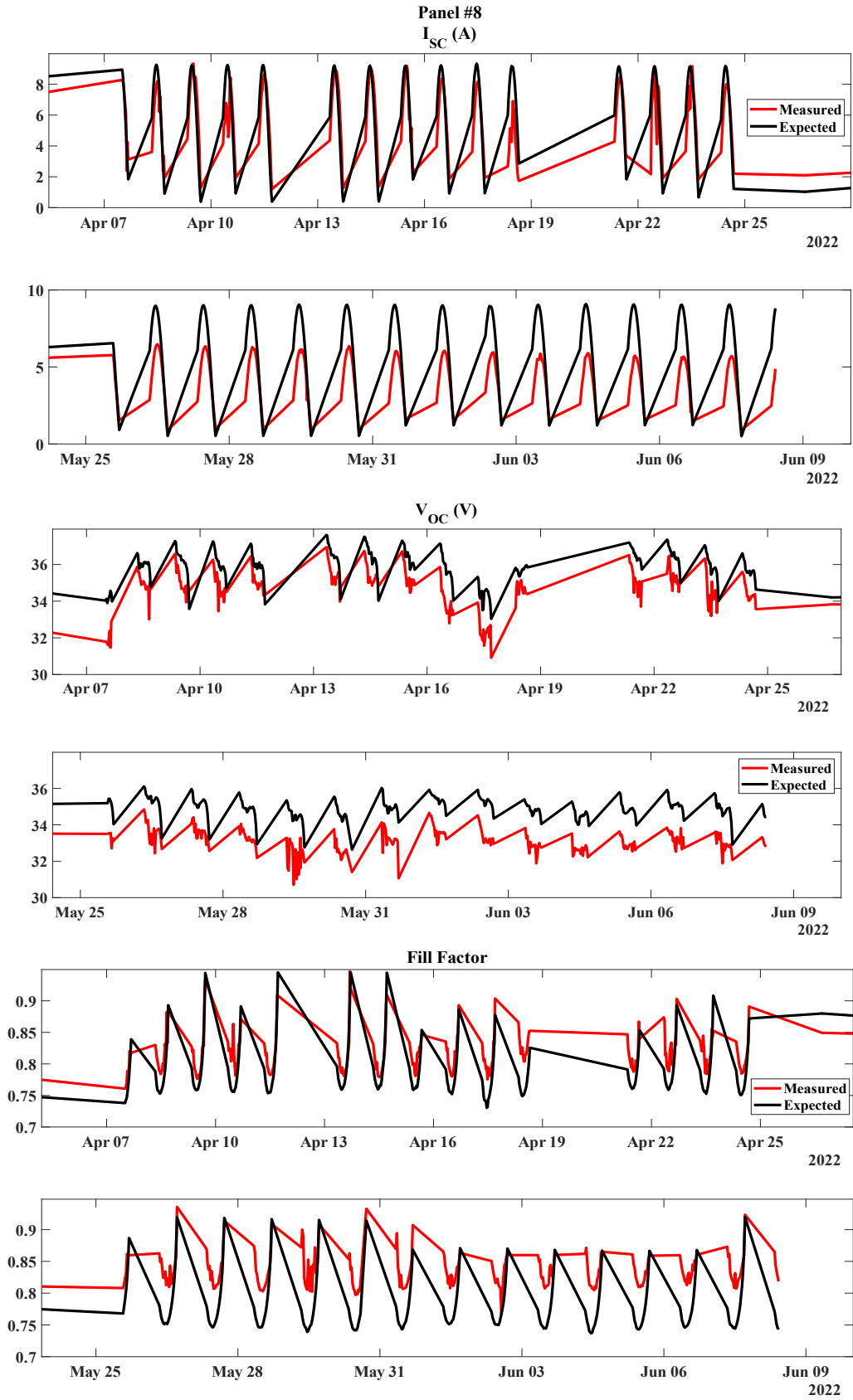


Figure 78 Time analysis of panel 8

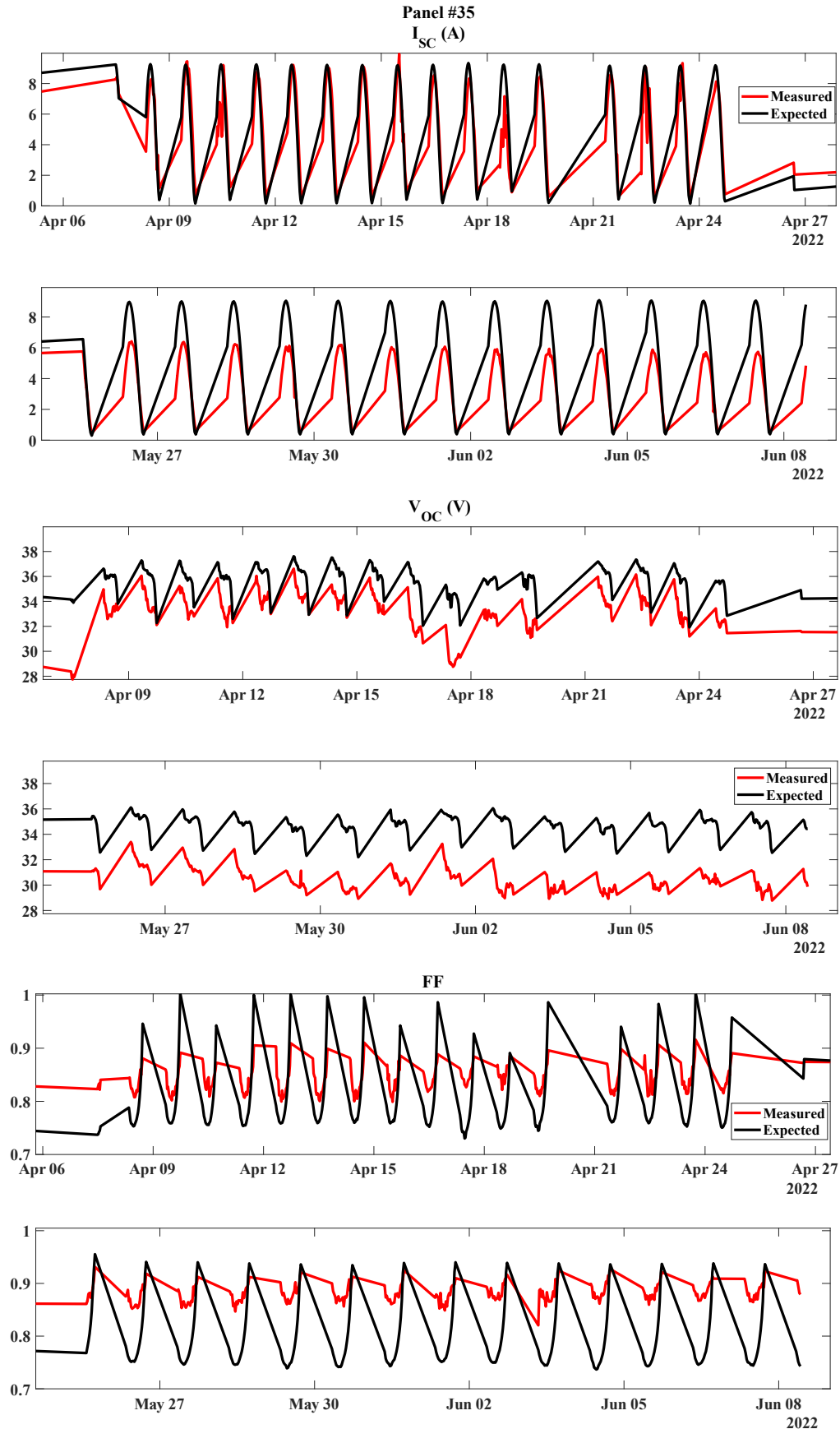


Figure 79 Time analysis for panel 35

### 6.5.2 Analysis in space

The analysis in space allows you to find the similarity and dissimilarity of estimated parameters as signals against time and it runs through the following process.

1. Specify the time region at which you need to check similarity.
2. Specify the name of the parameter.
3. Specify the ID of two panels you want to compare both in similarity (evaluate the decoherence of their parameters)- specify reference and target panels.
4. Interpolate/extrapolate the industrial parameters of the target panel at each time instance of the reference panel readings.
5. Calculate the NRMSE between two sequences as shown in (44) and return the result as the dissimilarity measure.

Table 24 Decoherence measure between panel 8 and panel 35  
**April 9, 2022 - April 24, 2022**      **May 30, 2022 - June 5, 2022**

<b><math>I_{SC}</math></b>	0.2037	0.0579
<b><math>V_{OC}</math></b>	0.0718	0.0935
<b><math>FF</math></b>	0.0476	0.0561

What analysis in space shows us, is that there are variations among panels even at the same irradiance, temperature, and time. The decoherence of parameters of panels 8 and 35 changes by moving in a dusty period. As shown in Table 24, when panels are clean, the variation of short-circuit current is higher than if they are not clean while higher variation in open-circuit voltage and fill factor can indicate an issue of soiling. The threshold of the decoherence values that indicate a problem for each parameter is not yet studied.

### 6.5.3 Comparing standard IV curves

A good way to see the performance of solar panels at different environmental conditions is to translate its IV curve from datasheet values and then compare both curves for any changes. We will take an example for two readings whose characteristics are in Table 25.

Table 25 Two readings used for standard curve comparison

	Reading 1	Reading 2
Panel ID	21	3
Measurement Time	11-Mar-2022 09:40:45	15-Mar-2022 16:31:07
Irradiance ( $W/m^2$ )	860.6673	125.899
Temperature ( $C^o$ )	29.6647	15.1136
$V_{min}(V)$	8.18	26.29

Based on Figure 80, one can see the agreement between actual measurement and an expected curve found by our algorithm. For the first readings, the fill factor of the measurement is excessively higher than it should be, also, it has lower open-circuit voltage. But for the second reading strong agreement is found at both short-circuit and open-circuit regions, but also the reading suffer from high fill factor. The agreement between both is confirmed by not having any

dust issue at the time of measurement.

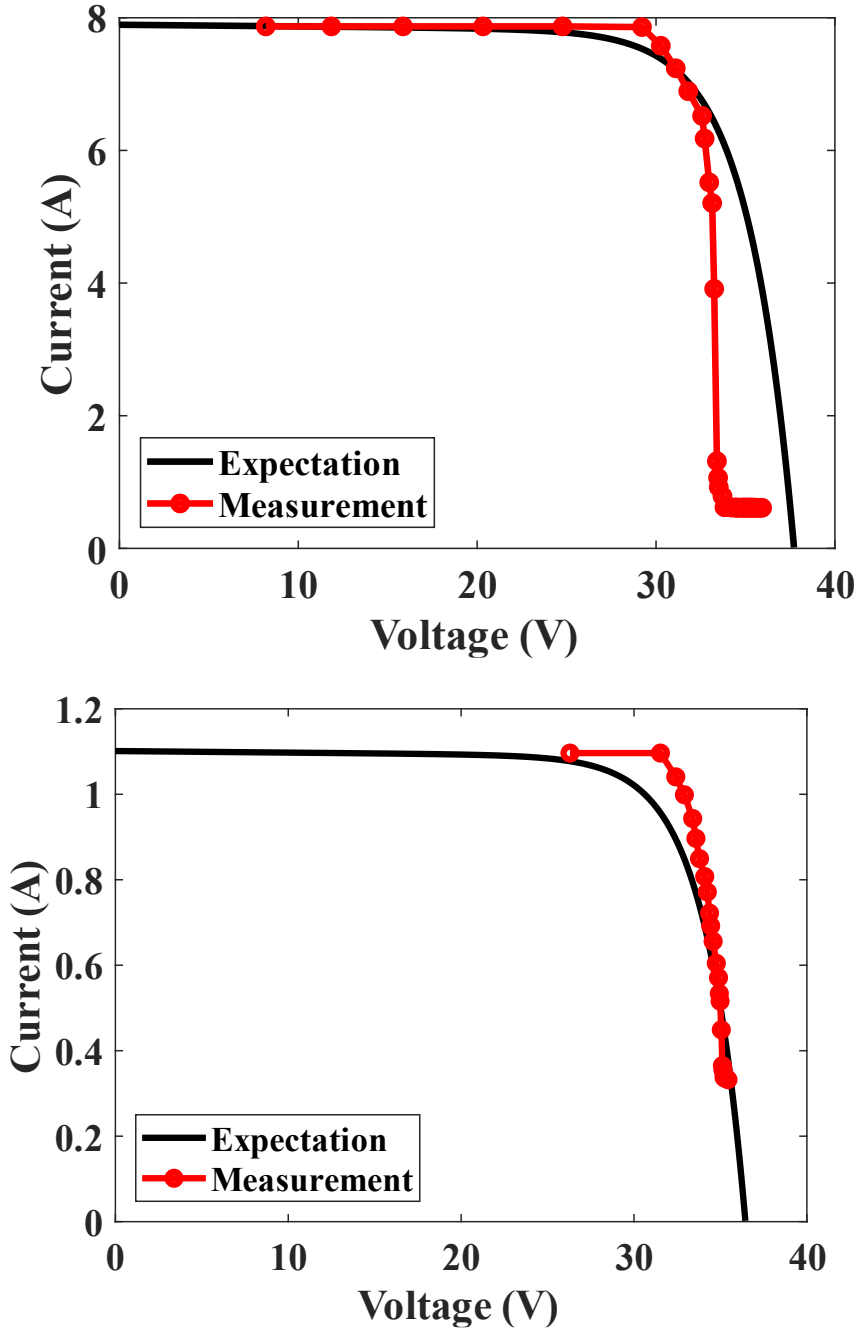


Figure 80 Comparison of standard curve generated by our model and an actual measurement (reading1 above and reading 2 below)

## 6.6 Summary

The target of this chapter is to demonstrate the different capabilities that the advisory layer of the photovoltaic monitoring system can have. Some limits on extracted faults are related to the quality of characterizers collecting information themselves. In this regard, two datasets utilizing different types of characterizers were deployed in the installed station and their output results were collected over a year in discretized fashion. Several metrics were proposed to assess the quality of both characterizers and the statistics of these metrics were investigated.

The second limitation is in the analysis module itself, so faults like partial shading were theoretically detectable although not encountered in any measurements. The analysis module is capable of doing bottom-up modelling knowing how parameters like fill factor (for instance) vary with individual cell patterns.

The next step is to assure that the modelling power we had is working correctly, so it was crucial to assure that solar panels are accurately modelled in a proper SDM model, so a comparison of two different parameter extraction algorithms was given and based on our needs only a modified version of Laudani's algorithm was utilized which gave appropriate levels of fitting errors.

What will happen next after finding panel SDM parameters is to use these parameters at different environmental conditions to find expected characteristics and judge faultiness. In this regard, we proposed two methods of analysis: analysis in time: where the history of a single panel is analyzed or analysis in space where the coherence of measurements coming from different panels is investigated. We quantified the decoherence by the normalized root mean square error of different parameters. From an advisory point of view, each parameter should have an acceptable level of decoherence so above this level we can decide a panel issue.

The last methodology in detecting faults is to compare standard IV curves together and check the irregularities that may arise from soiling, ageing, shading or issues from characterizers working in field.

# Conclusions

Based on dataset available for over a year, modelling the current-voltage characteristics is extremely helpful to be able find abnormalities either from characterizers or from panels, and can ultimately allocate faulty panels within a huge station.

Developing research and development solutions for photovoltaic is an economic opportunity and can give a competitive advantage for involved companies especially in Egypt given its abundant energy resources. As different technologies exist in the market, the one that takes biggest market share and we are interested in is polycrystalline silicon solar cell. The highest value of industrial parameters for this cell is limited by Shockley-Queisser limit. As we aim at the end to model and understand the impact of different faults on the performance of solar cells, we shifted our focus to faults detectable by current-voltage curves and different methods in the literature into finding them. We finally, adopted the model-based difference method, and moved on to build a good model that includes environmental conditions and circuit levels simulation of solar panels.

As a result, we chose a method for modelling environmental conditions and provided a mathematical ground for extracting circuit model parameters of a solar panel and also translating these parameters into different environmental conditions.

Moving after, we showed the specifications of installed stations, and technical description of the analysis module.

At the end, we had deep insights into analyzing reports out of this station and tried several analysis methods to detect solar panel operational faults.



# References

- [1] A. K. Shukla, K. Sudhakar, and P. Baredar, "Recent advancement in BIPV product technologies: A review," *Energy and Buildings*, vol. 140. 2017. doi: 10.1016/j.enbuild.2017.02.015.
- [2] O. J. Akintande, O. E. Olubusoye, A. F. Adenikinju, and B. T. Olanrewaju, "Modeling the determinants of renewable energy consumption: Evidence from the five most populous nations in Africa," *Energy*, vol. 206, 2020, doi: 10.1016/j.energy.2020.117992.
- [3] M. N. H. Comsan, "Solar Energy Perspectives in Egypt," in *the 4th Environmental Physics Conference*, 2010, no. March.
- [4] S. Obukhov and A. Ibrahim, "Analysis of the energy potential of renewable energy sources Egypt," in *MATEC Web of Conferences*, 2017, vol. 141. doi: 10.1051/mateconf/201714101035.
- [5] A. R. of E. Ministry of Electricity and Energy, "Annual Report."
- [6] A. R. of E. Central Agency for Public Mobilization and Statistics, "Annual report (2007/2008)," Cairo, 2008.
- [7] A. Khalil, A. Mubarak, and S. Kaseb, "Road map for renewable energy research and development in Egypt," *Journal of Advanced Research*, vol. 1, no. 1. 2010. doi: 10.1016/j.jare.2010.02.003.
- [8] K. D. Patlitzianas, "Solar energy in Egypt: Significant business opportunities," *Renewable Energy*, vol. 36, no. 9. 2011. doi: 10.1016/j.renene.2011.03.006.
- [9] "Steady State Analysis and Impact of Benban Solar Park on The Egyptian Transmission System 9," *International Journal of Advanced Trends in Computer Science and Engineering*, vol. 10, no. 2, 2021, doi: 10.30534/ijatcse/2021/641022021.
- [10] Schneider Electric Egypt, "ExoStruxure Platform | Schneider Electric Egypt." <https://www.se.com/eg/en/work/campaign/innovation/platform.jsp> (accessed Dec. 08, 2022).
- [11] ABB, "ABB Ability Industrial Internet of Things." <https://global.abb/topic/ability/en> (accessed Dec. 08, 2022).
- [12] "TRUST PV, SOLAR PV, PERFORMANCE AND RELIABILITY." <https://trust-pv.eu/> (accessed Dec. 08, 2022).
- [13] T. Saga, "Advances in crystalline silicon solar cell technology for industrial mass production," *NPG Asia Materials 2010 2:3*, vol. 2, no. 3, pp. 96–102, Jul. 2010, doi: 10.1038/asiamat.2010.82.
- [14] D. M. Bagnall and M. Boreland, "Photovoltaic technologies," *Energy Policy*, vol. 36, no. 12, 2008, doi: 10.1016/j.enpol.2008.09.070.
- [15] J. H. Werner, "Second and Third Generation Photovoltaics -- Dreams and Reality," 2004. doi: 10.1007/978-3-540-39970-4\_5.
- [16] J. Zhao, A. Wang, and M. A. Green, "24.5% Efficiency silicon PERT cells on MCZ substrates and 24.7% efficiency PERL cells on FZ substrates," *Progress in Photovoltaics: Research and Applications*, vol. 7, no. 6, 1999, doi: 10.1002/(sici)1099-159x(199911/12)7:6<471::aid-pip298>3.3.co;2-z.
- [17] J. Schmidt *et al.*, "23rd European Photovoltaic Solar Energy Conference, Valencia, Spain, Sept. 2008 PROGRESS IN THE SURFACE PASSIVATION OF SILICON SOLAR CELLS," 2008.

- [18] T. D. Lee and A. U. Ebong, "A review of thin film solar cell technologies and challenges," *Renewable and Sustainable Energy Reviews*, vol. 70. 2017. doi: 10.1016/j.rser.2016.12.028.
- [19] G. Conibeer, "Third-generation photovoltaics," *Materials Today*, vol. 10, no. 11. 2007. doi: 10.1016/S1369-7021(07)70278-X.
- [20] N. Kant and P. Singh, "Review of next generation photovoltaic solar cell technology and comparative materialistic development," *Mater Today Proc*, vol. 56, 2022, doi: 10.1016/j.matpr.2021.11.116.
- [21] D. A. Neamen, *Semiconductor Physics and Devices Basic Principles*, vol. 9, no. 5. 2006.
- [22] R. L. Cummrow, "Photovoltaic effect in p-n junctions," *Physical Review*, vol. 95, no. 1, 1954, doi: 10.1103/PhysRev.95.16.
- [23] L. C. Hirst, "Principles of solar energy conversion," in *Comprehensive Renewable Energy*, vol. 1, 2012. doi: 10.1016/B978-0-08-087872-0.00115-3.
- [24] S. J. Fonash, *Solar Cell Device Physics*. 2010. doi: 10.1016/C2009-0-19749-0.
- [25] A. Luque and S. Hegedus, *Handbook of Photovoltaic Science and Engineering*. 2011. doi: 10.1002/9780470974704.
- [26] Muhammad Elgamal, "Simulate IV from circuit parameters," 2022. [https://drive.google.com/open?id=1wyUugVw6gOEks1UbbYJOnCUBU2xC5KTNo&authuser=melgamal%40aucegypt.edu&usp=drive\\_fs](https://drive.google.com/open?id=1wyUugVw6gOEks1UbbYJOnCUBU2xC5KTNo&authuser=melgamal%40aucegypt.edu&usp=drive_fs) (accessed Nov. 20, 2022).
- [27] A. Ali *et al.*, "Investigation of MPPT Techniques under Uniform and Non-Uniform Solar Irradiation Condition-A Retrospection," *IEEE Access*, vol. 8, 2020, doi: 10.1109/ACCESS.2020.3007710.
- [28] S. Chander, A. Purohit, A. Nehra, S. P. Nehra, and M. S. Dhaka, "A study on spectral response and external quantum efficiency of mono-crystalline silicon solar cell," *International Journal of Renewable Energy Research*, vol. 5, no. 1, 2015, doi: 10.20508/ijrer.v5i1.1760.g6469.
- [29] W. Shockley and H. J. Queisser, "Detailed balance limit of efficiency of p-n junction solar cells," *J Appl Phys*, vol. 32, no. 3, 1961, doi: 10.1063/1.1736034.
- [30] T. Trupke, M. A. Green, and P. Würfel, "Improving solar cell efficiencies by up-conversion of sub-band-gap light," *J Appl Phys*, vol. 92, no. 7, 2002, doi: 10.1063/1.1505677.
- [31] T. Trupke, M. A. Green, and P. Würfel, "Improving solar cell efficiencies by down-conversion of high-energy photons," *J Appl Phys*, vol. 92, no. 3, 2002, doi: 10.1063/1.1492021.
- [32] P. K. Nayak, S. Mahesh, H. J. Snaith, and D. Cahen, "Photovoltaic solar cell technologies: analysing the state of the art," *Nat Rev Mater*, vol. 4, no. 4, pp. 269–285, Apr. 2019, doi: 10.1038/s41578-019-0097-0.
- [33] S. Rühle, "Tabulated values of the Shockley-Queisser limit for single junction solar cells," *Solar Energy*, vol. 130, pp. 139–147, Jun. 2016, doi: 10.1016/j.solener.2016.02.015.
- [34] M. Green, E. Dunlop, J. Hohl-Ebinger, M. Yoshita, N. Kopidakis, and X. Hao, "Solar cell efficiency tables (version 57)," *Progress in Photovoltaics: Research and Applications*, vol. 29, no. 1, 2021, doi: 10.1002/pip.3371.
- [35] D. S. Pillai, F. Blaabjerg, and N. Rajasekar, "A Comparative Evaluation of Advanced Fault Detection Approaches for PV Systems," *IEEE J Photovolt*, vol. 9, no. 2, pp. 513–527, Mar. 2019, doi: 10.1109/JPHOTOV.2019.2892189.
- [36] T. Takashima, J. Yamaguchi, K. Otani, T. Oozeki, K. Kato, and M. Ishida, "Experimental studies of fault location in PV module strings," *Solar Energy Materials and Solar Cells*, vol. 93, no. 6–7, pp. 1079–1082, Jun. 2009, doi: 10.1016/j.solmat.2008.11.060.
- [37] A. Y. Appiah, X. Zhang, B. B. K. Ayawli, and F. Kyeremeh, "Long short-Term memory

- networks based automatic feature extraction for photovoltaic array fault diagnosis," *IEEE Access*, vol. 7, pp. 30089–30101, 2019, doi: 10.1109/ACCESS.2019.2902949.
- [38] M. Ma, H. Liu, Z. Zhang, P. Yun, and F. Liu, "Rapid diagnosis of hot spot failure of crystalline silicon PV module based on I-V curve," *Microelectronics Reliability*, vol. 100–101, 2019, doi: 10.1016/j.microrel.2019.113402.
- [39] K. A. K. Niazi, W. Akhtar, H. A. Khan, Y. Yang, and S. Athar, "Hotspot diagnosis for solar photovoltaic modules using a Naive Bayes classifier," *Solar Energy*, vol. 190, pp. 34–43, Sep. 2019, doi: 10.1016/j.solener.2019.07.063.
- [40] T. Subba Rao, "Classification, parameter estimation and state estimation - an engineering approach using MATLAB," *J Time Ser Anal*, vol. 32, no. 2, 2011, doi: 10.1111/j.1467-9892.2010.00665.x.
- [41] M. Stone, "Cross-Validatory Choice and Assessment of Statistical Predictions (With Discussion)," *Journal of the Royal Statistical Society: Series B (Methodological)*, vol. 38, no. 1, 1976, doi: 10.1111/j.2517-6161.1976.tb01573.x.
- [42] M. Stone, "Cross-Validatory Choice and Assessment of Statistical Predictions (With Discussion)," *Journal of the Royal Statistical Society: Series B (Methodological)*, 1976, doi: 10.1111/j.2517-6161.1976.tb01573.x.
- [43] Muhammad Elgamal, "Analysis Module," 2022. [https://drive.google.com/drive/folders/1xFYhKjXXY1g-qZqEiiAXX3uNSJzTXdJF?usp=share\\_link](https://drive.google.com/drive/folders/1xFYhKjXXY1g-qZqEiiAXX3uNSJzTXdJF?usp=share_link) (accessed Nov. 21, 2022).
- [44] Suntech Power, "275 Watt Polycrystalline Solar Module," 2018. <https://www.enfsolar.com/pv/panel-datasheet/crystalline/29973> (accessed Nov. 20, 2022).
- [45] H. Nakamura, T. Yamada, T. Sugiura, K. Sakuta, and K. Kurokawa, "Data analysis on solar irradiance and performance characteristics of solar modules with a test facility of various tilted angles and directions," *Solar Energy Materials and Solar Cells*, vol. 67, no. 1–4, 2001, doi: 10.1016/S0927-0248(00)00331-7.
- [46] A. K. Yadav and S. S. Chandel, "Tilt angle optimization to maximize incident solar radiation: A review," *Renewable and Sustainable Energy Reviews*, vol. 23, 2013. doi: 10.1016/j.rser.2013.02.027.
- [47] D. L. King, W. E. Boyson, and J. A. Kratochvil, "Photovoltaic array performance model, SANDIA Report SAND2004-3535," *Sandia Report No. 2004-3535*, vol. 8, no. December, 2004.
- [48] D. L. King, W. E. Boyson, and J. A. Kratochvil, "Photovoltaic array performance model," *Sandia Report No. 2004-3535*, vol. 8, 2004, doi: 10.2172/919131.
- [49] M. Shimojo, K. Iwai, A. Asai, S. Nozawa, T. Minamidani, and M. Saito, "Variation of the Solar Microwave Spectrum in the Last Half Century," *Astrophys J*, vol. 848, no. 1, 2017, doi: 10.3847/1538-4357/aa8c75.
- [50] N. E. Nèmec *et al.*, "Power spectra of solar brightness variations at various inclinations," *Astron Astrophys*, vol. 636, 2020, doi: 10.1051/0004-6361/202037588.
- [51] W. D. Lubitz, "Effect of manual tilt adjustments on incident irradiance on fixed and tracking solar panels," *Appl Energy*, vol. 88, no. 5, 2011, doi: 10.1016/j.apenergy.2010.11.008.
- [52] F. Kasten and A. T. Young, "Revised optical air mass tables and approximation formula," *Appl Opt*, vol. 28, no. 22, 1989, doi: 10.1364/ao.28.004735.
- [53] European Commission, "PVGIS Photovoltaic Geographical Information System." [https://joint-research-centre.ec.europa.eu/pvgis-photovoltaic-geographical-information-system\\_en](https://joint-research-centre.ec.europa.eu/pvgis-photovoltaic-geographical-information-system_en) (accessed Nov. 26, 2022).

- [54] N. Fumo, P. Mago, and R. Luck, "Methodology to estimate building energy consumption using EnergyPlus Benchmark Models," *Energy Build*, vol. 42, no. 12, 2010, doi: 10.1016/j.enbuild.2010.07.027.
- [55] E. L. Maxwell, "METSTAT - The solar radiation model used in the production of the national solar radiation data base (NSRDB)," *Solar Energy*, vol. 62, no. 4, 1998, doi: 10.1016/S0038-092X(98)00003-6.
- [56] M. Sengupta, Y. Xie, A. Lopez, A. Habte, G. Maclaurin, and J. Shelby, "The National Solar Radiation Data Base (NSRDB)," *Renewable and Sustainable Energy Reviews*, vol. 89, 2018, doi: 10.1016/j.rser.2018.03.003.
- [57] W. Marion and K. Urban, "User's Manual for TMY2s: Typical Meteorological Years: Derived from the 1961-1990 National Solar Radiation Data Base," 1995.
- [58] "Solar Irradiance Data | Solargis: weather data and software for solar power investments."
- [59] P. Ineichen and R. Perez, "A new airmass independent formulation for the Linke turbidity coefficient," *Solar Energy*, vol. 73, no. 3, 2002, doi: 10.1016/S0038-092X(02)00045-2.
- [60] R. Perez *et al.*, "A new operational model for satellite-derived irradiances: Description and validation," *Solar Energy*, vol. 73, no. 5, 2002, doi: 10.1016/S0038-092X(02)00122-6.
- [61] M. J. Reno, C. W. Hansen, and J. S. Stein, "Global Horizontal Irradiance Clear Sky Models: Implementation and Analysis," *SANDIA REPORT SAND2012-2389 Unlimited Release Printed March 2012*, no. March, 2012.
- [62] J. Remund *et al.*, "Worldwide Linke turbidity information To cite this version :," *Proceedings of ISES Solar World Congress*, 2003.
- [63] B. Haurwitz, "INSOLATION IN RELATION TO CLOUD TYPE," *Journal of Meteorology*, vol. 3, no. 4, 1946, doi: 10.1175/1520-0469(1946)003<0123:iirtct>2.0.co;2.
- [64] B. Haurwitz, "INSOLATION IN RELATION TO CLOUDINESS AND CLOUD DENSITY," *Journal of Meteorology*, vol. 2, no. 3, 1945, doi: 10.1175/1520-0469(1945)002<0154:iirtca>2.0.co;2.
- [65] P. Ineichen, "Validation of models that estimate the clear sky global and beam solar irradiance," *Solar Energy*, vol. 132, 2016, doi: 10.1016/j.solener.2016.03.017.
- [66] P. Ineichen, "A broadband simplified version of the Solis clear sky model," *Solar Energy*, vol. 82, no. 8, 2008, doi: 10.1016/j.solener.2008.02.009.
- [67] B. Y. H. Liu and R. C. Jordan, "The long-term average performance of flat-plate solar-energy collectors," *Solar Energy*, vol. 7, no. 2, 1963, doi: 10.1016/0038-092x(63)90006-9.
- [68] T. M. Klucher, "Evaluation of models to predict insolation on tilted surfaces," *Solar Energy*, vol. 23, no. 2, 1979, doi: 10.1016/0038-092X(79)90110-5.
- [69] R. Perez, P. Ineichen, R. Seals, J. Michalsky, and R. Stewart, "Modeling daylight availability and irradiance components from direct and global irradiance," *Solar Energy*, vol. 44, no. 5, 1990, doi: 10.1016/0038-092X(90)90055-H.
- [70] M. M. Holland and L. Landrum, "Factors affecting projected Arctic surface shortwave heating and albedo change in coupled climate models," *Philosophical Transactions of the Royal Society A: Mathematical, Physical and Engineering Sciences*, vol. 373, no. 2045, 2015, doi: 10.1098/rsta.2014.0162.
- [71] M. Wendisch *et al.*, "Airborne measurements of areal spectral surface albedo over different sea and land surfaces," *Journal of Geophysical Research: Atmospheres*, vol. 109, no. 8, 2004, doi: 10.1029/2003JD004392.
- [72] R. E. Payne, "Albedo of the Sea Surface," *J Atmos Sci*, vol. 29, no. 5, 1972, doi: 10.1175/1520-0469(1972)029<0959:aotss>2.0.co;2.

- [73] ASCE-EWRI, "The ASCE standardized reference evapotranspiration equation: ASCE-EWRI Standardization of Reference Evapotranspiration Task Committee Report," *American Society of Civil Engineers*, 2005.
- [74] J. A. Duffie, W. A. Beckman, and W. M. Worek, "Solar Engineering of Thermal Processes, 2nd ed.," *J Sol Energy Eng*, vol. 116, no. 1, 1994, doi: 10.1115/1.2930068.
- [75] J. Gribbin, "Radiative Processes in Meteorology and Climatology," *Physics Bulletin*, vol. 27, no. 12, 1976, doi: 10.1088/0031-9112/27/12/041.
- [76] H. Zou *et al.*, "Alternating Current Photovoltaic Effect," *Advanced Materials*, vol. 32, no. 11, Mar. 2020, doi: 10.1002/adma.201907249.
- [77] A. M. Humada, M. Hojabri, S. Mekhilef, and H. M. Hamada, "Solar cell parameters extraction based on single and double-diode models: A review," *Renewable and Sustainable Energy Reviews*, vol. 56. Elsevier Ltd, pp. 494–509, Apr. 01, 2016. doi: 10.1016/j.rser.2015.11.051.
- [78] V. Khanna, B. K. Das, D. Bisht, Vandana, and P. K. Singh, "A three diode model for industrial solar cells and estimation of solar cell parameters using PSO algorithm," *Renew Energy*, vol. 78, pp. 105–113, Jun. 2015, doi: 10.1016/j.renene.2014.12.072.
- [79] M. Wolf and H. Rauschenbach, "Series resistance effects on solar cell measurements," *Advanced Energy Conversion*, vol. 3, no. 2, 1963, doi: 10.1016/0365-1789(63)90063-8.
- [80] N. M. A. Alrahim Shannan, N. Z. Yahaya, and B. Singh, "Single-diode model and two-diode model of PV modules: A comparison," in *Proceedings - 2013 IEEE International Conference on Control System, Computing and Engineering, ICCSCE 2013*, 2013. doi: 10.1109/ICCSCE.2013.6719960.
- [81] S. Steingrube, O. Breitenstein, K. Ramspeck, S. Glunz, A. Schenk, and P. P. Altermatt, "Explanation of commonly observed shunt currents in c-Si solar cells by means of recombination statistics beyond the Shockley-Read-Hall approximation," *J Appl Phys*, vol. 110, no. 1, 2011, doi: 10.1063/1.3607310.
- [82] M. R. Alrashidi and M. F. Alhajri, "Parameters Estimation of Double Diode Solar Cell Model," *Engineering and Technology*, vol. 7, no. 2, 2013.
- [83] M. Kermadi, V. J. Chin, S. Mekhilef, and Z. Salam, "A fast and accurate generalized analytical approach for PV arrays modeling under partial shading conditions," *Solar Energy*, vol. 208, 2020, doi: 10.1016/j.solener.2020.07.077.
- [84] T. Ma, H. Yang, and L. Lu, "Development of a model to simulate the performance characteristics of crystalline silicon photovoltaic modules/strings/arrays," *Solar Energy*, vol. 100, 2014, doi: 10.1016/j.solener.2013.12.003.
- [85] E. Batzelis, "Non-iterative methods for the extraction of the single-diode model parameters of photovoltaic modules: A review and comparative assessment," *Energies (Basel)*, vol. 12, no. 3, Jan. 2019, doi: 10.3390/en12030358.
- [86] R. Abbassi, A. Abbassi, M. Jemli, and S. Chebbi, "Identification of unknown parameters of solar cell models: A comprehensive overview of available approaches," *Renewable and Sustainable Energy Reviews*, vol. 90. Elsevier Ltd, pp. 453–474, Jul. 01, 2018. doi: 10.1016/j.rser.2018.03.011.
- [87] H. Ibrahim and N. Anani, "Variations of PV module parameters with irradiance and temperature," in *Energy Procedia*, 2017, vol. 134. doi: 10.1016/j.egypro.2017.09.617.
- [88] V. lo Brano and G. Ciulla, "An efficient analytical approach for obtaining a five parameters model of photovoltaic modules using only reference data," *Appl Energy*, vol. 111, 2013, doi: 10.1016/j.apenergy.2013.06.046.
- [89] NREL, "Photovoltaic Performance | Photovoltaic Research | NREL."

- <https://www.nrel.gov/pv/real-time-photovoltaic-solar-resource-testing.html> (accessed Dec. 10, 2022).
- [90] S. Cannizzaro, M. C. di Piazza, M. Luna, and G. Vitale, "PVID: An interactive Matlab application for parameter identification of complete and simplified single-diode PV models," in *2014 IEEE 15th Workshop on Control and Modeling for Power Electronics, COMPEL 2014*, 2014. doi: 10.1109/COMPEL.2014.6877152.
- [91] E. Saloux, A. Teyssedou, and M. Sorin, "Explicit model of photovoltaic panels to determine voltages and currents at the maximum power point," *Solar Energy*, vol. 85, no. 5, 2011, doi: 10.1016/j.solener.2010.12.022.
- [92] V. Stornelli, M. Muttillio, T. de Rubeis, and I. Nardi, "A new simplified five-parameter estimation method for single-diode model of photovoltaic panels," *Energies (Basel)*, vol. 12, no. 22, 2019, doi: 10.3390/en12224271.
- [93] A. Laudani, F. Riganti Fulginei, and A. Salvini, "High performing extraction procedure for the one-diode model of a photovoltaic panel from experimental I-V curves by using reduced forms," *Solar Energy*, vol. 103, 2014, doi: 10.1016/j.solener.2014.02.014.
- [94] A. Laudani, F. Mancilla-David, F. Riganti-Fulginei, and A. Salvini, "Reduced-form of the photovoltaic five-parameter model for efficient computation of parameters," *Solar Energy*, vol. 97, 2013, doi: 10.1016/j.solener.2013.07.031.
- [95] D. R. Ahmed, H. M. Abdullah, and F. F. Muhammadsharif, "Utilization of device parameters to assess the performance of a monocrystalline solar module under varied temperature and irradiance," *Energy Systems*, 2021, doi: 10.1007/s12667-021-00472-6.
- [96] V. lo Brano, A. Orioli, G. Ciulla, and A. di Gangi, "An improved five-parameter model for photovoltaic modules," *Solar Energy Materials and Solar Cells*, vol. 94, no. 8, 2010, doi: 10.1016/j.solmat.2010.04.003.
- [97] A. Chatterjee, A. Keyhani, and D. Kapoor, "Identification of photovoltaic source models," *IEEE Transactions on Energy Conversion*, vol. 26, no. 3, 2011, doi: 10.1109/TEC.2011.2159268.
- [98] M. G. Villalva, J. R. Gazoli, and E. R. Filho, "Comprehensive approach to modeling and simulation of photovoltaic arrays," *IEEE Trans Power Electron*, vol. 24, no. 5, 2009, doi: 10.1109/TPEL.2009.2013862.
- [99] Y. Mahmoud, W. Xiao, and H. H. Zeineldin, "A simple approach to modeling and simulation of photovoltaic modules," *IEEE Trans Sustain Energy*, vol. 3, no. 1, 2012, doi: 10.1109/TSTE.2011.2170776.
- [100] H. A. B. Siddique, P. Xu, and R. W. de Doncker, "Parameter extraction algorithm for one-diode model of PV panels based on datasheet values," in *4th International Conference on Clean Electrical Power: Renewable Energy Resources Impact, ICCEP 2013*, 2013. doi: 10.1109/ICCEP.2013.6586957.
- [101] A. Orioli and A. di Gangi, "A procedure to calculate the five-parameter model of crystalline silicon photovoltaic modules on the basis of the tabular performance data," *Appl Energy*, vol. 102, 2013, doi: 10.1016/j.apenergy.2012.06.036.
- [102] A. N. Celik and N. Acikgoz, "Modelling and experimental verification of the operating current of mono-crystalline photovoltaic modules using four- and five-parameter models," *Appl Energy*, vol. 84, no. 1, 2007, doi: 10.1016/j.apenergy.2006.04.007.
- [103] H. el Achouby, M. Zaimi, A. Ibral, and E. M. Assaid, "New analytical approach for modelling effects of temperature and irradiance on physical parameters of photovoltaic solar module," *Energy Convers Manag*, vol. 177, 2018, doi: 10.1016/j.enconman.2018.09.054.
- [104] SOLARGIS, ESMAP, and World Bank Group, "Global Solar Atlas." <https://globalsolaratlas.info/map?c=30.017976,31.506386,11&s=30.017695,31.506666&m=>

- site&pv=ground,180,29,1000 (accessed Nov. 20, 2022).
- [105] Suntech, "IV characteristics of Suntech STP275-20/Wfw at different irradiance ." [https://drive.google.com/open?id=1x2gbxVp9cD3F858o0D2MACrJJTQhABRv&authuser=melgama1%40aucegypt.edu&usp=drive\\_fs](https://drive.google.com/open?id=1x2gbxVp9cD3F858o0D2MACrJJTQhABRv&authuser=melgama1%40aucegypt.edu&usp=drive_fs) (accessed Nov. 20, 2022).
- [106] S. van der Walt, S. C. Colbert, and G. Varoquaux, "The NumPy array: A structure for efficient numerical computation," *Comput Sci Eng*, vol. 13, no. 2, 2011, doi: 10.1109/MCSE.2011.37.
- [107] P. Virtanen *et al.*, "SciPy 1.0: fundamental algorithms for scientific computing in Python," *Nat Methods*, vol. 17, no. 3, 2020, doi: 10.1038/s41592-019-0686-2.
- [108] W. McKinney, "pandas: a Foundational Python Library for Data Analysis and Statistics," *Python for High Performance and Scientific Computing*, 2011.
- [109] "frechetdist . PyPI." <https://pypi.org/project/frechetdist/> (accessed Dec. 14, 2022).
- [110] HELMUT ALT and MICHAEL GODAU, "Computing the Frechet distance between two polygonal curves," *Int J Comput Geom Appl*, vol. 5, no. 1n2, 1995.
- [111] "Vaisala: A global leader in environmental and industrial measurements." <https://www.vaisala.com/en> (accessed Nov. 26, 2022).
- [112] "MeteoStat: The Weather Record Keeper." <https://meteostat.net/en/> (accessed Nov. 21, 2022).
- [113] "pvlib python -- pvlib python 0.9.3 documentation." <https://pvlib-python.readthedocs.io/en/stable/> (accessed Nov. 26, 2022).
- [114] "matplotlib -- Visualization with Python." <https://matplotlib.org/> (accessed Nov. 26, 2022).
- [115] F. Gao and L. Han, "Implementing the Nelder-Mead simplex algorithm with adaptive parameters," *Comput Optim Appl*, vol. 51, no. 1, 2012, doi: 10.1007/s10589-010-9329-3.
- [116] D. Kraft, "A Software Package for Sequential Quadratic Programming," *Technical Report DFVLR-FB*, vol. 88, no. 28. 1988.
- [117] C. Zhu, R. H. Byrd, P. Lu, and J. Nocedal, "Algorithm 778: L-BFGS-B: Fortran Subroutines for Large-Scale Bound-Constrained Optimization," *ACM Transactions on Mathematical Software*, vol. 23, no. 4, 1997, doi: 10.1145/279232.279236.
- [118] S. G. Nash, "Preconditioning of Truncated-Newton Methods," *SIAM Journal on Scientific and Statistical Computing*, vol. 6, no. 3, 1985, doi: 10.1137/0906042.
- [119] I. Reda and A. Andreas, "Solar position algorithm for solar radiation applications," *Solar Energy*, vol. 76, no. 5, 2004, doi: 10.1016/j.solener.2003.12.003.

# Appendix

## Full Description of Analysis Module

### 1 Dependencies, APIs, and code templates

Several APIs were used in the analysis module including the following

#### 1.1 Mathematical and scientific computing packages

NumPy [106] is a Python package that is useful for manipulating multidimensional-array objects called “ndarray”. Such objects can save time for doing complex mathematical computations in the form of matrices. Sorting, addressing or matrix operations can be done easily with NumPy in a few lines of code. Most of used classes in the module have the form of vector operations, interpolation, numerical differentiation/integration, logical addressing and performing statistical operations and they could be performed easily by the help of NumPy.

SciPy [107] is another Python package that has different applications including symbolic computation, dealing with special functions, optimization problems, signal processing, linear algebra, statistics, and file input/output operations. The module uses SciPy as a part of the parameter extraction process to solve complicated nonlinear equations that involve Lambert W function and advanced parameter fitting manipulations, besides its use for saving and manipulating `.mat` files.

Pandas [108] is another Python package used mainly for big-data analytics and artificial-intelligence applications. It is used in several parts of the module to organize large portions of the data especially parsed station reports.

Frchetdist [109] is a Python package for computing the Fréchet distance between two curves which measures the extent at which two curves are so similar. A zero Fréchet distance means both curves coincide, and larger one means greater dissimilarity between both [110]. This package is used in computing the dissimilarity between different IV measurements.

#### 1.2 Weather APIs

The calculation of environmental conditions for a solar panel (i.e., the incident irradiance  $Irr_T$  and the cell temperature  $T_c$ ) depend on actual measurements from the installed site beside modelled data for weather conditions.

Real datasets including the **GHI**, **DNI**, **DHI**, ambient temperature and wind speed are available online for free including

- TMY (Typical Meteorological Year) 2/3[57] :includes data for the United States from 1961 to 2019 and some other regions in the world.
- NSRDB (National Solar Radiation Database) [55], [56]: includes terabytes of data on most of geographical regions in the world up to 2021.



- PVGIS (Photovoltaic Geographical Information System) [53] which is an online dataset provided by the European commission for several regions up to 2020.
- EPW (Energy-Plus Weather)[54]

All aforementioned datasets can be accessed through specific **APIs** provided by PVLib, but unfortunately, they are historical databases and many of them does not have information about Egypt. Additionally, most databases that have live data are proprietary for a subscription fee [58], [111].

So instead, we depended on MeteoStat[112] to retrieve the hourly measurements of ambient temperature, wind speed and pressure. MeteoStat searches multiple online databases for weather of every location on earth up to the time of inquiry. If a data is missing for a specific location or at specific time, MeteoStat performs spatial or time interpolation to find the required value.

In the designed module Temperature inquiry is done as a class method in `pv_analyser.iv_measurement.update_temperature()`. At such method, the windspeed is used to find cell temperature as in (13) and (14).

PVLib [113] is a Python package that can model several photovoltaic systems environmental conditions like finding irradiance values whether through online datasets or by other empirical models. It also can model several solar panel designs like bifacial panels for instance.

In our module, to find an irradiance for a specific object of the `pv_analyser.iv_measurement` class, the method `update_irradiance()` is used, which uses wind speed and temperature provided by MeteoStat, station location and measurement time to find the solar position as shown in (20) and (21). The GHI, DNI and DHI are calculated by Perez-Ineichen model [59]-[62] and then total irradiance is calculated. The whole procedure is summarized in Figure 81.

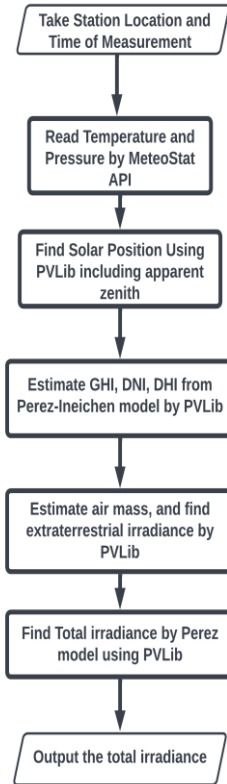


Figure 81 Flowchart for irradiance estimation

### 1.3 Additional packages

MatPlotLib [114] is used to plot an IV measurement and for graphical purposes. “pickle” and “datetime” are built-in package that help in saving variables, and manipulating time objects respectively

## 2 Functions

Several functions were defined outside the scope of any used class however, they are called within module classes or externally.

### 2.1 Reading a single characterization

`pv_analyser.find_iv(characterization)` is a function that reads a single characterization in a station report and extracts the IV characteristics from it. Figure 82 shows how the station report is formatted. For instance, characterization number 2 is composed panel ID, followed by a time stamp then a sequence of points like this  $v_1, i_1, v_2, i_2 \dots$  which includes all reading.

1	19	03/10/2022.16:17:32	33.7795	0.2497	33.6332	0.2535
2	9	03/10/2022.16:17:33	34.6312	0.4073	34.5405	0.4073
3	26	03/10/2022.16:17:35	34.6530	0.4223	34.5918	0.4223
4	15	03/10/2022.16:17:37	34.8217	0.2852	34.7901	0.2903
5	4	03/10/2022.16:17:39	34.0985	0.3939	33.9213	0.3968
6	21	03/10/2022.16:17:41	34.1059	0.5760	34.0791	0.5768
7	1	03/10/2022.16:17:43	34.6070	0.1992	34.3244	0.2029
8	17	03/10/2022.16:17:45	36.2234	0.2744	35.9881	0.2744
9	24	03/10/2022.16:17:46	34.6597	0.1718	34.6366	0.1726
10	12	03/10/2022.16:17:46	35.5149	0.3850	35.4780	0.4454

Figure 82 Sample station report. Yellow is panel ID, red is timestamp and green is sequence of IV points.

## 2.2 Reading and saving variables

`pv_analyser.save_variable(object, name)` and `pv_analyser.read_variable(name)` are functions that use pickle library to save extracted analysis, import and export data.

## 2.3 Parsing and analyzing reports

`pv_analyser.parse_station_report()` is a main function that reads station reports in the format shown in Figure 82. The inputs of the function are listed below:

1. **file\_name**: name and location of the station report.
2. **full\_report**: a logic variable that asks if the user wants to read the full report or portion of it (default **True**).
3. **atspecific**: if the **full\_report** is set to **False**. It takes the value `'location'` or `'all-panels-at-instance'` to read characterizations at a specific panel or all panels at specific time duration.
4. **time**: if **full\_report** is **False** then time receives two `datetime.datetime` objects for the start and end time of readings. Also, if **atspecific** is `'all-panels-at-instance'` then the first value is for the time at which reading is done. The function retrieves readings with minimum difference in time to the target time.
5. **panel\_id**: takes the panel ID which is important if **atspecific** is `'location'`.
6. **extract\_parameters**: a logic variable (default **False**) that determines if the user wants to extract industrial parameters of the IV measurement.
7. **condition\_extraction**: a logic variable (default **True**) that determines if IV measurement needs to be conditioned prior to parameter extraction.
8. **find\_circuit\_parameters**: a logic variable (default **False**) that determines if panel circuit parameters need to be evaluated.
9. **cell\_count**: an integer variable that defines the number of cells within a panel which is useful when finding the circuit parameters.

Additionally, `pv_analyser.parse_station_report()` discards all characterizations that have number of points below a specific threshold stored in the variable `reading_length_threshold` and it assures that all readings have positive current value. The function returns a list of `pv_analyser.iv_measurement` objects related to each characterization.

`pv_analyser.analyse_station_across_space()` performs space analysis at

specific time instance, and if data is missing at this instance, the function interpolates a new reading linearly between the two nearest readings: one before and one after and it takes the following variables as input:

1. **source\_file**: destination of station report file
2. **time\_of\_analysis**: a `datetime.datetime` object that corresponds to the instance we want our analysis at.
3. **panels\_included**: a list with all panels at which we want to make a time analysis.
4. **chosen\_parameters**: a string list that includes all parameters that we want to include in our analysis possible values are within this list ['isc', 'voc', 'imp', 'vmp', 'mp', 'fillfac', 'effciency', 'irradiance', 'temprature', 'rs', 'rp', 'idark', 'ideality', 'iph'].
5. **time\_resolution**: an integer representing the range at which we look for interpolating readings such that the function looks for readings at `time_of_analysis - time_resolution/2` to `time_of_analysis + time_resolution/2`.

`pv_analyser.analyse_panel_through_time()` is the function that does time analysis. It has inputs `source_file` and `chosen_parameters` like those in `pv_analyser.analyse_station_through_space()`. However, it has extra parameters specifying the panel under analysis (`panel_id`) and two-element integer lists to signify the start and end of the analysis period (`year, month, day, hour` and `min`). Furthermore, it has a `cell_count` input which is used when doing circuit parameter estimation.

Both `pv_analyser.analyse_station_across_space()` and `pv_analyser.analyse_panel_through_time()` return a `pandas.dataframe` object having time as index column and each of `chosen_parameters` list as a column header.

## 2.4 Running Optimization

As parameter extraction is considered a minimization problem (check (63) as an example), we define a function that does mathematical optimization called `pv_analyser.run_optimizer()` whose inputs are

1. **func**, a function header that will be passed to the optimizer, the passed function must have a single list input so each index corresponds to a parameter of this function.
2. **x0**, the initial point passed to the optimizer which is useful for finding local minima of optimized functions.
3. **ranges**, a list of slice objects (datatype in python that has start, end and step in one object) for each parameter of the optimized function which is useful for global optimization.
4. **method**, is a string that specifies different methods of optimization that can be applied. It has one of these values: 'brute', 'Nelder-Mead', 'SLSQP', 'L-BFGS-B' and 'TNC'.

When the method chosen is 'brute', only **ranges** are considered as they limit the search space at which the optimizer is looking for a global minimum. This method is guaranteed to reach a global minimum but with huge number of computations so methods like Nedler-Mead[115], Sequential Least-Square Quadratic Programming (SLSQP) [116], L-BFGS-B [117] and Truncated Newton Constrained algorithm [118] – are used to find a local minimum given an initial value **x0**. The global minimum methods are way faster but can get

trapped sometimes preventing them finding the true minimum of some problem. The output of the function is the parameter list at the minimum and the value of function at global minimum.

### 3 Used classes

Two independent classes exist within the module: `pv_analyser.panel_diode` and `pv_analyser.iv_measurement`. These classes are not inherited by any other class. `panel_diode` is a class with properties that are the circuit parameters of a panel bypass diode. It has also the capability of finding voltage at specific current value through its method `find_voltage`.

#### 3.1 `iv_measurement` class

This class is the most important class of the analysis module, and we will discuss its internal structure below.

First, its constructor passes the following parameters

1. **measuring\_time** and **acquiry\_time**: must be `datetime.datetime` objects they signify the time this measurement was taken at or how much does it need to simulate it respectively.
2. **temperature** and **irradiance**: floats for both temperature in  $C^{\circ}$  and irradiance in  $W/m^2$
3. **current**, **voltage**: flattened NumPy arrays of same length.
4. **panel\_id**: integer for panel ID.

When the `iv_measurement` is instantiated, it has the following properties

1. **measured\_current**, **current**, **simulated\_current** or **measured\_voltage**, **voltage**, **simulated\_voltage**: they are all flattened NumPy arrays that include measured reading, a conditioned version of the same reading and a circuit simulation with proper SDM parameters that best-fits the reading respectively.
2. **vmin**, **vmax**, **voc**, **isc**, **imp**, **iph**, **rs**, **rp**, **idark**, **ideality** and **efficiency**: the minimum voltage at the measured reading, maximum voltage,  $V_{OC}$  (can be different if the reading was not conditioned),  $I_{SC}$ ,  $I_{MP}$ , and  $I_{ph}$ ,  $R_S$ ,  $R_P$ ,  $I_{dark}$ ,  $n$  for the extracted SDM parameters and finally  $\eta$  for the taken measurement.
3. **statematrix**: a Python list of NumPy 2D arrays including in this order  $R_S$ ,  $R_P$ ,  $I_{ph}$ ,  $I_{dark}$ ,  $n$  and temperature matrix. This property stores all the variables required that lead to this IV measurement for a given panel.

#### Feature Extraction with `iv_measurement.extract_features()`

This method extracts industrial parameters of an IV measurement, condition real

measurement and/or extract current modes within a an IV reading.

The method **extract\_features** has an optional input **condition\_measurement** which is set to **False** by default. This option guarantees that the taken measurement is less noisy, uniformly sampled, has few irregularities that make it suitable for further processing.

The conditioning algorithm proceeds as follows:

1. Sort reading from lower voltage to upper voltage (and related current values as well).
2. Define a voltage vector running from 0 to highest voltage in the reading. The number of points in this vector is the optional input **point\_count** with default value of 1000.
3. Do linear interpolation for the current value at each point of the newly formed voltage vector to be able to uniformly sample the measurement.
4. Numerically differentiate the interpolated current vector with respect to the voltage vector and take the absolute value of the derivative (i.e., compute the absolute instantaneous conductance).
5. After the maximum power point, locate parts of the current vector whose absolute derivative is below a predefined threshold and eliminate them. The conditioning threshold is taken as an optional input to **extract\_features** and it is called **conditioning\_threshold** whose default value is 0.05.
6. Take the average of the first fifty points in the current vector and extend them to the left as the short-circuit current value of the reading.
7. For the open-circuit point extrapolate the reading with a polynomial until it intersects with the voltage axis. The default order of this polynomial is taken by the optional input **fitting\_order** whose default value is 10.

If **condition\_measurement** is True, then the function checks whether it is required to find current modes or not depending on the option **find\_current\_modes** which is set by default to False. Finding current modes follows the steps below

1. Histogram the conditioned current vector at big number of bins (1000), and find corresponding bin values.
2. Pad the histogram vector with zeros at the end, such that if a peak arises at the last element of the vector, it will be succeeded with a zero (so it is easier to identify as a peak).
3. Fit a polynomial to the histogram vector, to be easier in finding peaks without being trapped in a local noised peak (useful in analyzing a noisy reading).
4. Use **scipy.signal.find\_peaks()** to find peaks in the histogram vector and choose the biggest  $n$  ones such that  $n$  is the number of cell strings.
5. Choose either part or all of chosen peaks that have specific relative height to each other.
6. Save chosen peaks at **current\_modes** property.

All other common industrial parameters are found by means of (12), depending on the properties **voltage** and **current** which can be updated if conditioning has occurred.

### Parameter Extraction using **iv\_measurement.equivalent\_circuit()**

This method extracts the circuit parameters of the SDM model from a given IV measurement and stores the output measurements in the properties **simulated\_voltage** and **simulated\_current**. Additionally, as sometimes the parameter extraction method fails, it

updates the `equivalent_circuit_found` property to `False` if the operation failed.

Two inputs are taken for this function: `N` and `method`. `N` is the number of cells in series for the taken IV reading and `method` can take either of these values: `'stornelli'` or `'modified_laudani'`. If the method is `'stornelli'`, reading is conditioned at the beginning as all calculations depend on the maximum power point and smoothness around and afterward the same procedure proposed in [92] is implemented.

On the other hand, if `method` is `'modified_laudani'`, it is made sure that reading is conditioned, then the value of maximum possible series resistance is obtained from (72).

Three internal functions are defined within the scope of the condition of having a `'modified-laudani'` method. The first is `calculate_parameters()` and it takes  $\theta = (n, R_S)$  and returns all SDM parameters by the reduced forms given in (67), (69), (70), and (71). The second function is `cost_function()` and it takes the parameters as an input and then it evaluates the maximum absolute error to be minimized as in (63). The third function is called `example_function()` and it receives a list of two elements corresponding to  $(n, \log(R_S))$  because usually the value of  $R_S$  is very small so we can deal better with logarithms to search the parameter space.

`example_function()` is then passed to `run_optimizer()` with the option `method` equals `'TNC'` and if the value exceeds 10% of the  $I_{SC}$  then the algorithm runs brute force optimizer, but this is done very rarely and the parameters minimizing `example_function()` are obtained beside storing the best fit IV characteristics in `simulated_voltage` and `simulated_current` properties.

### Estimating Sunrise/Sunset using `iv_measurement.find_sun_time()`

It is important sometimes to inspect the measurements against the time of measurement across the day, so it becomes important to know the sunrise and the sunset of a given date. PVLib provided `pvlib.solarposition.sun_rise_set_transit_spa()` based on [119] that can estimate clearly the sunrise and the sunset of a specific date. So, a user can grasp if the taken measurements make sense or not. The evaluation of these times depends on the varying solar position, and the location of the station and time zone which are kept as constant in the module. The outputs of this function are stored in `sunrise` and `sunset` properties.

### Estimating Incident Irradiance using `iv_measurement.update_irradiance()`

To find the irradiance, one needs to know the location and time of measurement. The location is called from a module constant and stored in `pvlib.location.location` object. It is important to evaluate the temperature and pressure which can be given by the help of Meteostat to find the apparent solar position. Afterward, given the solar position and the time, one can find all components of the radiation: DNI, DHI, GHI by Perez-Ineichen model [59]–[62]. Additionally, extraterrestrial radiation component is calculated using `pvlib.irradiance.get_extra_radiation()` which depends on [61], [73]–[75]. After all components of the irradiance are calculated (DNI, DHI, GHI, extraterrestrial) and given the

albedo of the location defined as a constant of 0.4, the total irradiance is calculated and saved in the property **irradiance**.

### Estimating Cell Temperature using `iv_measurement.update_temperature()`

At the beginning it is made sure that the irradiance is estimated. Then both the ambient temperature and wind speed are taken by the MeteoStat API then they are substituted in (13) and (14) to estimate cell temperature. All required constants are stored in the module as in Table 10 for the case 'open-rack glass front and polymer back'.

### Doing Time Interpolation Between Two Readings using `iv_measurement.time_interpolate()`

At sometimes, when analyzing the whole station at once, you may not be able to find all readings at this instance so, you need to interpolate two readings together and finding an intermediate reading. To make this happen, you need to make sure that both readings are sampled at the same voltage points (which can be done by linear interpolation as well), then you linearly interpolate each voltage sample based on the timing of the two IV measurements. The inputs of these functions are two other `pv_analyser.iv_measurement` objects.

### Saving to and Reading from `.mat` files

One needs to save data to a format readable by other programming languages like MATLAB. So important properties of the `iv_measurement` object are stored into a dictionary and got saved by `scipy.io.savemat()` within the method `iv_measurement.save_as_mat()`. Or on the other hand, one can read a `.mat` file with specific entries into an `iv_measurement` object using `iv_measurement.read_from_mat()`. Both functions take a string for the file name to which one needs to read from or write into.

### Displaying Measurements and Printing Features

One can print industrial parameters of an IV measurement using `iv_measurement.display_features()` and also a plot of the IV characteristics stored in properties **voltage** and **current** can be done with `iv_measurement.plot()`. The plotting function can be run in a loop but after setting the optional input **several\_plots** to **True** and specifying the duration between plots by changing **duration** whose default is 1.3 seconds.

### Finding Dissimilarity between Two Measurements

One can calculate the similarity between two IV measurements, which is useful by first normalizing the voltage and current readings over the maximum voltage and current of the



reference reading the calculate the Fréchet distance between both curves (only the part that is common between them on voltage axis). This process is done in `iv_measurement.find_dissimilarity()`

### 3.2 cell class

This class is the parent of both `cell_string` and panel classes. The constructor function takes the SDM parameters as inputs then the method `cell.characterize()` does the characterization process.

`cell.characterize()` takes two inputs `current` - which is a NumPy vector with current readings we want to evaluate our model at and `start_guess` which is an initial value fed to the equation solver while finding the IV characteristics.

Within this function there is a loop over all values in the current axis, then an error function called `SDM(p)` which takes `p` (value of voltage) and tries to minimize the error when subtracting both sides of (11) then the value doing so is taken as an acceptable voltage value. This is done by the help of `scipy.optimize.fsolve()`. Afterward, unnecessary values in the current axis above the photocurrent are removed and data is resampled at equidistant voltages and saved in the property `measurement` of type `iv_measurement`.

### 3.3 cell\_string class

This class inherits from `cell` class, however, `characterize()` method is implemented differently. In such an implementation it takes the current vector and assigns an empty voltage vector and loops over all the cells of the cell string by defining sub-cells and summing their output voltage exactly as in (31). The resulting vector undergoes the same processing as in `cell` class and also gets saved in `measurement` property.

### 3.4 panel class

This class embodies the description of physical panel from industrial point of view and from circuit-wise equivalent point of view. For instance, properties like `model_name`, `rows`, `columns`, `cell_string_count` and `area` represent the physical properties of the panel. Also, datasheet parameters are included in properties like `isc`, `voc`, `mp`, `vmp`, `imp`, `efficiency`, `power_thermal_coefficient` and `voc_thermal_coefficient`. Furthermore, some parameters are extracted manually from datasheet like `isc_nonlinearity_factor` and `voc_irradiance_correction_factors`. The  $I_{SC}$  nonlinearity factor is  $\alpha$  in (78) and it is calculated by observing the lowest and highest  $I_{SC}$  at the lowest and highest irradiance levels. Moreover, the  $V_{OC}$  correction factors are the parameters that best fit (86), there can be higher-order correction factors like having a third order polynomial as shown in (79) but we find this unnecessary sometimes.

$$V_{OC} - V_{OC,STC} - \mu_{voc}\Delta T = c_0 + c_1 \ln(Irr^{\nabla}) \quad (86)$$

Aside from these properties, datasheet measurement is included into the property **ideal\_measurement** and all other measurements of the same panel are stored in **measurements** property which is a list of **iv\_measurement** objects. The initial values of all aforementioned parameters are those of the used panel as shown in Table 18.

### Loading a Measurement using `panel.load_measurement()`

The method `load_measurement()` can load measurement from different sources into the panel object properties **ideal\_measurement** or **measurements**. If the optional input `find_equivalent_circuit` is set to **True** (while its default is **False**), then the SDM parameters of the added reading is extracted as well and saved into the saved **iv\_measurement** (either in **measurements** or **ideal\_measurement** properties).

This function has three other optional inputs:

1. **source\_type**: and it can be `'csv'` or `'measurement'`, which allows the loaded measurements to be taken from a `.csv` file or from an **iv\_measurement** object
2. **source**: which includes wither a string of the file name or a variable of the **iv\_measurement**.
3. **type**: it can be `'STC'` so it will be loaded into the **ideal\_measurement** property- or `'taken'` which will append the read measurement into the end of the measurements list.

### Characterizing a Panel using `panel.characterize()`

To characterize a panel there are two different scenarios, either to assume all cells have same set of SDM parameters then a very good approximation of the IV characteristics is (36) but here the SDM parameters given are panel-level parameters so  $R_S$  given is the  $R_S$  for the whole panel and so on. The other scenario is to simulate where each cell has different set of SDM parameters and in these situations, we depend on (35).

Either way, one needs first to pass an **iv\_measurement** object containing the current values we want to run our simulation at besides the full set of SDM parameters per cell as they are located physically stored in the property **statematrix** of the passed **iv\_measurement** object. The passed object needs to be stored at specific index in **measurements** property.

The function takes **index**, **start\_guess** and **parameters\_are\_panel\_level** as optional inputs with default values of **0**, **2** and **True** respectively. If the number of elements in `measurements[index].statematrix[0]` (or any other element in **statematrix**) exceed

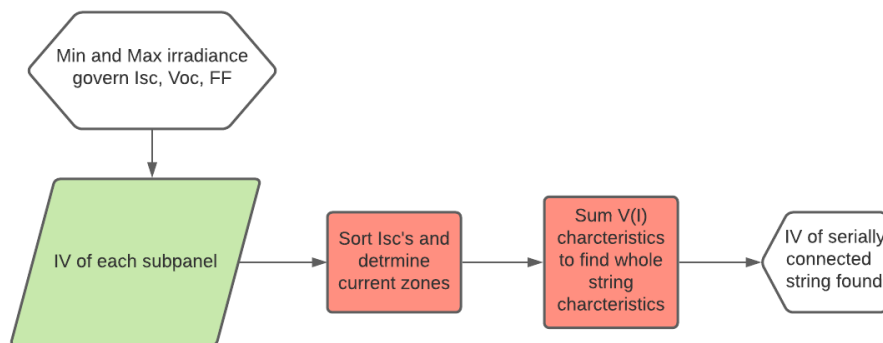


Figure 83 Finding panel irradiance from cell irradiance

one then we consider this as a sign we are doing a cell level simulation and in such scenario, we reshape the dimensions of SDM parameter matrices to comply not with physical placement but with electrical connection, so each row does not represent a physical row but cells in a single cell string. The output of this function is stored in the properties **simulated\_voltage** and **simulated\_current** of **measurements[index]**.

When simulating a panel from cell level, one needs to sort the minimum photocurrent per each cell string and accordingly we define different current zones and apply (35) freely, a process depicted in Figure 83 where subpanel means a cell string and we assume that a panel when properly operated is a serial string of cells. However, at some instances, the minimum photocurrent in each string can be similar to others so we perturb the photocurrent at such string with error less than 0.1% to be able to use the same formula again even with similar minimum photocurrents.

When simulating a panel as a whole (when **parameters\_are\_panel\_level** is set to **True**), then the situation is much nicer because of solving (36) numerically.

### Translating Parameters using **panel.translate\_parameters()**

Parameter translation occurs only when the property **ideal\_measurement** is full with an **iv\_measurement** object. At the beginning we make sure that **ideal\_measurement** has SDM parameters extracted and if not we do **ideal\_measurement.equivalent\_circuit()**. We additionally, depend on the STC parameters embodied within the panel class itself. **panel.translate\_parameters()** takes two inputs: **G** and **T** for irradiance and temperature respectively. Equations (75)/(78), (79), (80), (81), (82), and (83) are solved sequentially to translate the panel-level SDM parameters. Afterward, the translated parameters beside simulation at these new parameters are stored in the new property **translated\_measurement**.